

**Parenteral drug delivery systems
based on fatty acid modified poly(glycerol adipate)**

Dissertation

zur Erlangung des
Doktorgrades der Naturwissenschaften (Dr. rer. nat.)

der Naturwissenschaftlichen Fakultät I
Biowissenschaften

der Martin-Luther-Universität Halle-Wittenberg,

vorgelegt

von Frau Verena Maria Weiss geb. Gläßer
geb. am 27.05.1983 in Herrenberg

Gutachter

1. Prof. Dr. Karsten Mäder
2. Prof. Dr. Jörg Kressler
3. Prof. Dr. Michaela Schulz-Siegmund

Halle, den 23. April 2014

Table of contents

Abbreviations	C
1 Introduction.....	1
2 Materials.....	12
2.1 Polymers.....	12
2.1.1 PGA fatty acid esters	12
2.1.2 Hydroxypropyl methacrylamid (HPMA) copolymers.....	13
2.2 Fluorescent dyes.....	13
2.3 ESR spin probes	14
2.4 Miscellaneous	14
3 Experimental.....	15
3.1 Preparation and characterization of nanoparticles.....	15
3.1.1 Preparation of nanoparticles.....	15
3.1.2 Coating of PGA-S65 nanoparticles.....	15
3.1.3 Photon correlation spectroscopy (PCS)	16
3.1.4 Zeta potential measurement.....	16
3.1.5 Transmission electron microscopy (TEM).....	17
3.1.6 Asymmetrical flow field-flow fractionation (AF4).....	17
3.1.7 Differential scanning calorimetry (DSC)	18
3.1.8 Proton nuclear magnetic resonance (¹ H-NMR).....	18
3.1.9 X-ray diffraction (XRD)	19
3.1.10 Multispectral fluorescence imaging (MSFI) of Nile red loaded particles	19
3.1.11 Determination of drug loading	20
3.1.12 Hemolytic activity	21
3.1.13 Cell culture studies	21
3.1.14 <i>In vivo</i> experiments	22
3.1.15 <i>Ex vivo</i> experiments.....	24
3.1.16 Investigation of “bone targeting”	24
3.2 Characterization and preparation of implants and applied polymers	25
3.2.1 Characterization of Lauroyl-PGA bulk polymers	25
3.2.2 Preparation of implants.....	26
3.2.3 <i>In vitro</i> investigation of implants by spectral spatial ESR imaging (ESRI) ...	26
3.2.4 Animal care and <i>in vivo</i> multispectral fluorescence imaging.....	27
3.2.5 <i>Ex vivo</i> investigation of implants by confocal laser scanning microscopy....	28
4 Results and discussion.....	29
4.1 PGA based nanoparticles.....	29
4.1.1 Preparation of nanoparticles.....	29

4.1.2	Photon correlation spectroscopy.....	29
4.1.3	Zeta potential measurement.....	31
4.1.4	Transmission electron microscopy.....	32
4.1.5	Asymmetrical flow field-flow fractionation.....	35
4.1.6	Differential scanning calorimetry.....	37
4.1.7	¹ H-Nuclear magnetic resonance spectroscopy of nanoparticles.....	40
4.1.8	X-ray diffraction.....	42
4.1.9	Multispectral fluorescence imaging of Nile red loaded particles.....	50
4.1.10	Determination of drug loading.....	51
4.1.11	Hemolytic activity.....	52
4.1.12	Cell culture studies.....	53
4.1.13	<i>In vivo</i> experiments.....	55
4.1.14	<i>Ex vivo</i> experiments.....	63
4.1.15	Investigation of “bone targeting”.....	66
4.1.16	Further investigations of coated nanoparticles.....	68
4.2	PGA based implants.....	71
4.2.1	¹ H-NMR relaxometry.....	71
4.2.2	Texture analysis.....	72
4.2.3	Spectral spatial ESR imaging of model implants.....	74
4.2.4	<i>In vitro</i> release study by multispectral fluorescence imaging.....	82
4.2.5	<i>In vivo</i> release study by multispectral fluorescence imaging.....	83
4.2.6	<i>Ex vivo</i> investigation of implants by confocal laser scanning microscopy....	85
5	Summary and perspectives.....	87
6	References.....	93
7	Appendix.....	I
7.1	Supplementary material.....	I
7.2	Inhaltsangabe in deutscher Sprache.....	III
7.3	Acknowledgment.....	V
7.4	Publications.....	VI
7.4.1	Research Papers.....	VI
7.4.2	Book chapters.....	VI
7.4.3	Abstracts and posters.....	VI
7.5	Curriculum vitae.....	VIII
7.6	Selbstständigkeitserklärung.....	IX

Abbreviations

¹ H-NMR	proton nuclear magnetic resonance
AF4	asymmetrical flow field-flow fractionation
AAS	antibiotic-antimycotic solution
Asp	aspartic acid
AT	4-Amino-2,2,5,5-tetramethyl-3-imidazoline-1-oxyl
BB	backbone
DDS	drug delivery system
DMEM	Dulbecco's Modified Eagle Medium
Dox	Doxorubicin
EDC	1-ethyl-3-(3-dimethylaminopropyl)carbodiimide
Em.	emission
EPR	electron paramagnetic resonance
ESR	electron spin resonance
ESRI	electron spin resonance imaging
Ex.	extinction
FBS	fetal bovine serum
Glu	glutamic acid
GMO	glycerol monooleate, monoolein
HA	hydroxylapatite
HD-PMI	2-Heptadecyl-2,3,4,5,5-penta-methylimidazolidine-1-oxyl
HepG2	human hepatocarcinoma cell line
HPMA	hydroxypropyl methacrylamid
IMC	Institute of Macromolecular Chemistry of Academy of Sciences of the Czech Republic, Prague
i.v.	intravenous
LDH	lactate dehydrogenase
Lipof.	Lipofundin® N
logP	partition coefficient (octanol/water)
M _n	number average molecular weight
M _r	relative molecular mass
M _w	weight average molecular weight
MALLS	multi-angle laser light scattering
MCT	medium-chain triglycerides
MPS	mononuclear phagocyte system
MSFI	multispectral fluorescence imaging
NIR	near-infrared
NMR	nuclear magnetic resonance
NP	nanoparticle
PBS	phosphate buffered saline

PCS	photon correlation spectroscopy
PDI	polydispersity index
PEG	polyethylene glycol
PET	polyethylene terephthalate
PGA	poly(glycerol adipate)
PLA	polylactic acid
PLGA	poly(lactic-co-glycolic acid)
r_h	hydrodynamic radius
r_{rms}	root mean square radius
RBC	red blood cells
RCM	rate controlling membrane
RI	refractive index
s.c.	subcutaneous
SAXS	small-angle X-ray scattering
SDS	sodium dodecyl sulfate
SLN	solid lipid nanoparticle
τ_R	rotational correlation time
TEM	transmission electron microscopy
TL	Tempol (2,2,6,6-Tetramethyl-4-hydroxy-piperidin-1-oxyl)
THPP	5,10,15,20-Tetrakis(4-hydroxyphenyl)-21 <i>H</i> ,23 <i>H</i> -porphine
TMSP	3-(trimethylsilyl)propionic-2,2,3,3- d_4 acid
wt%	weight percent
WAXS	wide-angle X-ray scattering
XRD	X-ray diffraction

1 Introduction

The idea of “controlled” drug delivery was developed in order to reduce application frequency, enhance therapeutic efficiency of drugs and reduce their side effects. By the means of prolonged administration (sustained drug release or prolonged circulation) and/or targeted delivery of the drug to the site of action, patient compliance can be improved and therapeutic outcomes optimized. Due to the growing number of drugs with low gastrointestinal stability, high first pass metabolism or poor oral availability, the development of parenteral drug delivery systems (DDS) – besides other alternative application routes – gained particular interest in the last decades. To date, a wide range of DDS have been developed which enable the delivery of drugs from days to years. The various carrier systems can be classified according to their size into macroscale, microscale and nanoscale [1].

The ongoing search for improvement and innovation lead to a multitude of new materials, today mainly based on biodegradable structures. Besides the most prominent biodegradable polymers – polyglycolic acid, polylactic acid (PLA) and their copolymer poly(lactic-co-glycolic acid), PLGA [2-4], various classes of synthetic polymers including for instance polyesters [5,6], polyorthoesters [7,8], polyanhydrides [9-11], polyamides [12], polyurethanes [13] and polyphosphazenes [14] – natural or semi-synthetic polymers like chitosan [15,16] and alginates [17,18] as well as various lipid formulations [19-23] have been studied as biodegradable DDS. However, only some macro- and microscaled systems based on PLA and PLGA could be placed on the market yet (e.g. Trenantone[®], Eligard[®], Zoladex[®]) and no polymeric nanoparticle product is used in clinical practice today.

Depending on the physicochemical properties of different drug molecules, different characteristics of the carriers are required. There is hence no perfect delivery system meeting the demands of all drugs. In view of this, it is therefore highly desirable to develop variable systems with adjustable properties, covering a wide range of applications. In 2005, Kallinteri *et al.* published poly(glycerol adipate) (PGA) as a new functionalized biodegradable polymer for nanoparticulate drug delivery systems [24] (Figure 1-1).

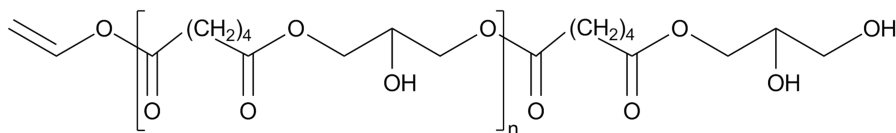


Figure 1-1. Chemical structure of the poly(glycerol adipate) backbone.

One major advantage over most other linear polyesters like PLGA is the free hydroxyl group per repeating unit. As PGA is synthesized by enzymatic polycondensation which is selective for primary OH groups, the secondary OH group of the glycerol remains available for further modification. Another prominent example where free OH groups of

glycerol are present in a polymer, is polyglycerol, mostly synthesized as hyperbranched dendrimers [25]. However, the ether bonds of polyglycerol are not biodegradable, which is a major drawback for many applications compared to PGA.

The free OH group in PGA allows the adjustment of the physicochemical properties of the polymer according to the requirements of different systems and drugs. PGA itself is hydrophilic but not soluble in water. By esterification of PGA with fatty acids, composite amphiphilic systems with hydrophilic and lipophilic features are obtained, representing a combination of polymer and lipids. The esterification is a random process resulting in a comb-like polymer with random distribution of the side chains throughout the polymer backbone (Figure 1-2). For this work, several series of PGA polyesters with varying esterification degree of different saturated and unsaturated fatty acids have been synthesized to explore the characteristics and the potential of fatty acid modified PGA as DDS. The synthesized polymers are named with L, S, Ol or B for lauroyl, stearoyl, oleoyl or behenoyl side groups followed by a number which represents mol% of esterified OH groups (e.g. PGA-S20 where 20 % of the OH groups are esterified with stearic acid).

In general, it should be mentioned that for each experiment, it was considered, which PGA-fatty acid esters should be used in order to get a good picture of the various properties. Due to the limited amount available of each bulk polymer (0.15 – 1 g), it was not possible to carry out each experiment with all relevant polyesters.

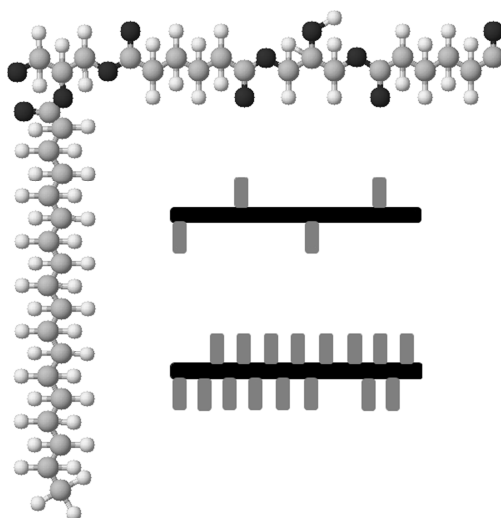


Figure 1-2 Outside: Ball-and-stick model of stearoyl substituted PGA. Inside: Schematic comb-like structures of PGA-S20 and PGA-S85. The average number of stearoyl groups per polymer chain is about 4 for PGA-S20 and 16 for PGA-S85.

Figure 1-2 depicts the comparison of the PGA species with highest and lowest content of stearoyl side chains, PGA-S20 and PGA-S85. The main differences are the average distance between the “teeth” of the comb-like polymer and their overall volume requirement in relation to that of the polymer backbone. For PGA-S20, the average number of stearoyl groups per polymer chain is about 4 and for PGA-S85 it is about 16, resulting in volume fractions of the alkyl chains of about 0.24 and 0.57 respectively.

These structural differences have far reaching consequences for the morphology and structure of systems formed by these polymers. In this work, various fatty acid modified PGAs have been used for the preparation of drug delivery systems in the form of macroscale implants as well as nanoscale particles. Special attention was given to the comprehensive *in vitro* characterization of these systems.

Nanosized delivery systems have been studied intensely for parenteral application of drugs in the last decades. The discovery of a possible drug delivery to target cells by active or passive targeting brought back Paul Ehrlich's idea of the "Magic Bullet" from the early 1900s [26]. In 1975, Helmut Ringsdorf published the concept of a polymer-drug conjugate including a moiety for targeting to specific biological sites, e.g. for specific receptor interaction [27]. This is today referred to as "active" targeting [28] (e.g. Adcetris®). "Passive" targeting, in contrast, is not achieved by the attachment of special moieties but is based on Hiroshi Maeda's finding of the "enhanced permeability and retention (EPR) effect" [29,30]. His group found the accumulation of nanoscaled carriers in solid tumors which was ascribed to their unique pathophysiological characteristics, including leaky vascular architecture, extensive vascular permeability and an impaired lymphatic clearance [31-33]. This is a promising strategy in cancer therapy [34] and already implemented in clinical praxis today (e.g. Abraxane®, Caelyx®). Another passive approach in research is the targeting of pathological endothelium, which is also called vascular targeting [35-37].

A large variety of nanoscaled drug delivery systems have been developed over the years, ranging from soluble polymer conjugates [38-40] and dendrimers [41,42] via micelles [43-45], mixed micelles [46-48] and liposomes [49-51] to liquid nanoemulsions [23,52,53], liquid-crystalline cubosomes [54,55] and supercooled smectic nanoparticles [56] to combined systems like nanocapsules [57-59] and nanostructured carriers (NLC) [60-62] to solid polymeric nanoparticles [63-66] and solid lipid nanoparticles (SLN) [22,67,68]. However, only few nanoscaled DDS for parenteral application have been brought to market so far, mainly based on liposomes (e.g. AmBisome®, Caelyx®, Visudyne®) or emulsions (e.g. Diazepam-®Lipuro, Etomidat-®Lipuro, Disoprivan®) as well as some polyethylene glycol (PEG)-protein conjugates (e.g. PEG-Intron®, Pegasys®, Neulasta®). Upon comparing liquid systems with solid particles, it becomes clear why the ideal DDS has not been found yet. Whereas liquid systems provide higher solubilization capacity than solid ones [69], they lack in stability and protection for the incorporated molecules as well as control of drug release [70-72]. Solid systems, in contrast, might control the release of drugs and provide protection against degradation [71,72], but most of them suffer the drawback of poor incorporation rates [22,72-74]. The most widely used polymers for solid nanoparticles are PLA and PLGA although they show relatively low drug loading capacities and often an initial burst release of the drug [66,73,75]. As an alternative to polymeric systems, lipid based SLNs have been proposed as carriers for lipophilic drugs [22,76,77]. However, the crystalline state of the SLNs and their platelet-like shape limit drug incorporation and provide only short diffusion

pathways [23,60]. Actually, it has been observed that in most cases, a large fraction of drug is localized at the surface of the particles instead of being incorporated within the particle core [78-81]. The ejection of drug molecules from the matrix is also promoted by polymorphic transitions of the lipids [72,82] and increase in crystallinity [83] over time. Another drawback of SLNs and many other nanocarriers is the need for additives like surfactants to stabilize the particles. Amphiphilic stabilizers can form coexisting colloidal structures and can furthermore cause irritation *in vivo*. It is therefore highly desirable to develop self-stabilizing systems. Prominent examples are amphiphilic PEGylated diblock copolymers like PEG-PLA and PEG-PLGA which self-assemble in water and form stable systems [84-86]. In this study, the optimization of the widely used interfacial deposition method (also known as nanoprecipitation method) [24,87,88] enabled the preparation of PGA-fatty acid ester nanoparticles without the need for surfactants or other additives.

Prior to this work, the knowledge about morphology, size and other properties of PGA nanoparticles was quite limited [24,89,90]. Two cell culture studies regarding their uptake in brain tumor cells had been published [91,92] but nothing was reported about internal structures, aggregate states, thermal behavior and polarity of the nanoparticles. These are, however, crucial characteristics to understand drug incorporation and *in vivo* behavior of the carriers. Moreover are these fundamental parameters for the effective strategic development of the material. Particle size is a very important parameter, influencing e.g. *in vivo* fate, phagocytosis, body distribution and tumor accumulation [93-95]. Yet not only the size but also the geometry of particles affects their transport and biodistribution within the blood vessels, their adsorption to mucosa or endothelium, as well as their strength of adhesion and internalization into cells [23,37,96]. Furthermore, both particle size and shape influence *in vitro* characteristics of nanoparticles such as drug incorporation, internal diffusion pathways, dispersion rheology, storage stability etc. [23].

With regard to drug loading and release, systems that offer a compromise between highly ordered crystals and fluid emulsions are most desirable. Yet an accurate knowledge of shape and internal structure of a carrier system is prerequisite to develop rational strategies for modification, drug incorporation and targeting. It was therefore the first aim of this study to prepare nanoparticles of different PGA based polymers with varying fatty acids, esterification degrees and aggregate states and characterize their structure and properties in detail. The characterization of nanoscaled systems is, however, not an easy task. The methods, which are suitable for the nanoscale, are based on different measurement principles and thus possibly lead to different results. Particle sizing is therefore especially challenging. In this study, the combination of photon correlation spectroscopy (PCS), asymmetrical flow field-flow fractionation (AF4) and different transmission electron microscopy (TEM) methods provided comprehensive particle size data as well as information about particle shape and structure. The inner structure was furthermore investigated by small-angle and wide-angle x-ray diffraction (SAXS, WAXS) in more detail. WAXS measurements provided information about the

molecular packing of the fatty acid side chains of the polymers whereas SAXS peaks revealed data about the supramolecular nanostructure. On the basis of these observations, together with the findings of TEM, structural models of polymer arrangement in PGA based nanoparticles have been proposed. As an additional important parameter of polymers and nanoparticles, their thermal behavior was characterized by means of differential scanning calorimetry (DSC), SAXS, WAXS and proton nuclear magnetic resonance spectroscopy ($^1\text{H-NMR}$). Thereby, particular importance was attached to room and body temperature to get information about storage stability and potential *in vivo* melting of the particles. Information about the polarity of the particles has been acquired by the incorporation of the lipophilic fluorescence dye Nile red ($\log P \sim 5$ [97]). The strong solvatochromism of this dye, depending on the physicochemical properties of its environment, and the almost fully quenched fluorescence intensity in water [98] make it a valuable reporter molecule for the polarity of lipophilic structures.

Drug incorporation in nanosized systems is a very challenging task and – as mentioned above – drug loading capacity is often a considerable drawback of solid nanocarriers. However, a reliable determination of the loading capacity is probably just as challenging. In most studies, drug loading is only determined by qualitatively monitoring drug precipitation. However, precipitated drug is not always easy to detect and the precipitation can also occur highly retarded [23,72]. Therefore, a number of quantitative methods have been published [23,99-102], most of them facing the difficulty to separate the free drug, which was not incorporated, from the particles. In this study, an own procedure has been developed, based on gel filtration, lyophilization and fluorescence measurement. The loading capacity of solid PGA-S65 nanoparticles was investigated for the highly lipophilic fluorescent dye DiI ($\log P \sim 20$ [103]) and the lipophilic tetrakis(4-hydroxyphenyl)-21*H*,23*H*-porphine (THPP; $\log P \sim 6.4$) which is a low-priced analog to the photosensitizer temoporfin (Foscan[®]) [104].

As a next step towards *in vivo* experiments, it was the aim to investigate the hemolytic activity of the nanoparticles as well as their toxicity for human hepatocarcinoma cells (HepG2). Erythrocytes are among the first cells to come into contact with intravenously (i.v.) injected pharmaceuticals. Therefore, hemolytic activity is a crucial value to be determined before performing *in vivo* experiments. Many molecules, especially amphiphiles show hemolysis of red blood cells (RBCs) as a result of interaction with the RBC membrane. For biomedical particles, hepatocytes are also an important test system [105] as the liver is the main organ for biotransformation and defense against xenobiotics and has also been identified as the preferential site of nanoparticle accumulation in the body [106-108]. Compatibility with HepG2 cells was determined by a Qblue viability assay to quantitatively measure the proliferation and metabolic activity of cells. This assay is based on the conversion of the non-fluorescent redox dye resazurin into a highly fluorescent product (resorufin) by metabolically active cells [109]. Fluorescence intensity is therefore a direct measure of the metabolic activity of cell cultures and can be quantified on a fluorescence microplate reader [110,111]. In

addition, a modified lactate dehydrogenase (LDH) cytotoxicity assay was conducted in order to obtain information about the cell quantity. The LDH assay is commonly used as a measure of membrane integrity of cells. Upon membrane damage, LDH, which is present in all cells, is released into the medium and the activity correlates with the number of lysed cells. LDH activity can be determined by a coupled enzymatic reaction which leads to a photometrically measurable product. In this study, the assay was modified and used for the estimation of cell quantity [112].

After reviewing all results of *in vitro* characterization, PGA-S65 nanoparticles have been selected for the *in vivo* study. Loading of the nanoparticles with the near-infrared (NIR) fluorescent dye DiR provided the possibility of non-invasive monitoring by *in vivo* multispectral fluorescence imaging (MSFI) after i.v. injection. DiR has excitation and emission maxima in the NIR region (750 nm/780 nm [113]), where light scattering and absorbance as well as autofluorescence of tissue are lowest [114,115]. NIR light in the range of 650-900 nm, the so called optical window [116,117], is able to penetrate biological tissues much more efficiently than visible and ultraviolet light and is therefore most suitable for optical imaging of deep tissues in living small animals [116,117]. The first *in vivo* experiment was conducted in healthy SKH1 mice to get information about body distribution and fate of the nanoparticles after i.v. injection. In the second study, tumor accumulation of nanoparticles was investigated in a human xenograft colon carcinoma model (HT29) in athymic Nude-Foxn1 mice [118-120].

One major drawback concerning the administration of nanoparticles and other colloidal carriers is their rapid elimination from the blood circulation after i.v. injection [121-123]. The interaction of the particle surface with plasma proteins leads to opsonization and sometimes destabilization of the particles [124,125]. Opsonization through protein adsorption activates the unspecific immune system, in particular the phagocytic cells of the mononuclear phagocyte system (MPS), including for example circulating monocytes, Kupffer cells of the liver sinusoids and splenic macrophages, and promotes particle uptake by these cells [126]. The interaction of colloidal systems with the MPS is determined by their size, their charge and by the physicochemical properties of the particle surface [93,127,128]. In general, larger particles and hydrophobic particles are taken up faster due to facilitated protein adsorption [94,129]. In order to overcome this obstacle and prevent opsonization, several approaches of surface modification have been reported. A widely used method is the shielding of the particle surface by coating, mostly with hydrophilic polymers [121,130,131]. This is often named "stealth" drug delivery as the coating is intended to render the particle "invisible" for the MPS [94,132,133]. Thereby, decreased protein adsorption, reduced phagocytic uptake, prolonged blood circulation and reduced uptake in the liver have been demonstrated [121,127,131,132,134]. The discussed mechanisms for this phenomenon are shielding of the surface charge, hydrophilization of the particle surface, steric hindrance and the formation of a polymeric hydrogel layer avoiding protein adsorption [122,135,136]. A wide range of coating materials have been used, of which block copolymers of ethylene oxide and propylene oxide (Ploxamer surfactants) and the homopolymer PEG are the

most extensively studied [121,133,137,138]. The attachment to the nanoparticles can occur either through physical adsorption (e.g. Poloxamer) or by covalent conjugation (e.g. PEG).

In order to prolong *in vivo* circulation time of PGA-S65 nanoparticles in the present study, physical coating with Poloxamer as well as covalent bonding of PEG chains to PGA have therefore initially been considered. Coating of physically adsorbed Poloxamer would have been easily realizable (and was already implemented for *in vitro* cell experiments) but assumed to be possibly unstable *in vivo*. Experiments for covalent attachment of PEG chains to the PGA backbone by click chemistry were successful; however, already a few PEG chains made the resulting polymer water soluble. Inspired by a lecture of Karel Ulbrich from the Institute of Macromolecular Chemistry AS CR in Prague (IMC), Hydroxypropyl methacrylamid (HPMA) copolymers were selected for nanoparticle coating. HPMA copolymers are loosely coiled, hydrophilic and mostly neutral macromolecules without affinity for blood vessels or plasma membranes [139] and good biocompatibility [140]. HPMA copolymers are intensively studied [38,140-143] and typically used as polymer-drug conjugates for the delivery of anticancer drugs to solid tumors. Promising therapeutic activity has been reported [144,145] and several conjugates have been subjected to clinical trials [140,146,147]. HPMA copolymers with hydrophobic substituents (e.g. cholesterol) which self-assemble into polymeric micelles or nanoparticles [148,149] have also been reported as effective carrier systems for solid tumor targeting by EPR effect [148]. Regarding the coating of PGA based nanoparticles, cholesterol moieties of these amphiphilic polymers seemed to be suitable as hydrophobic anchors, which could be physically included in the nanoparticles during preparation. Fixed in this way, the HPMA copolymer was intended to form a hydrophilic shell around the PGA-S65 nanoparticles.

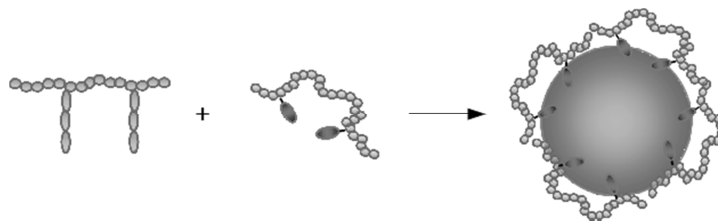


Figure 1-3. Formation of coated nanoparticles from PGA-S65 and cholesterol bearing HPMA copolymer.

In addition to this physical way of coating, covalent bonding of semitelechelic HPMA copolymers to the nanoparticle surface was planned. Semitelechelic polymers are linear macromolecules with a reactive group at only one end of the polymer chain. This functional group permits one point conjugation of the macromolecule to other species or surfaces without cross-linking [140]. Multivalent and semitelechelic HPMA copolymers were already successfully used for covalent surface modification and coating of polyelectrolyte and adenoviral gene delivery vectors [150-155]. For the coated vectors reduced binding of blood proteins, decreased phagocytic uptake, prolonged blood circulation, increased bioavailability and reduced toxicity compared to PEG-coated

complexes have been reported [150]. Amino group modified polystyrene latex nanoparticles have also been coated with HPMA copolymers as model particles in order to study the coating process to NH_2 groups [156].

In this study, free carboxyl groups on the surface of the PGA-S65 nanoparticles were used for covalent bonding of semitelechelic HPMA copolymer conjugates bearing a primary amino group at the end of the polymer chain. These carboxyl groups result from the conversion of vinyl end groups (Figure 1-1) through hydrolysis [157-159].

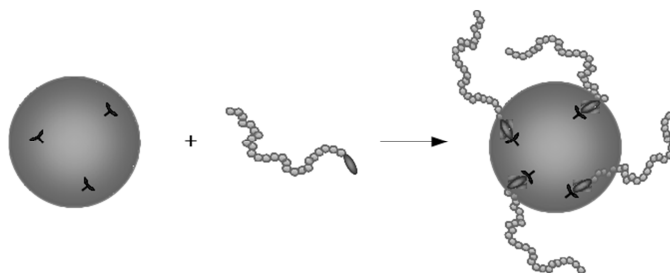


Figure 1-4. Covalent coating of nanoparticles with HPMA copolymer.

The two coating methods were compared regarding particle size, zeta potential and *in vivo* distribution of the resulting nanoparticles as well as coating efficiency. In order to track the distribution of the coating polymer *in vivo*, the far red fluorescent dye Dy676 was covalently attached to both HPMA copolymers by a stable amide bond. Simultaneous fluorescence imaging of DiR and Dy676 with two filter sets and the unmixing of the component signals by the software afterwards provided the opportunity to monitor the distribution of the nanoparticles and the coating polymer in parallel. To get deeper insight into the body distribution, mice were autopsied at the end of the study and fluorescence intensities of both dyes measured in various organs.

In view of some unexpected observations during the *in vivo* study, further *in vitro* experiments were carried out as a follow-up. This involved a more detailed study of the coating efficiency as well as an investigation of nanoparticle binding to bones. The observed attraction of PGA-S65 nanoparticles to bones could be caused by various reasons. Possible mechanisms are an attachment of PGA to the inorganic matrix, mainly hydroxylapatite (HA) or calcium ions, an attachment to the organic matrix or phagocytic uptake by mononuclear macrophages of the MPS lining the bone marrow sinusoids [160-162]. To further elucidate the relevant mechanism, the possible binding of the nanoparticles to Ca^{2+} ions was investigated by complexometric titration and a binding assay with HA.

The potential of fatty acid modified PGA is by far not limited to nanoparticles. In the second part of this work, different Lauroyl-PGAs were investigated regarding their application as implants for drug delivery. Whereas drug delivery with nanoparticles mainly focuses on targeting to specific sites in the body, drug delivery by implants and microparticles is primarily intended to prolong the release of drugs in order to achieve sustained local or systemic therapy over a certain period of time.

The concept of extended drug release started with implanted tablets or pellets of hydrophobic drugs in the 1930s [163,164]. In the 1960s/1970s, stimulated by investigations on silicone rubber tubes which were “controlling” the release of anesthetic gas at a constant rate [165], the concept of rate-controlling membrane (RCM) systems was established. Various products for local or systemic therapy have been developed, ranging from the ocular insert Ocusert® [166] via contraceptive implants [167] (e.g. Norplant®) and hydrogel implants [168] (e.g. Vantas®) to osmotic pump systems [169,170] (ALZET®, DUROS®), all of which are based on an RCM, providing a relatively constant drug rate. However, a major drawback of these devices is the need of posttreatment removal, usually demanding surgical intervention. In view of this, the use of biodegradable polymers was the next step in development after the polyhydroxy acids had entered the market [2-4]. As mentioned before, a wide range of biodegradable polymers have been synthesized by now and many of them have also been studied as biodegradable implants [4,7,9] (e.g. Zoladex® based on PLGA) or microparticles [171-173] (e.g. Decapeptyl® based on PLGA, Trenantone® based on PLA). Furthermore, lipid implants [19-21] and lipid microparticles [174] have been reported as sustained release systems for pharmaceutical proteins. However, the solid aggregate state of most applied materials complicates the formulation process and requires the injection or insertion of the implants with large needles or by microsurgery. A major improvement was therefore the development of *in situ* forming systems which are injected as low viscous drug containing solutions through standard needles [175-177]. After injection, the solidification and formation of the implant can be achieved by various strategies, ranging from *in situ* cross-linking to *in situ* phase separation [177-179]. To date, all commercially available products are based on phase separation by solvent exchange (e.g. Atridox® based on PLA in *N*-methyl-2-pyrrolidone (NMP) and Eligard® based on PLGA in NMP). In these systems, the *in situ* implant formation proceeds due to a decrease in polymer solubility when NMP diffuses into the surrounding tissue and water penetrates into the organic phase. However, the use of NMP and other organic solvents in such systems was reported to cause myotoxic effects and other undesired tissue responses [180]. Furthermore, the problems of high burst release during implant formation [180], variable implant shape and low pH values during degradation of PLGA [181-183] are still drawbacks to be overcome.

One quite different drug delivery system for sustained release which has been approved for clinical use is the multivesicular liposome concentrate DepoFoam® [184,185] (e.g. DepoCyte®). High drug loading, good tolerance and prolonged release of small drugs and macromolecules up to several weeks have been reported for this technology [184,185]. Besides other approaches to overcome the drawbacks of the widely used PLA or PLGA implants, poly(2-hydroxyoctanoic acid), called “hexPLA”, was the first viscous biodegradable polymer reported as sustained release implant injectable without the addition of solvents or with only ≤ 5 % of NMP [186,187]. Inspired by these promising results of hexPLA, viscous Lauroyl-PGAs have been investigated in this study regarding

their potential as sustained release implants. The viscosity of most Lauroyl-PGAs (esterification degree ≥ 25) allows direct subcutaneous injection through standard needles. Nevertheless, for the incorporation of dyes or spin probes, solutions in NMP were prepared and added to the polymers to a final content of 5 % organic solvent. In order to achieve a homogeneous distribution, dual asymmetric centrifugation (DAC) was applied [188]. This is an efficient but gentle mixing method which can even be used for pharmaceutical proteins without inducing protein destabilization [189].

A series of Lauroyl-PGA polyesters has been characterized by $^1\text{H-NMR}$ relaxometry and texture analysis in terms of viscosity and mechanical properties. By means of the non-invasive method of $^1\text{H-NMR}$ relaxometry, the transverse relaxation time T_2 was measured which characterizes the signal decay and describes how fast initial magnetization returns to the equilibrium state through spin-spin relaxation [190,191]. As this time constant is considerably influenced by the physical state and the mobility of protons [191-193], it was used in this study to get insight into the viscosity [194] of the semisolid polymers. The method of texture analysis was performed in order to get further information about the mechanical properties of these polymers. During the compression of a polymer by a metal probe, peak forces and mechanical work have been measured from which parameters like hardness and adhesiveness of the polymer could be calculated.

Model implants of Lauroyl-PGAs were prepared with different electron spin resonance (ESR) probes or fluorescent dyes and their release was studied by the non-invasive methods of spectral spatial ESR imaging (ESRI) and MSFI. By MSFI, model implants were monitored in whole and the overall release of the hydrophilic Rhodamine110 and the lipophilic DiI was recorded. In contrast, the method of ESRI is capable to resolve heterogeneities within the samples and provide spatial information about the distribution of electron spins and their characteristics at different locations [195]. From these characteristics, expressed by the respective ESR spectrum, information about the microenvironment inside the implant could be obtained. Particularly water penetration, polarity and pH value as well as mobility of the spin probes were monitored over time. These are important parameters with direct influence on drug release, degradation kinetics and drug stability [196]. By the use of a pH-sensitive spin probe, the process of the pH value could be assessed which is another crucial parameter during polymer degradation. It has been reported, for instance, that the pH may drop to 3 or 2 inside degrading PLGA implants [181,182]. This could be very unfavorable for the stability of incorporated proteins, peptides and small molecules [197]. Furthermore, the biocompatibility of the implant with respect to surrounding cells and tissue could be affected [182].

In addition to these *in vitro* investigations, a preliminary *in vivo* study in SKH1 mice was carried out with PGA-L25 and PGA-L95, loaded with the lipophilic fluorescent dye DiI. The mice were monitored over six months by non-invasive MSFI and sacrificed at the end of the study for *ex vivo* autopsy.

The wide range of analytical methods applied in this work provide comprehensive insight into the characteristics of poly(glycerol adipate) and its possible applications in drug delivery.

2 Materials

2.1 Polymers

2.1.1 PGA fatty acid esters

PGA polyesters have been synthesized at the Institute of Chemistry, Department of Physical Chemistry, Martin Luther University Halle-Wittenberg as described in [157].

Esterification degrees were calculated using $^1\text{H-NMR}$ spectra (see 3.1.8.1), molar mass was measured by gel permeation chromatography (Viscotek GPCmax VE 200, Malvern Instruments, Malvern, UK), equipped with a refractive index detector (Viscotek VE 3580 RI detector). For some of the polymers, the volume fractions of the fatty acid side chains were calculated by Materials Studio 4.1 (Accelrys Software, San Diego, US).

Table 2-1. PGA based polyesters used in this work. Their number average molecular weight (M_n), weight average molecular weight (M_w), polydispersity index (M_w/M_n), the exact percentage of substituted OH groups of the PGA backbone and the calculated volume fraction of the fatty acid side chains are given.

Polymer	M_n [Da]	M_w [Da]	M_w/M_n (PDI)	Substituted OH groups [mol%]	Volume fraction of fatty acids [%]
PGA-BB	3 675	8 484	2.31	0	0
PGA-BB-2*	3 403	7 261	2.13	0	0
PGA-L15	3 578	9 827	2.75	13	
PGA-L25	5 345	10 763	2.01	25	
PGA-L30	5 452	11 226	2.06	28	
PGA-L50	8 075	16 386	2.03	50	
PGA-L75	14 810	31 629	2.14	75	
PGA-L95	14 593	27 412	1.88	95	
PGA-S20	1 926	3 276	1.70	18.9	24
PGA-S50	3 602	6 927	1.92	48.3	44
PGA-S65	4 328	6 614	1.53	65.9	51
PGA-S85	7 227	14 325	1.98	85	57
PGA-B45	6 473	10 132	1.57	43.5	
PGA-B65	8 793	14 706	1.67	65	
PGA-O110	5 442	12 220	2.24	15	18
PGA-O120	5 900	12 231	2.07	23	25
PGA-O130	6 979	17 154	2.46	30	30
PGA-O170	9 690	16 178	1.67	67	50
PGA-O190	11 687	19 974	1.71	92	57

* A second batch of PGA-BB was synthesized for the polymers used in the implant study.

2.1.2 Hydroxypropyl methacrylamid (HPMA) copolymers

HPMA copolymers were synthesized at the Institute of Macromolecular Chemistry AS CR (IMC), Department of Biomedical Polymers, Prague (Czech Republic), as reported in [148,198-202]. The chemical structures are provided in the appendix (Figure 7-1 – 7-4).

Table 2-2. HPMA copolymers which were used for coating of PGA-S65 nanoparticles. M_w , PDI and some additional information about the chemical composition are denoted.

Polymer	Synonym	M_w [Da]	M_w/M_n	Characteristics
UH18	poly(HPMA-co-MA-ah-Chol-co-MA-ah-NHNH ₂)	29 800	2.0	cholesterol content 2.2 mol% hydrazide groups ~ 7 mol% 6-aminohexanoic acid spacer
UH19	poly(HPMA-co-MA-ah-Chol-co-MA-ah-NHNH ₂)	37 000	2.2	cholesterol content 4.8 mol% hydrazide groups ~ 7 mol% 6-aminohexanoic acid spacer
UH23	poly(HPMA-co-MA-ah-Chol-co-MA-ah-NHNH-Dy676)	31 000 (precursor)	1.9	cholesterol content 2.2 mol% hydrazide groups 5.5 mol% Dy676 content 0.7 wt% 6-aminohexanoic acid spacer
UH26	poly(HPMA-co-GFLG-Dox)-NH ₂	38 700	1.83	Dox content 8.5 wt% GlyPheLeuGly spacer
UH27	poly(HPMA-co-βA-Dy676)-NH ₂	20 000 (precursor)	1.12	Dy676 content 1.2 wt% β-Alanine spacer

2.2 Fluorescent dyes

Table 2-3. Fluorescent dyes. Maximum wavelengths of excitation (Ex.) and emission (Em.) are given.

Dye	Synonym	Excitation/Emission	Supplier
Nile red	9-diethylamino-5H-benzo[α]phenoxazine-5-one	Ex. 484-591 nm, Em. 529-657 nm [98]	Sigma, Taufkirchen, Germany
DiI	1,1'-Dioctadecyl-3,3,3',3'-tetramethylindocarbocyanine perchlorate (DiIC ₁₈ (3))	Ex. 549 nm, Em. 565 nm [113]	Sigma, Taufkirchen, Germany
DiR	1,1'-Dioctadecyl-3,3,3',3'-tetramethylindotricarbocyanine iodide (DiIC ₁₈ (7))	Ex. 750 nm, Em. 780 nm [113]	Invitrogen, Molecular Probes, Eugene, OR, USA
Dy676		Ex. 674 nm, Em. 699 nm	Dyomics, Jena, Germany
Rhodamine110	2-(6-Amino-3-imino-3H-xanthen-9-yl)-benzoic acid hydrochloride	Ex. 498 nm Em. 520 nm	Sigma, Taufkirchen, Germany

2.3 ESR spin probes

Table 2-4. ESR spin probes.

Spin probe	Synonym	Characteristics	Supplier
Tempol (TL)	2,2,6,6-Tetramethyl-4-hydroxy-piperidin-1-oxyl	hydrophilic	Sigma, Taufkirchen, Germany
D- ¹⁵ N-AT	4-Amino-2,2,5,5-tetramethyl-d ₁₂ -3-imidazoline-1-oxyl-1- ¹⁵ N	pH sensitive, hydrophilic	Institute of Chemical Kinetics and Combustion, Novosibirsk, Russia
HD-PMI	2-Heptadecyl-2,3,4,5,5-pentamethylimidazolidine-1-oxyl	lipophilic	Novosibirsk (see above)

2.4 Miscellaneous

Table 2-5. Further chemicals and their suppliers.

Substance	Synonym / formula	Supplier
Lutrol® F 68	Poloxamer 188	BASF, Ludwigshafen, Germany
5,10,15,20-Tetrakis(4-hydroxyphenyl)-21H,23H-porphine	THPP	Sigma-Aldrich, Taufkirchen, Germany
Calcium chloride solution	CaCl ₂	Sigma-Aldrich, Taufkirchen, Germany
Ethylendiaminetetraacetic acid disodium salt	EDTA-Na ₂	Sigma-Aldrich, Taufkirchen, Germany
Calcein disodium salt	Bis[N,N-di(carboxymethyl) aminomethyl] fluorescein disodium salt	Sigma-Aldrich, Taufkirchen, Germany
Hydoxylapatite	[Ca ₅ (OH)(PO ₄) ₃] _x	Sigma-Aldrich, Taufkirchen, Germany
Cutina® CP	Cetyl palmitate	BASF, Ludwigshafen, Germany
Lipofundin® N 20 %		B. Braun Melsungen AG, Melsungen, Germany
Dulbecco's Modified Eagle Medium	DMEM	Biochrom AG, Berlin, Germany
Fetal bovine serum	FBS	Biochrom AG, Berlin, Germany
Antibiotic-antimycotic solution	AAS	Sigma, Taufkirchen, Germany

Water was used in double distilled quality if not stated otherwise. Bidistillation was performed by a GFL bidistillator 2108 (GFL, Burgwedel, Germany). All other chemicals were of analytical grade.

3 Experimental

3.1 Preparation and characterization of nanoparticles

3.1.1 Preparation of nanoparticles

3.1.1.1 Preparation of plain nanoparticles

The nanoparticle dispersions were prepared according to an optimized interfacial deposition (nanoprecipitation) method [24,87,88]. If not stated otherwise, 10 mg of polymer were dissolved in 1 ml of acetone which was then injected slowly into 15 ml of double distilled water with a glass syringe under rapid magnetic stirring. The water was previously heated to 70 °C (Behenoyl-PGAs) or 60 °C (others), which is above the melting temperature of the fatty acid side chains. The hot nanoparticle dispersion was afterwards poured into an empty iced beaker under magnetic stirring to achieve rapid solidification. Remaining solvent and some water were removed by a rotary evaporator to obtain a 1 % dispersion (10 mg polymer/g). Storage took place at 8 °C.

For Behenoyl-PGAs, which are insoluble in acetone, dichloromethane/acetone (volume ratio 1/6) [203], tetrahydrofuran (THF), THF/ethanol (3/2 [204] and 1/1) were tested as solvents. The latter mixture was used in the following.

3.1.1.2 Preparation of loaded nanoparticles

Loaded nanoparticles were prepared according to the general procedure described for plain particles (3.1.1.1). Yet instead of dissolving the polymer in 1 ml of organic solvent, a reduced volume was firstly applied. After solution of the polymer, the required volume of stock solution, containing the drug or dye, in the same solvent was added and stirred for sufficient mixing. With this mixture, nanoprecipitation was carried out as described.

3.1.2 Coating of PGA-S65 nanoparticles

3.1.2.1 Physical coating

10 mg PGA-S65 and 20/30/50 wt% of HPMA copolymer, bearing cholesterol moieties (UH18, UH19 or UH23), were weighed together in a glass vial. At first, 1 ml of THF was applied to solve PGA-S65 under magnetic stirring and subsequently 1 ml of ethanol was added for dissolution of the HPMA copolymer. With this mixture, nanoprecipitation was carried out as described (3.1.1.1).

3.1.2.2 Covalent coating

3.1.2.2.1 Preliminary test of coating with Doxorubicin bearing UH26

The covalent coating of beforehand prepared PGA-S65 nanoparticles was firstly tested at the IMC in Prague with a semitelechelic Doxorubicin (Dox) bearing HPMA copolymer

(UH26). The primary amino group at the end of the polymer chain was used for covalent bonding of the free carboxyl groups of PGA-S65 nanoparticles. The carbodiimide coupling method was applied using water soluble *N*-ethyl-*N'*-(3-dimethylaminopropyl) carbodiimide.HCl (EDC). For this, aqueous solutions of UH26 and EDC (50-fold molar excess to polymer amino groups) and a crystal of dimethylaminopyridine were added to a corresponding amount of PGA-S65 nanoparticle suspension. Three different types of coated nanoparticles were prepared with PGA-S65/HPMA conjugate ratios of 2/1, 4/3 and 1/1 (w/w). The reaction mixture was stirred overnight at room temperature. Then low-molecular-weight compounds and possible unreacted polymer conjugate were removed by gel filtration using Sephacryl® S-300 and PBS solution (pH 7.4). The content of UH26 in coated nanoparticles was determined by amino acid analysis according to [198].

3.1.2.2 Coating with Dy676 bearing UH27

The covalent coating of PGA-S65 nanoparticles (loaded with 0.025 wt% DiR) with the Dy676 bearing HPMA copolymer (UH27) was carried out in Halle according to the above described procedure with a PGA-S65/HPMA conjugate ratio of 2/1 (w/w). The amount of EDC was raised to 100-fold molar excess to polymer amino groups. Low-molecular-weight compounds were removed by gel filtration using a PD-10 column (PD MidiTrap G-25, GE Healthcare, Little Chalfont, UK) and PBS solution (pH 7.4). The sample for *in vivo* experiments was additionally washed by centrifugal ultrafiltration (Amicon Ultra 4 ml Filters, cut off 100 kDa, Merck Millipore, Billerica, USA).

3.1.3 Photon correlation spectroscopy (PCS)

Particle size measurements by dynamic light scattering were performed in the backscattering mode (173°), using a High Performance Particle Sizer (HPPS; Malvern Instruments, Malvern, UK) or a Zetasizer Nano-ZS (Malvern Instruments), Model ZEN 3600. Nanoparticle dispersions were diluted with double distilled, filtered water (pore size 0.2 µm) to a concentration of 0.1 mg/ml and measured at 25 °C in the middle of the cuvette. Each sample was measured 4 times with 12–16 runs each. Z-average diameters and polydispersity indices (PDI) were determined by the cumulant analysis software of the instrument (Dispersion Technology Software 4.20, Malvern or Zetasizer Software 6.30, Malvern).

3.1.4 Zeta potential measurement

The zeta potential of the nanoparticles was determined by laser Doppler anemometry with a Zetamaster S (Malvern Instruments) or a Zetasizer Nano-ZS (Malvern Instruments) for the coated nanoparticles. All samples were diluted to 0.2 mg/ml with 1:10 Sørensen's phosphate buffer (pH 6.8). At Zetamaster S, 3 aliquots of every sample were measured with 5 runs each, at Zetamaster Nano-ZS, 5 measurements with 22 runs were performed for each sample at 25 °C.

3.1.5 Transmission electron microscopy (TEM)

3.1.5.1 Negative stain

The negatively stained samples were prepared by spreading 3 μl of the dispersion onto a Cu grid coated with a Formvar[®] film. Excess liquid was blotted off, the grids were washed with water, placed on a droplet of 1 % aqueous uranyl acetate and drained off after 1 min. The dried specimens were observed with a Zeiss EM 900 transmission electron microscope (Carl Zeiss SMT, Oberkochen, Germany) at an acceleration voltage of 80 kV. Electron micrographs were taken with a slow scan camera (Variospeed SSCCD camera SM-1 k-120, TRS, Moorenweis, Germany).

3.1.5.2 Freeze fracture

The samples for freeze-fracture were cryofixed using a propane jet-freeze device JFD 030 (BAL-TEC, Balzers, Liechtenstein). Thereafter the samples were freeze-fractured at -150 °C without etching with a freeze-fracture/freeze-etching system BAF 060 (BAL-TEC). The surfaces were shadowed with platinum (2 nm layer, shadowing angle 45°) and subsequently with carbon (20 nm, 90°). The replica was floated in 4 % sodium chloride, rinsed in distilled water, washed in 30 % acetone and rinsed again in distilled water. Afterwards the replica was mounted on copper grids coated with Formvar[®] films. The same microscope and camera were used as described above.

3.1.5.3 Cryo-TEM

For cryo-TEM imaging, one droplet of nanoparticle dispersion was applied in a wet chamber to a copper grid covered by a holey carbon film (Quantifoil[®] R3.5/1 Micro Tools GmbH, Jena, Germany) and excess of liquid was blotted automatically for 1 s between two strips of filter paper. Subsequently, the samples were rapidly plunged into liquid ethane (cooled to -180 °C) in a cryobox (Carl Zeiss NTS GmbH, Oberkochen, Germany). Excess ethane was removed with a piece of filter paper. The samples were transferred with a cryo-transfer unit (Gatan 626-DH) into the precooled cryo-electron microscope (Philips CM 120, Netherlands) operated at 120 kV and viewed under low dose conditions. The Images were recorded with a 1k CCD Camera (FastScan F114, TVIPS, Gauting, Germany).

3.1.6 Asymmetrical flow field-flow fractionation (AF4)

The AF4 measurements were carried out with an Eclipse[®] AF4 separation system equipped with a DAWN[®] EOS multi-angle laser light scattering (MALLS) detector (both from Wyatt, Dernbach, Germany) as described in [205] and a refractive index detector RI-101 (Shodex, Yokohama, Japan). The channel dimensions were adjusted by a trapezoidal spacer (height 350 μm , length 265 mm, largest width 21 mm) and a membrane of polyethersulfone or regenerated cellulose with a 5 kDa cut off (Microdyn-Nadir, Wiesbaden, Germany) was employed as accumulation wall. All samples were

diluted (0.1 mg/g if not stated otherwise) and measured in double distilled water which was filtered (0.1 μm , VVLP, Millipore) before and preserved with 0.02% sodium azide. During focusing (focus flow 2 ml/min) 100 μl of nanoparticle dispersion or polymer solution were injected and the nanoparticles subsequently eluted with a constant detector flow of 1 ml/min and decreasing cross flow [205]. For the polymer samples, the method cycle was adjusted to achieve a better separation for small compounds. Scattering intensities were measured by the MALLS detector at 15 different angles (between 26 and 163°) using a laser wavelength of 690 nm and change of refractive index was determined by the RI detector. Eluted fractions which were needed for further investigation, were collected at the end of the AF4 channel every 1 or 2 min.

Size calculations from the MALLS data were carried out by the Astra 4.90 software (Wyatt) using the particles mode [205]. Molecular mass of the polymer was also calculated by Astra 4.90 on the basis of the RI data.

3.1.7 Differential scanning calorimetry (DSC)

DSC measurements for Stearoyl- and Behenoyl-PGA bulk polymers were performed with a Pyris 1 DSC (PerkinElmer instruments, Rodgau, Germany) in standard aluminum sample pans. Nanoparticle dispersions (2.5 mg/ml) were measured with a VP-DSC MicroCalorimeter (MicroCal LLC, Northampton, MA, USA) which is intended to study liquid samples. Measurements were carried out in a temperature range of 10–60 °C (Stearoyl-PGAs) or 10–70 °C (Behenoyl-PGAs) at a heating rate of 1 K/min. Polymers were measured against an empty reference pan, dispersions against purified water. Three consecutive heating and cooling scans were recorded of each sample.

DSC experiments with Lauroyl- and Oleoyl-PGAs were carried out under continuous nitrogen flow using a Mettler Toledo DSC 823e module (Mettler Toledo, Gießen, Germany). Every sample was heated up to 100 °C and kept at this temperature for 20 min. The sample was then cooled to -50 °C with a cooling rate of -1 K/min. The sample was kept at -50 °C for further 20 min; afterwards the sample was heated up again to 100 °C with a heating rate of 1 K/min.

3.1.8 Proton nuclear magnetic resonance ($^1\text{H-NMR}$)

3.1.8.1 $^1\text{H-NMR}$ spectroscopy of PGA bulk polymers

$^1\text{H-NMR}$ spectra of the PGA polyesters were recorded using a Gemini 2000 spectrometer (Varian, Palo Alto, USA) operating at 400 MHz. The esterification degree of OH groups in PGA was calculated from the integrals of the peaks according to the following equation:

$$\text{Esterification degree (\%)} = [1.33 \times a / (d - 0.67 \times a)] \times 100$$

Peak a ($\delta = 0.86$): terminal CH_3 groups of fatty acid side chains; peak d ($\delta = 2.36$): CH_2 groups located in α -position to carbonyl groups. (The detailed assignment of the $^1\text{H-NMR}$ peaks to the corresponding protons in the polymer is displayed in Figure 4-9)

3.1.8.2 $^1\text{H-NMR}$ spectroscopy of nanoparticles

$^1\text{H-NMR}$ spectra were acquired from a 400 MHz spectrometer (Gemini 2000; Varian, Palo Alto, California, USA) as well as a 500 MHz spectrometer (Unity Inova 500; Varian) for the temperature controlled measurements. Bulk polymers (20 mg/ml) were measured in deuterated chloroform, nanoparticles (10 mg/ml) in double distilled water containing deuterium oxide and the sodium salt of 3-(trimethylsilyl)propionic-2,2,3,3- d_4 acid as a standard (0.75 wt% in D_2O).

3.1.9 X-ray diffraction (XRD)

3.1.9.1 Small-angle X-ray scattering (SAXS)

Small-angle X-ray scattering experiments (SAXS) were performed using a rotating copper anode Rotaflex RU-H3R (Rigaku, Tokyo, Japan) equipped with a HI-STAR 2D detector (Bruker, Billerica, USA) and a focusing X-ray optics device Confocal Max-Flux[®] (Osmic, Troy, USA) which also served as monochromator for the $\text{Cu K}\alpha_1$ radiation ($\lambda = 0.154 \text{ nm}$). The samples were sealed in glass capillaries with a diameter of 1 mm and a wall thickness of 10 μm .

3.1.9.2 Combined SAXS and Wide-angle X-ray scattering (WAXS)

X-ray patterns were measured in transmission with a stationary linear position sensitive detector ($2\theta = 0\text{-}40^\circ$) on a stage including a curved primary $\text{Ge}(111)$ monochromator and temperature control (STOE & CIE GmbH). The samples were sealed in 1.5 mm glass capillaries. $\text{Cu K}\alpha_1$ ($\lambda = 0.154 \text{ nm}$) radiation was used, and the scattering was corrected with respect to an empty capillary. The SAXS and WAXS patterns were measured simultaneously during heating and cooling. The heating rate was 1/15 K/min (5 min equilibration, 10 min exposition for each pattern) for the applied temperature protocol.

3.1.9.3 Synchrotron SAXS and WAXS measurements

Nanoparticle morphology was further studied by simultaneous SAXS and WAXS experiments using synchrotron radiation at the HASYLAB synchrotron laboratories (beamline A2) at Deutsches Elektronen Synchrotron DESY, Hamburg. The radiation wavelength was $\lambda = 0.154 \text{ nm}$. Temperatures were varied between 10 $^\circ\text{C}$ and 60 $^\circ\text{C}$ by JUMO IMAGO 500 multi-channel process and program controller (JUMO, Fulda, Germany). Obtained curves were corrected by background subtraction and, if necessary, Lorentz correction ($I(q) \rightarrow s^2I(q)$) was applied and curves were smoothed [206].

3.1.10 Multispectral fluorescence imaging (MSFI) of Nile red loaded particles

Nanoparticles loaded with 0.2 % of the fluorescence dye Nile red were prepared (see 3.1.1.2) and studied by MSFI. Fluorescence spectra were measured using the MaestroTM in-vivo imaging system (Cambridge Research & Instrumentation, Woburn, USA). A green filter set with an excitation band-pass filter of 503 to 555 nm and a 580 nm longpass

filter for emission were used. The tunable filter was automatically stepped in 2 nm increments from 550 to 800 nm while the Maestro™ multispectral imaging system captured images at each wavelength interval with constant exposure times.

3.1.11 Determination of drug loading

The study of the loading capacity of PGA nanoparticles with lipophilic molecules was carried out with the fluorescent dye DiI and with the fluorescent drug 5,10,15,20-Tetrakis(4-hydroxyphenyl)-21*H*,23*H*-porphine (THPP). In order to determine the free content of dye or drug which was not included into the nanoparticles during the preparation process, size exclusion chromatography (SEC) by gel filtration was applied to separate the loaded nanoparticles from the remaining small molecules. The separation was carried out with PD-10 Desalting Columns (GE Healthcare, Little Chalfont, UK) prepacked with Sephadex® G-25 M (cross-linked dextran, exclusion limit 5×10^3 Da). SEC separates molecules on the basis of differences in size. Molecules larger than the largest pores in the Sephadex® matrix are excluded from the matrix and are eluted first. Molecules smaller than the largest pores will penetrate the pores to varying extent. They have a larger accessible column volume than the large molecules and therefore they elute later just before one total column volume of elution medium has passed through the column [207].

The PD-10 columns contain UV absorbing stabilizers and preservatives (0.15 % Kathon™ CG) and therefore have to be equilibrated with buffer or water first. In this experiment, pure water was used for equilibration and elution because salts from buffer would be hindering the following experimental procedure. After equilibration with 25 ml of water, 1 ml of the nanoparticle sample was applied on top of the column, 1.5 ml of water were added after the sample had entered the packed bed completely and subsequently 3 ml of water were applied for elution. The first 2.8 ml of the eluate were discarded and subsequently 3 ml of eluate collected. After complete elution, the column was again washed with 30 ml of water. Three aliquots of each nanoparticle batch were separated from free drug or dye according to this protocol. The collected samples were afterwards freeze-dried (Christ ALPHA 1-2, Martin Christ, Osterode, Germany) overnight together with 3 reference tubes, each containing 1 ml of untreated nanoparticle sample. The freeze-dried preparations were then dissolved in 1 or 2 ml of acetone and measured in a black 96-well plate (PP-Microplate, F-shape, Greiner bio-one, Frickenhausen, Germany) with a fluorescence plate reader (NOVOstar, BMG LABTECH, Ortenberg, Germany). Three wells of each sample and reference were measured in triplicate. The fluorescence dye DiI was excited at 544 nm and the emission was measured at 620 nm. These were not the optimum wavelengths for the dye; however the most suitable of the available filters in the NOVOstar plate reader. For THPP, the absorption wavelength was determined by UV/VIS spectroscopy (Spekol® 1200, Analytik Jena AG, Jena, Germany) and the emission range (maximum 653 nm) was taken from literature [208,209]. The excitation took place at 380 nm and emission was measured at 620 nm. The percentage

of effectively loaded drug or dye was calculated with respect to the unseparated references. In order to ensure the linear dependence of the emitted fluorescence from the applied dye or drug concentration, calibration curves were recorded in triplicate.

3.1.12 Hemolytic activity

Human whole blood (stored in EDTA tubes for anti-clotting) was separated from plasma by centrifugation at 1000*g*. The remaining RBCs were washed and diluted with isotonic phosphate buffered saline (PBS, 137 mM NaCl, 2.7 mM KCl, 10.1 mM Na₂HPO₄, 1.8 mM KH₂PO₄, pH 7.4) to obtain a 2 % (v/v) RBC suspension. Nanoparticle samples (10 mg/ml) were made isotonic by adding sorbitol (5 % w/v). PBS was used as zero value and a 2 % aqueous sodium dodecyl sulfate solution served as 100 % value. The samples were added 1:1 (v/v) to the RBC suspension and incubated at 37 °C for 1 h in an end-over-end shaker. The intact RBCs were removed by centrifugation (850*g*) to be separated from hemoglobin. To clear the supernatant from nanoparticles, a mixture of ethanol/HCl (40:1, v/v) was added 1:4 (v/v) and centrifuged for 15 min at 850*g*. Thereafter, the percentage of hemoglobin in the supernatant was determined by UV/VIS spectroscopy at 398 nm (Spekol® 1200, Analytik Jena AG, Jena, Germany).

3.1.13 Cell culture studies

3.1.13.1 Cell culture

HepG2 cells were grown in Dulbecco's Modified Eagle Medium (DMEM) supplemented with 10 % fetal bovine serum (FBS) and 1 % antibiotic-antimycotic solution (AAS) at 37 °C in a humidified 5 % CO₂/ 95 % air atmosphere using a NUAIRE DH Autoflow incubator (AuAire Corp., Plymouth, USA). Almost confluent cells were harvested by trypsin. For this, medium residues were firstly removed by rinsing the adherent cells with sterile PBS, followed by the incubation with trypsin/ EDTA (0.25 %/ 0.02 %) for 5 min at 37 °C. The reaction was stopped by adding DMEM containing 10 % FBS. After centrifugation of the cell suspension for 10 min at 250 rpm (~6*g*, Z 400 K, Hermle, Wehingen, Germany) the HepG2 cells were resuspended in culture medium at a density of 10⁴ cells/ml.

3.1.13.2 Cell viability and proliferation

Cell viability and cell numbers after 24 h incubation with the nanoparticles were determined by QBlue viability assay (QBlue Cell Viability Assay Kit, BioCat, Heidelberg, Germany) and a modified LDH cytotoxicity kit II (BioVision, Mountain View, USA).

Prior to these experiments, the optimal number of cells to seed was defined. For this, different numbers of cells in DMEM supplemented with 10 % FBS and 1 % AAS were seeded in black 96-well-plates (Cellstar®, Greiner Bio-One GmbH, Frickenhausen, Germany) and incubated for 3 d which covered the duration of the planned assays. Then 10 µl of QBlue reagent were added to each well and the plate was incubated for additional 2 h. Subsequently, after excitation at 544 nm, the fluorescence intensity was

measured at 590 nm emission using a plate reader (FLUOstar OPTIMA, BMG LABTECH, Offenburg, Germany). The relationship between seeded cell number per well and relative fluorescence was determined.

3.1.13.2.1 QBlue cell viability assay

5×10^3 cells per well (100 μ l) in DMEM supplemented with 10 % FBS and 1 % AAS were seeded in a black 96-well-plate (Cellstar®) and incubated for 2 d to let them grow adherent. Thereafter, the medium was aspirated. For the samples, 1 % (10 mg/ml) of nanoparticle suspension was diluted 1:10 with sterilized PBS. 25 μ l of this suspension was mixed with 75 μ l of pure DMEM and added to the cells, which leads to a final concentration of 250 μ g/ml. With this, the cells were further incubated for 24 h. Subsequently, 10 μ l of QBlue reagent were applied and the plate was incubated for additional 2 h. The fluorescence intensity was then measured at 590 nm emission after excitation at 544 nm using a plate reader (FLUOstar OPTIMA). To investigate the concentration dependence, the experiment was repeated with a concentration of 100 μ g/ml nanoparticles. Additionally, the assay was carried out with DMEM supplemented with 10 % of FBS for dilution of the samples to provide a control value of optimal growth conditions for the cells.

3.1.13.2.2 Lactate dehydrogenase cytotoxicity assay (LDH)

To estimate the cell quantity, a modified lactate dehydrogenase (LDH) cytotoxicity assay kit II was conducted according to Niepel *et al.* [210]. For this, HepG2 cells were grown and incubated with the nanoparticle samples as in the QBlue assay. The medium was removed carefully and the wells were washed with 200 μ l of PBS. Thereafter, 100 μ l of 0.5 % (v/v in PBS) Triton® X-100 were added to each well for lysis of all viable cells. Then the culture plate was placed on a shaker (IKA KS 260 control, Staufen, Germany) at 150 rpm and incubated for 30 min at room temperature. Subsequently, 10 μ l of the supernatant were transferred to a transparent 96-well-plate and 100 μ l of the LDH reaction mix were added to each well. The plates were wrapped up in aluminum foil and incubated for 30 min at room temperature. To finish the reaction, 10 μ l of stop solution from the LDH kit were added to each well. The absorbance of the solution was measured at 450 nm using a plate reader (FLUOstar OPTIMA).

3.1.14 In vivo experiments

All *in vivo* experiments complied with the regional guidelines for animal testing and animal care and were approved by the responsible animal care and use committee.

3.1.14.1 Animals and tumor monitoring

Distribution studies of the different nanoparticle samples were performed in female hairless, immunocompetent SKH1-*Hr^{hr}* mice (Charles River, Wilmington, USA; about 4 months old). Tumor accumulation was studied in female athymic Nude-Foxn1 mice

(Harlan Winkelmann, Borcheln, Germany; about 3 months old) which were inoculated s.c. with 5×10^6 colorectal carcinoma HT29 wild type cells [120] on the left flank about 4 weeks prior to nanoparticle injection. All mice were kept under controlled conditions (12 h light/dark cycle, 24 °C, feed and water *ad libitum*).

The tumor growth was monitored initially every 2-3 d, later every day by measuring the dimensions (length l and width w) with a sliding caliper. the tumor volume was estimated according to Euhus *et al.* [211] and Tomayko *et al.* [212] using the following equation

$$V = l * w^2 * \frac{\pi}{6}$$

Equation 3-1. Approximation of tumor volume through measurement of tumor length (l) and width (w).

3.1.14.2 Injection protocol

The mice were randomized in different groups according to weight (SKH1) or tumor volume (Nude-Foxn1) at the day of injection. Each mouse was slowly injected i.v. into the tail vein with 100 μ l of the respective sample as a single dose (Sterican® 30 G needles, B. Braun, Melsungen, Germany). 24 h after the injection, one mouse of each group was sacrificed and autopsied in order to get information about the distribution of the dyes in the organs after 1 d. The other mice were further monitored for 2-3 weeks, depending on the tumor burden. During *in vivo* imaging the mice were anesthetized with an isoflurane (Forene®, Abbott, Germany)/oxygen mixture (inhalation narcosis system, Drägerwerk AG, Lübeck, Germany) and placed on a tempered plate (35 °C) to prevent cooling of the body temperature. Mouse weight was controlled initially every 2-3 d, later every day. At the end of the study, mice were sacrificed by cervical dislocation and autopsied. Internal organs were removed and their fluorescence intensity measured *ex vivo*.

Table 3-1. Applied samples and number of injected mice for each group of the in vivo study.

Sample	Included fluorescent dyes	Injected mice
PGA-S65 uncoated	DiR	4 SKH1 + 4 Nude-Foxn1
PGA-S65 + UH23 (physical coating)	DiR + Dy676	4 SKH1 + 4 Nude-Foxn1
PGA-S65 + UH27 (covalent coating)	DiR + Dy676	4 SKH1 + 5 Nude-Foxn1
UH23 polymer	Dy676	2 Nude-Foxn1

All samples were freshly prepared (1 wt% in bidistilled water) and made isotonic with 5 % sorbitol. The samples S65+UH23 and S65+UH27, used for the Nude-Foxn1 mice, were washed with PBS buffer by ultrafiltration (Amicon Ultra 4 ml Filters, cut off 100 kDa, Merck Millipore, Billerica, USA).

3.1.14.3 *In vivo* and *ex vivo* multispectral fluorescence imaging

In vivo and *ex vivo* MSFI was performed by the Maestro™ in-vivo imaging system (Cambridge Research & Instrumentation, Woburn, USA). In order to get a combined picture of both fluorescence dyes used in this study, each image cube was acquired with two filter sets in the range of 680 to 950 nm. For the Dy676 signal a red filter set (excitation filter 615-665 nm, emission filter 700 nm longpass) and for DiR a near-infrared (NIR) filter set was employed (excitation 710-760 nm, emission 800 nm longpass). The Maestro™ software (version 2.10.0) was used for recording and analysis of the overlaid image cubes. Single component images of DiR and Dy676 were calculated by the software based on the respective spectra and were overlaid afterwards to obtain a combined image of both dyes. The intensity distribution of the single component images in this work are displayed in the jetblack color profile.

Tumor accumulation of the different nanoparticle samples was estimated according to Hoffmann *et al.* [119] from the unmixed single component images:

$$TAV = \frac{\text{proportion of fluorescence signal}}{\text{proportion of fluorescence area}}$$

$$\text{proportion of fluorescence signal} = \frac{I_{\text{tumor}}}{I_{\text{mouse}} - I_{\text{tumor}}}$$

$$\text{proportion of fluorescence area} = \frac{\text{area}_{\text{tumor}}}{\text{area}_{\text{mouse}} - \text{area}_{\text{tumor}}}$$

$$TAV = \frac{I_{\text{tumor}} \times (\text{area}_{\text{mouse}} - \text{area}_{\text{tumor}})}{\text{area}_{\text{tumor}} \times (I_{\text{mouse}} - I_{\text{tumor}})}$$

Equation 3-2. Calculation of the tumor accumulation value (TAV) according to [119].

3.1.15 *Ex vivo* experiments

3.1.16 Investigation of “bone targeting”

In order to get a deeper insight into the phenomenon of nanoparticle accumulation in or on bones, two methods to determine Ca²⁺ binding and a binding assay with hydroxylapatite (HA) were performed with PGA-S65 nanoparticles.

The Ca²⁺ binding test was carried out according to [213] and [214]. Both methods were based on incubation of nanoparticles with Ca²⁺, followed by centrifugation (MiniSpin®, Eppendorf, Hamburg, Germany and Avanti® J-20XP, Beckmann Coulter, Krefeld, Germany) and complexometric titration of the free Ca²⁺ with Ethylendiaminetetraacetic acid disodium salt (EDTA-Na₂). The first method was performed by back titration against calcein solution as indicator; the second method used direct titration with Eriochrome Black T solution as indicator.

The HA binding assay was modified after [215]. In brief, 400 μ l of different concentrations (0.0625-0.625 mg/ml) of DiI loaded PGA-S65 nanoparticles (0.25 wt% dye/polymer, z-average 156 nm, PDI 0.067) in PBS (pH 7.4) were added to 2.5 mg of HA powder. For comparison, cetyl palmitate SLNs of the same particle size (z-average 155 nm, PDI 0.087) were employed (prepared by high pressure homogenization, stabilized by 2.5 wt% Poloxamer 188) and treated in the same way.

The mixtures were incubated in an end-over-end shaker for 1 h at room temperature and subsequently centrifuged at low speed (MiniSpin[®], Eppendorf, 0.8 rpm \sim $4.3 \cdot 10^{-5}g$) for 2 min. The fluorescence intensity of the supernatant was measured with a microplate reader (NOVOstar, BMG LABTECH, Ortenberg, Germany) in a black 96-well plate (Greiner bio-one, Frickenhausen, Germany) at 620 nm after excitation at 544 nm. Each concentration was prepared and measured in triplicate. The content of remaining nanoparticles in the supernatant was calculated from the fluorescence intensities in reference to equally treated blank samples without HA. Linearity of fluorescence vs. concentration was tested up to 0.7 mg/ml by calibration.

To investigate the influence of the applied HA amount in this experiment, the same procedure was carried out with 1 mg, 2.5 mg and 5 mg of HA incubated with a medium concentration of nanoparticles (0.3125 mg/ml).

3.2 Characterization and preparation of implants and applied polymers

3.2.1 Characterization of Lauroyl-PGA bulk polymers

3.2.1.1 ¹H-NMR relaxometry

¹H-NMR relaxation experiments were carried out with a 20 MHz NMR benchtop system (Maran DRX2, Oxford Instruments Molecular Biotools, Abingdon, UK). The T₂ relaxation decays of the Lauroyl-PGA bulk polymers were determined with the spin echo technique by applying the Carr-Purcell-Meiboom-Gill (CPMG) pulse sequence [216]. The measurements were performed at 25 °C with 256 echoes per pulse sequence and a relaxation delay time of 2 s. Each sample was measured in triplicate with 512 repetitions per measurement. The obtained decays were fitted with the program WinDXP (Oxford Instruments) by inverse Laplace transform and the T₂ distributions were calculated in the relaxation time range from 10 μ s to 2 s.

3.2.1.2 Texture analysis

Texture analysis of bulk polymers was conducted by a Brookfield CT3[™]-4500 Texture Analyzer (Brookfield Engineering Laboratories, Middleboro, USA) equipped with a cylindrical TA44 probe of 4 mm diameter. The measuring parameters were set as follows: Compression mode, 1 cycle, speed 0.3 mm/s for compression and retraction, data recording 20 points/s, trigger point 0.004 N, penetration depth 1.5 mm. Recording

and data processing was carried out with the software TexturePro CT V1.4 Build 17 (Brookfield). For each polymer 3-5 compression cycles were recorded.

3.2.2 Preparation of implants

For both applied investigation methods, electron spin resonance (ESR) imaging and MSFI, reporter molecules as model drugs had to be incorporated into the polymers. This was achieved by preparing solutions of the substances in N-methyl-2-pyrrolidone (NMP) which were then added to the polymer with a final content of 5 wt% NMP. The ESR spin probes were applied to final concentrations of 1 mM; for MSFI 1 $\mu\text{g/g}$ DiI and 0.5 $\mu\text{g/g}$ Rh110 were used. To achieve homogeneous distribution, the mixing of the NMP solutions with the polymers was carried out by dual asymmetric centrifugation using a SpeedMixer™ DAC 150 SP (Hauschild, Hamm, Germany).

3.2.3 *In vitro* investigation of implants by spectral spatial ESR imaging (ESRI)

For ESRI, PGA-L30 containing either Tempol (TL) or a mixture of HD-PMI and D-¹⁵N-AT was used. 100 μg of each sample were placed into the cuboidal, one side open cavity of a sample holder which was specially designed and manufactured for this purpose.

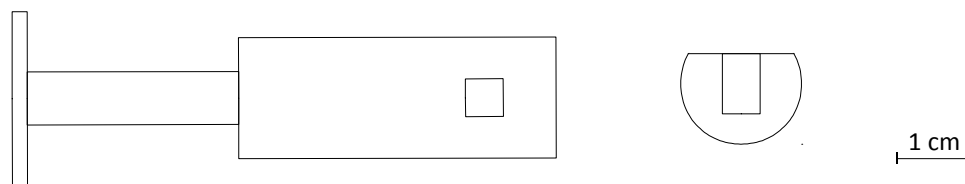


Figure 3-1. Sample holder for ESRI of implants in top view and cross section (at the position of the cuboidal cavity which holds a sample volume of 200 μl). The nose at the end of the holder ensures exact positioning inside the resonator.

The sample holders were exposed to buffer solution (PBS 1:10, pH 7.4 + 0.02 % sodium azide + 0.01 % Polysorbate 80) which was kept in a shaking water bath (SW 23, Julabo, Seelbach, Germany) at 37 °C and 26 rpm. Each sample was prepared at least twice. The samples were taken out of the buffer at dedicated time points and measured by ESRI after removing excess buffer from the container. Measurements were performed by an L-band ESR spectrometer with a 2D tomography device (MagnetTech, Berlin, Germany), operating at a microwave frequency of about 1.1-1.3 GHz. Measurement parameters were used as follows: attenuation 6 dB, B_0 -field 49.00-49.11 mT, scan range 8 mT, scan time per projection 60 s, modulation amplitude 0.1 mT, data points per projection 1024, 31 projections/6 missing projections. Data recording was carried out by the program Cu3 v6.1 (MagnetTech). Image reconstruction yielded spectral-spatial images of 512 \times 512 points. From these contour plots, ESR spectra of individual image layers were extracted and analyzed by the fitting software MagicPlot Student (Magicplot Systems, Saint Petersburg, Russia).

The rotational correlation time τ_R of TL was calculated from the parameters of the first derivative ESR spectrum according to the empirical formula [217,218]

$$\tau_R = 6.5 * 10^{-10} * \Delta B_0 (\sqrt{h_0/h_{-1}} - 1)$$

Equation 3-3. Calculation of rotational correlation time τ_R [s] from the line width of the central line (ΔB_0 , [mT]) and the amplitudes of the central (h_0) and the high-field line (h_{-1}).

where ΔB_0 is the line width of the central line, h_0 is the height of the central line and h_{-1} is the height of the high-field line. This formula allows the estimation of τ_R for fast isotropic motions ($\tau_R \leq 3$ ns).

The pH value inside the implant was calculated from the hyperfine splitting (distance between high-field and low-field line in ESR spectrum) of the pH-sensitive nitroxide D-¹⁵N-AT. A calibration curve of the hyperfine splitting of D-¹⁵N-AT as a function of pH was determined beforehand under equal measurement parameters. To avoid influence of altering ionic strength, the above mentioned buffer medium was applied for the calibration curve and its pH adjusted by adding NaCl containing HCl solution of the same ionic strength.

3.2.3.1 *In vitro* release study by multispectral fluorescence imaging

PGA-L25, -L30, -L50 and -L95 were used for the *in vitro* release study by MSFI. All samples contained the fluorescence dyes DiI and Rh110 as model drugs. 60 μ g of each sample were placed into a one side open container, covered by a polyethylene terephthalate (PET) net and exposed to buffer solution (PBS 1:10, pH 7.4 + 0.02 % sodium azide + 0.01 % Polysorbate 80). The buffer was kept in a shaking water bath (SW 23, Julabo, Seelbach, Germany) at 37 °C and 26 rpm. Each sample was prepared in triplicate. The samples were removed from the buffer at dedicated time points and measured by a Maestro™ *in-vivo* imaging system (Cambridge Research & Instrumentation, Woburn, USA). In order to get combined pictures of both fluorescence dyes, each image cube was acquired with two filter sets in the range of 500 to 800 nm. For Rh110, a blue filter set (excitation bandpass filter 445-490 nm, emission filter 515 nm longpass) and for DiI a green filter set (excitation bandpass filter 503-555 nm, emission filter 580 nm longpass) was employed. The tunable filters were automatically stepped in 10 nm increments while the Maestro™ imaging system captured images with adjusted exposure times for each filter set. The Maestro™ software (version 2.10.0) was used for recording and analysis of the overlaid images.

3.2.4 Animal care and *in vivo* multispectral fluorescence imaging

All *in vivo* experiments complied with the regional guidelines for animal testing and animal care and were approved by the responsible animal care and use committee. The *in vivo* study was performed in four healthy female nude mice (SKH1-*Hr^{hr}*, about 2-3 months old) which were kept under controlled conditions (12 h light/dark cycle, 24 °C, feed and water *ad libitum*). The polymeric implants (about 50 μ l) were injected subcutaneously on the inner side of the thighs. Each mouse was injected on the left thigh

with a PGA-L25 implant and two mice (mice 3 & 4) additionally with a PGA-L95 implant on the right thigh. All implants contained 1 µg/g of the fluorescence dye DiI. The mice were monitored for 6 months using the above described Maestro™ in-vivo imaging system with the green filter set (see 3.2.3.1). During *in vivo* imaging the mice were anesthetized with an isoflurane/oxygen mixture and placed on a tempered plate (35 °C) to prevent cooling of the body temperature. Mouse weight was controlled initially every 2-3 d, later every week. After 6 months, mice were sacrificed by cervical dislocation and autopsied. Remaining implants were taken out and fixed in formalin (5 wt% in PBS).

3.2.5 *Ex vivo* investigation of implants by confocal laser scanning microscopy

The fixed implants were investigated by confocal laser scanning microscopy (CLSM) using a Leica TCS SP2 DM IRE2 (Leica Microsystems, Wetzlar, Germany), equipped with an HCX PL APO 63x1.2 W objective. Fluorescence and reflection images were recorded in parallel by excitation at 543 nm (Helium-Neon laser) and detection at 580-620 nm (fluorescence) and 540-550 nm (reflection).

4 Results and discussion

4.1 PGA based nanoparticles

4.1.1 Preparation of nanoparticles

Polymer nanoparticles have been prepared by an optimized interfacial deposition method [87]. As in the commonly used procedure, surfactants were needed to stabilize the nanoparticles of PGA-fatty acid esters with high esterification degrees [24], the preparation method has been modified in this study. It has been discovered that the implementation of a heating and cooling step (as described in 2.2.1) lead to stable, self-stabilizing nanoparticles with all tested Lauroyl-, Stearoyl- and Oleoyl-PGA polyesters. For Behenoyl-PGAs, which are insoluble in acetone, further modification was necessary and another applicable organic solvent had to be found. The interfacial deposition method requires a semi-polar, water miscible solvent with adequate solubility of the polymer and rapid diffusion into water. Decreased miscibility with water increases the interfacial tension and thus increases the resulting size of the particles [219]. The tested solvents dichloromethane/acetone (volume ratio 1/6) [203], THF and THF/ethanol (3/2) [204] all showed sufficient solubility of Behenoyl-PGA. But due to the reduced miscibility with water they lead to bigger particles (in descending order). Therefore, the amount of ethanol in the mixture with THF was increased. The ratio THF/ethanol 1:1 was found to be the best compromise between solubility of polymer (owing to THF) and rapid diffusion of the solvent into water (enhanced by ethanol). With this solvent mixture and the optimized preparation method, Behenoyl-PGA nanoparticles could be prepared for the first time.

4.1.2 Photon correlation spectroscopy

Particle sizes were measured by dynamic light scattering using PCS. PCS enables fast, reproducible measurements of intensity weighted hydrodynamic mean diameters, especially for particles in the nanoscale range. The size of nanoparticles plays an important role for vascular extravasation and tumor accumulation. Figure 4-1 depicts the z-averages and polydispersity indices (PDI) for all nanoparticles prepared by the above described standard procedure. With 80-200 nm, the particles were in the optimal range for tumor targeting [86,95,220] and mostly smaller than those previously reported [24]. PDI values < 0.15 show a narrow particle size distribution for all prepared batches. By modification of the preparation conditions, mainly variation of the acetone volume, the particle sizes could be adjusted according to the requirements for a specific experiment. For instance, the z-average of PGA-S65 nanoparticles could be decreased from about 136 nm to 92 nm by dissolving the polymer in 4 ml of acetone instead of 1 ml.

Some of the polymers with low substitution degrees formed smaller particles than the unsubstituted PGA backbone (Figure 4-1). This indicates that the interactions of fatty acid chains within the particle core enhance the packing of the particles. With increasing esterification degree, however, the particle sizes tend to increase for all tested types of fatty acid side chains. This could be either due to the bigger space occupied in the particle core by the acyl groups or a result of an increased aggregation number [24]. The chain length of the fatty acid has – in contrast to the esterification degree – no clear impact on the particle size. The preparation of several particle batches showed good reproducibility of z-average and PDI for all Lauroyl-, Stearoyl- and Behenoyl-PGA particles. The variability of the particle sizes for the Oleoyl-PGAs, particularly for PGA-O130, was unexplainably much higher, although working with constant parameters and conditions.

During storage at 8 °C, particle sizes and PDI of Lauroyl-, Stearoyl- and Behenoyl-PGA nanoparticles were stable for at least 5 months without significant changes. Exceptions were PGA-S50 and PGA-S20 nanoparticles whose z-averages started to increase within the second (PGA-S50) or fourth month (PGA-S20) (data not shown).

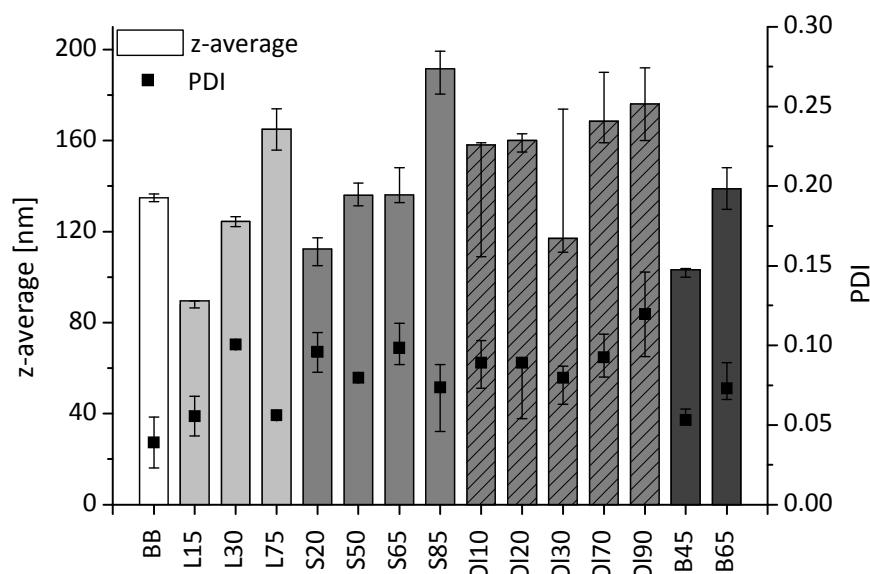


Figure 4-1. Influence of fatty acids and their esterification degree on particle size (determined by PCS): median and range of z-average and polydispersity index (PDI) are shown respectively ($n \geq 3$).

Particle size measurements were also applied to follow the coating reaction of PGA-S65 particles with HPMA copolymers (data not shown).

The physical coating with UH18 or UH19 increased the z-average diameter of PGA-S65 nanoparticles by about 10-20 nm. This is most likely a combined effect of the attached polymer shell on the outside and the cholesterol anchor molecules inside the particles.

For the covalently coated particles, in contrast, no significant increase in particle size was observed. For this, the following explanation could be considered: The plain PGA-S65 nanoparticles contain several carboxylic groups, thus the structure could be slightly expanded due to solvation of these groups in water. By means of the coating reaction,

amide bonds were formed accompanied by a drastic decrease in number of free solvated carboxyl groups. Thereby the hydrophilicity decreased and with it the size of the nanoparticles. Eventually, this reduction in particle size could be approximately compensated by the size effect of the attached polymer layer.

4.1.3 Zeta potential measurement

The zeta potential is an important parameter for the stability and biodistribution of colloidal dispersions. In general, high surface charges lead to electric repulsion between particles and thus prevent their aggregation [221]. For most PGA based nanoparticles highly negative zeta potentials have been measured (Figure 4-2) which is favorable for particle stability. The negative charge of the particles can be attributed to free terminal carboxyl end groups of the polymer backbone. According to synthesis of PGA, there are vinyl end groups (Figure 1-1) which will mostly convert into carboxyl groups because of hydrolysis [157-159]. The zeta potential tends to be more negative with increasing particle size which could be caused by an increased number of aggregated polymer chains. Besides, the zeta potential could be influenced by different internal structures of the particles. For PGA-S20 nanoparticles the lowest values have been measured. This could promote their accumulation and therefore lead to reduced storage stability (as mentioned in 4.1.2).

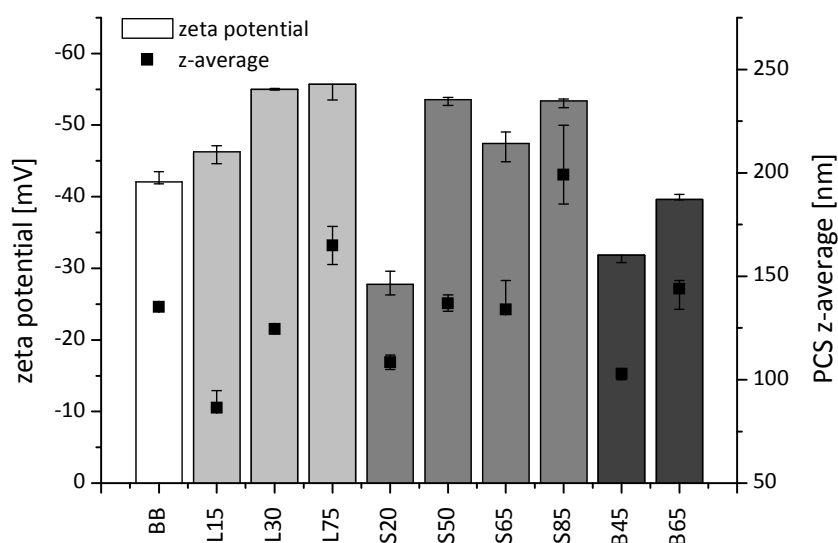


Figure 4-2. Zeta potential and z-average (from PCS) of PGA nanoparticles: median and range are shown respectively.

Besides the characterization of the plain nanoparticles, zeta potential measurement was used as an indicator for the success of the coating reactions with HPMA copolymers (Figure 4-3). With about -60 mV, the zeta potential of plain PGA-S65 nanoparticles prepared according to the method of the physically coated samples was highly negative. An addition of 20 wt% of the coating polymers UH18 or UH19 during preparation elevated the zeta potential to about -14 or -17 mV, indicating a quite successful coating reaction. An increase of the coating polymers to 50 wt% showed only slight

improvement by about 6 or 7 mV. A closer look suggests an almost linear raise for UH18 and a more distinct step for UH19 from 20 wt% to 30 wt%. This suggests that 20 wt% of UH18 and 20-30 wt% of UH19 are able to cover the surface of the PGA-S65 nanoparticles and thus shield their negative charge to a large extent. The only small additional effect of higher amounts of coating polymer indicates just an increase in coating layer thickness. These are, however, only vague considerations and should be investigated in more detail.

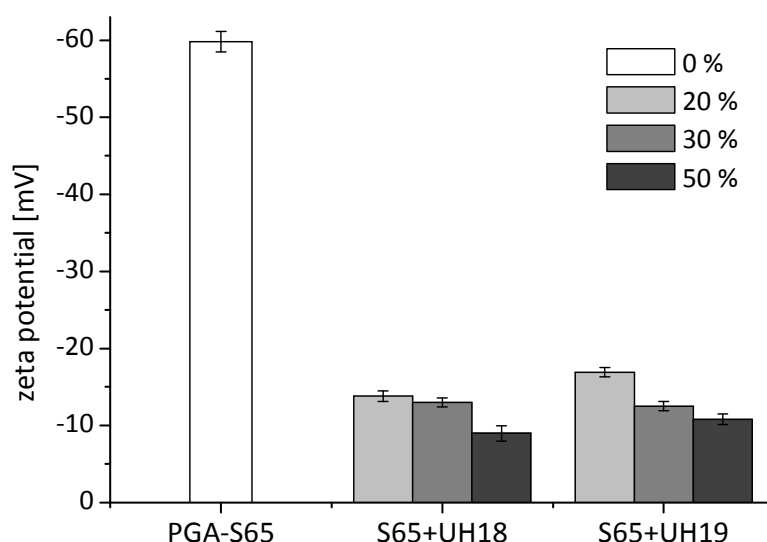


Figure 4-3. Zeta potential of physically coated PGA-S65 nanoparticles and uncoated PGA-S65 nanoparticles prepared by the same preparation method.

For the covalently coated nanoparticles, the zeta potential even dropped close to zero (-0.2 mV) after the coating reaction with UH26 (data not shown; data acquired at IMC in Prague). This points to an almost complete conversion of negatively charged carboxyl groups into amide bonds with the amino groups of the HPMA copolymer. For UH27, however, the zeta potential was only raised to -11.1 mV, indicating that the coating reaction did not proceed quantitatively with this polymer.

4.1.4 Transmission electron microscopy

Not only particle size but also particle shape plays a key role for the *in vitro* and *in vivo* behavior of nanoparticles. Transmission electron microscopy (TEM) of negatively stained and freeze-fractured samples as well as cryo-TEM micrographs visualized the particles and provided surprising information about morphology and structure. Kallinteri *et al.* reported that the shape of PGA based nanoparticles was spherical [24]. In this study, however, it was shown that the esterification degree of fatty acids strongly influenced the particle shape.

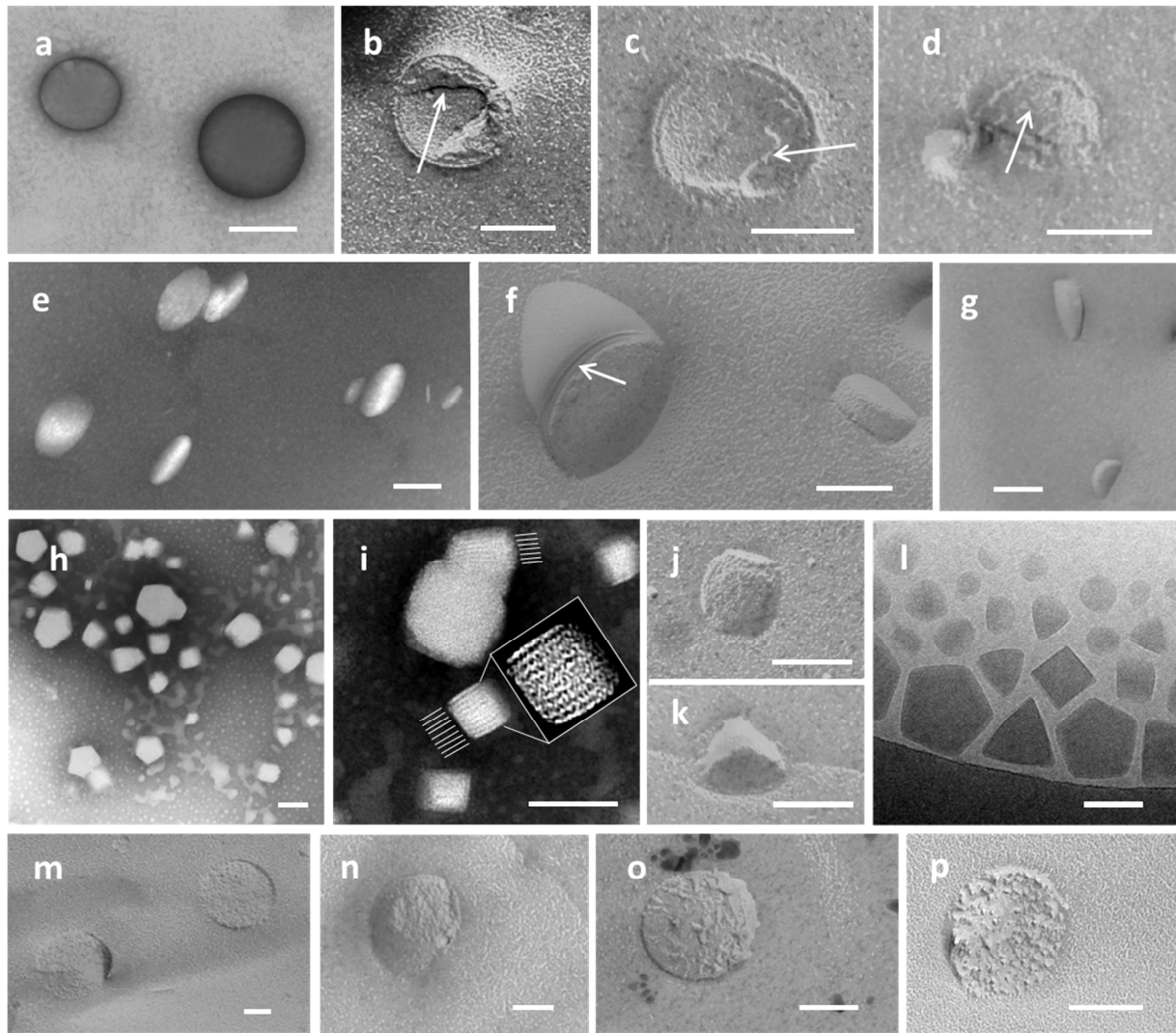


Figure 4-4. Transmission electron micrographs of nanoparticles; white bars indicate 100 nm, arrows and small bars mark layered structures. (a) Negatively staining TEM of PGA-S85. (b) Internal structure of PGA-S85 after freeze fracture. (c,d) Freeze fractured PGA-S65. (e) Negatively stained PGA-S50. (f,g) Freeze fractured PGA-S50. (h,i) Negatively stained PGA-S20. (j,k) Freeze fractured PGA-S20. (l) Cryo-TEM of PGA-S20. (m,n) Freeze fractured PGA-O120. (o,p) Freeze fractured O170.

Figure 4-4a is a negatively stained TEM image showing the typical spherical morphology of PGA-S85 nanoparticles in an aqueous suspension. According to surface energy minimization this is the classical structure for particulate systems. A freeze fracture image (b) depicts that a lamellar order is present inside the nanoparticles (indicated by an arrow), visible as terraces and steps in the micrograph. These could indicate an onion like structure, as it has been proposed for spherical smectic nanoparticles as well [56]. The same structures were found for PGA-S65 (c,d) as well. PGA-S50 nanoparticles (e-g), especially the smaller ones, showed disk-like shapes, larger particles were mostly ellipsoid. The flat shapes could promote the accumulation of PGA-S50 particles into stacks, leading to reduced storage stability (as mentioned in 4.1.2). Micrographs of freeze fractured particles in lateral exposure also indicate a structure with several layers (f). Surprisingly, negatively stained TEM images of PGA-S20 nanoparticles (h,i) revealed

diverse non-spherical shapes with linear borders and defined geometries. The larger ones could mostly be detected as pentagons, the smaller ones as square-like or rhombic shapes. To exclude the possibility of preparation effects, new batches of PGA-S20 nanoparticles were investigated by freeze fracture TEM and cryo-TEM. Both methods support the above mentioned findings (j-l). Especially the cryo-TEM images (l) nicely showed triangles, squares, and pentagons located at the edge of the hole of the carbon film. The polygons were arranged along the fringe of the hole due to the preparation procedure when filling the film holes with the aqueous nanoparticle suspension (effect of blotting [222]). As all TEM methods lead to two-dimensional projections, it is often difficult to distinguish between flat or bulky nanoparticles. The preparation techniques of the samples might lead to a preferential orientation of the particles with the largest surface displayed in the micrographs. To get more information about the third dimension of PGA-S20 nanoparticles, AF4/MALLS measurements combined with PCS were carried out afterwards (4.1.5). The lateral dimensions of the PGA-S20 nanoparticles in the images were usually below 100 nm. A closer look at the micrographs showed that the polygonal particles had an internal nanostructure (i,j). At first sight, it appeared like a lamellar morphology composed of hydrophobic bright regions and hydrophilic dark regions. The layer periodicity was estimated to approximately 6–7 nm (small white lines). In various simulations [223,224], it has been demonstrated that comb-like polymers with flexible side chains can undergo nanophase separation between the polymer backbone and the side chains. This can be associated with the formation of disordered domains or, if the side chains are sufficiently long and adopt an all-*trans* conformation (e.g. paraffinic chains during crystallization), they form a lamellar morphology. This is particularly favored by flexible polymer backbones [225] and also quite likely for Stearoyl-PGAs. Other polymers showing this behavior are polypeptides [224] or chitosan with *n*-alkyl side chains [226], poly(*n*-alkyl methacrylates) and poly(1-olefins) [227]. However, a closer inspection of PGA-S20 nanoparticles (see inset in Figure 4-4i) indicated that a more complicated morphology could be present here. It has also been reported that certain phase separated block copolymers can form hexagonally packed domains [228] when the volume fractions of the separated blocks favor such packing. As in the case of PGA-S20, the pool of alkyl chains accounts for 24 vol%, it is plausible that the superstructure formed by the nanophase separated domains might be not lamellar but similar to such a hexagonal morphology. In order to further clarify these considerations, X-ray scattering experiments were performed (4.1.8).

For Oleoyl-PGA nanoparticles (Figure 4-4m-p), all detected nanoparticles were spherical in shape, irrespective of their esterification degree. In the freeze-fracture micrographs, a phase separated structure was evidenced which might be an indication for a co-continuous phase morphology as also reported for cubosomes of monoolein (GMO) [54,229]. The possible structure analogy of Oleoyl-PGAs to GMO cubosomes, however, is still under discussion and requires further investigation.

The different shapes and structures of the nanoparticles could influence drug incorporation and *in vivo* behavior. It has been reported [37] that spherical particles move in almost linear flow within capillaries without any lateral drift to the vessel wall. Non-spherical particles, in contrast, can show complex motions, drifting laterally from one side of the vessel wall to the other. With these margination dynamics, non-spherical particles are more likely to extravasate through fenestrations, which is desirable in vascular and tumor targeting. They are also more likely to leave larger vessels in favor of the smaller and thus accumulate within the microcirculation. Moreover, it is known that nanoparticle adsorption to endothelium or mucosa is influenced by geometry as well as their strength of adhesion and internalization into cells [23,96]. In view of this it is crucial to know the particle structure for the rational design of *in vivo* drug carriers.

4.1.5 Asymmetrical flow field-flow fractionation

AF4 combined with MALLS permits accurate size determination of a sample due to separation before the MALLS measurement. AF4/MALLS determines the mass-weighted root mean square radius (r_{rms}) of each eluted fraction [230], also called radius of gyration [231]. The r_{rms} is calculated as the root mean square of the distance of all parts of the object from its center of mass. It is therefore strongly dependent on the particle morphology. Based on that, the combination of AF4 and MALLS is a valuable tool to obtain shape information of particles. PCS, in contrast, works with the assumption of spherical particles and determines their hydrodynamic diameters ($2r_h$). The ratio r_{rms}/r_h of the AF4/MALLS radius and the PCS radius of an eluted sample fraction can therefore be used for shape determination [232,233].

For hard spheres r_h is directly proportional to r_{rms} with [230,234]

$$r_h = r_{rms} \sqrt{\frac{5}{3}}$$

Equation 4-1. Correlation between hydrodynamic radius r_h and root mean square radius r_{rms} .

This leads to an r_{rms}/r_h ratio of 0.775. For non-spherical particles the ratios are higher, increasing up to a value of approximately 2 for rigid rods [231].

In TEM micrographs the third dimension of PGA-S20 nanoparticles could not be detected clearly. For most particles it could not be discriminated if they were flat platelets or bulky stacks (Figure 4-4h-l). Therefore, AF4 measurements were carried out to get additional information about their shape. For comparison, PGA-S85 nanoparticles of spherical shape were also included in this study.

In order to compare AF4 and PCS data of the same particle fractions, eluted samples were collected at the end of the AF4 channel and analyzed by PCS. Figure 4-5 displays $2r_{rms}$, the calculated diameter $2r_h$ for spheres (according to Equation 4-1) and the z-averages of the respective particle fractions measured by PCS. For PGA-S85 (a), the z-averages are in relatively good agreement with the calculated spherical diameters, the r_{rms}/r_h ratio mostly lying between 0.7 and 0.8. This verifies the spherical shape of PGA-

S85 nanoparticles, already seen by TEM (Figure 4-4a,b). For PGA-S20 (b), the measured z-averages of the firstly eluted AF4 fractions are only slightly smaller than the calculated spherical diameters. Ratios between 0.77 and 0.83 indicate shapes close to spheres for the smaller particles (55-100 nm). These fractions could correspond to the cube-like stacks that were detected in TEM in this size range (Figure 4-4i). For the larger particles with z-averages between 110 and 170 nm, the ratio is continually increasing up to 0.99. This points to non-spherical particles with rather flat shapes. In view of these measurements, it can be suggested that the third dimension of PGA-S20 nanoparticles is varying from bulky to more flat with increasing particle size.

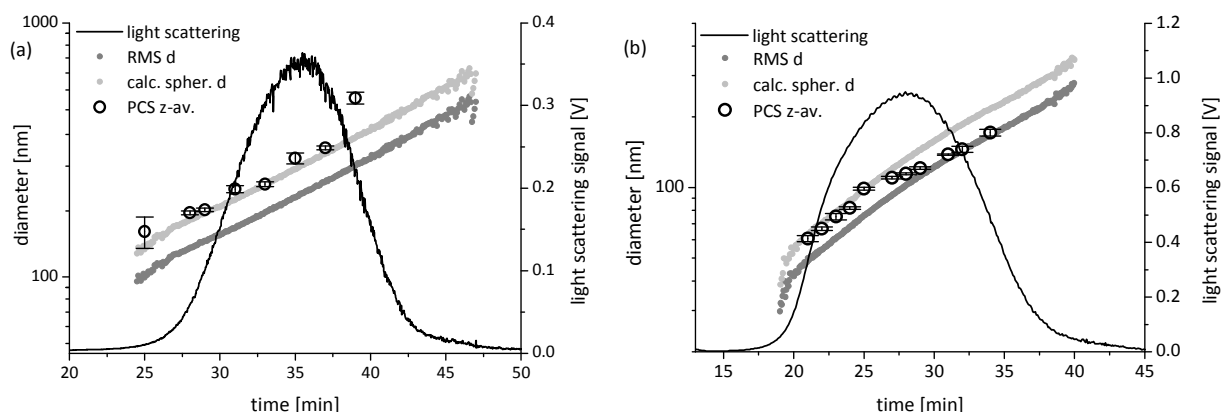


Figure 4-5. AF4 elution profile of (a) PGA-S85 and (b) PGA-S20 nanoparticles, showing the intensity of the light scattering signal at 90° over the time as well as d_{rms} , the calculated spherical diameters and the z-averages determined by PCS.

In addition to these measurements for shape determination, AF4 was used to get a deeper insight into the PGA-S65 nanoparticles coated with UH23. A method suitable for the detection of polymers was applied and – other than for the particles mode – the refractive index (RI) detector signals were used to compare the presence of UH23 in the coated sample with free UH23. Figure 4-6 displays the overlay of the RI chromatograms for the pure polymer solution and the coated particles, both containing the same amount of UH23. The first peak which was present in both chromatograms is known to be an injection peak observed for each measurement. Apart from that, the chromatogram of the UH23 sample shows 3 more or less distinct peaks. The long tailing of the third peak seems to be an overlay of several broader peaks appearing at higher elution times. This indicates the existence of UH23 in several forms and aggregates, probably micelles, which was also reported for similar cholesterol-bearing HPMA copolymers polymers [148,149]. The calculated molecular mass of the aggregates was in the range of $1.4\text{--}3.5 \times 10^7$ Da. Unfortunately, various fit methods of the raw data did not lead to reliable results for corresponding diameters. Results for the average geometrical diameter of the micelles were in the range of 20-45 nm.

The chromatogram of the coated nanoparticles displays the same peak pattern as the UH23 polymer, indicating the presence of unbound polymer molecules in the nanoparticle sample. Given that the content of UH23 was equal in both injected samples,

it is obvious that the main part of the polymer must have been attached to the nanoparticles. Quantitative evaluation of the peaks was, however, not possible as the shoulder of the third peak merges into the elution peak of the nanoparticles. As a result of the method cycle which was adjusted to the separation of small compounds like free polymers and micelles up to an elution time of 30 min, all larger particles were eluted in one peak after 30 min when the cross-flow dropped to almost zero.

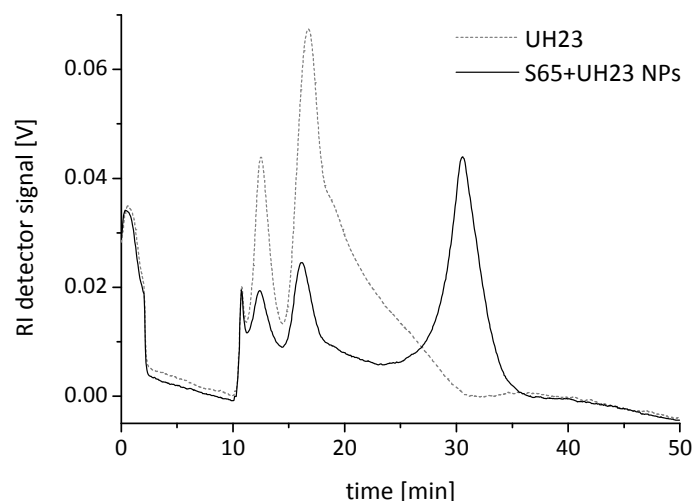


Figure 4-6. AF4 chromatograms of the refractive index detector for PGA-S65 nanoparticles coated with UH23 (solid) and free UH23 copolymer (dashed).

4.1.6 Differential scanning calorimetry

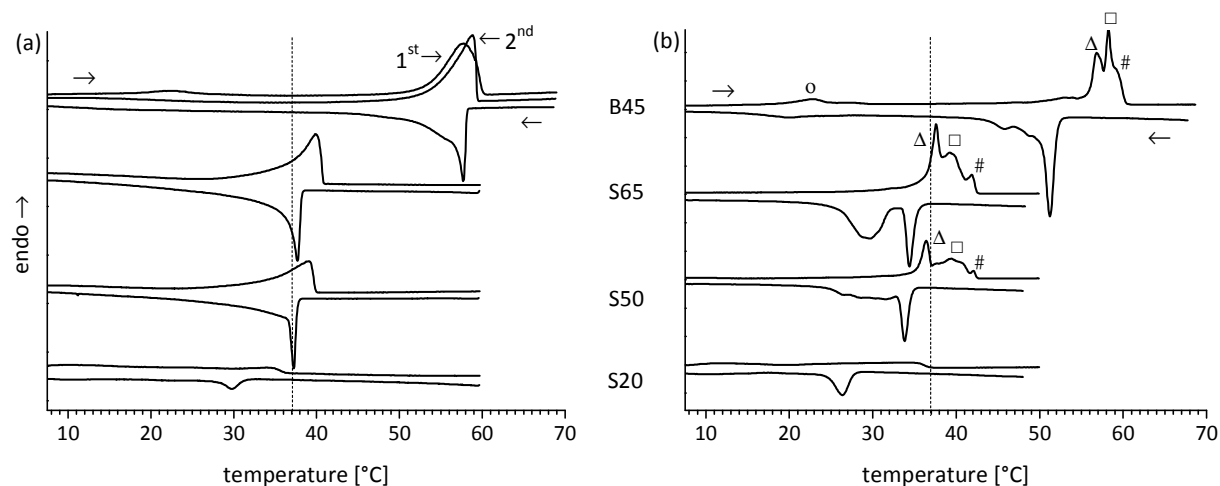


Figure 4-7. DSC thermograms of (a) bulk polymers and (b) nanoparticles: Second heating and cooling curves are shown if not stated otherwise. The dotted line indicates body temperature (37 °C); the symbols (o, Δ, □, #) mark the different transition peaks in the heating curves to simplify the discussion.

DSC measurements of bulk polymers and nanoparticles were carried out to investigate the influence of esterification on the thermal behavior, with particular regard to body temperature (Figure 4-7, Table 4-1). As the PGA backbone is an amorphous polymer, crystallization and melting are related only to the alkyl side chains. The heating

thermograms of PGA-S50, PGA-S65 and PGA-B45 bulk polymers (a) all showed one endothermic peak with a slow rise, corresponding to the melting of the fatty acid chains. The melting event occurs gradually over a temperature range of about 10 °C. Upon cooling, an initially sharp peak indicates an almost collective recrystallization of the fatty acid chains which then, however, fades into a tailing over a range of about 10 °C. The transition maxima (T_h) of Stearoyl-PGA bulk polymers were detected between 39.1 and 39.9 °C. With increasing esterification degree a tendency to higher T_h was observed (Table 4-1). The recrystallization peaks between 37.2 and 37.7 °C show the same trend.

Table 4-1. Temperatures (T) of peak maxima of heating (h) and cooling (c) curves in DSC thermograms for bulk polymers and nanoparticles (NP); main peaks are marked with *. For Behenoyl- and Stearoyl-PGA bulk polymers, enthalpies (ΔH) were calculated for heating and cooling.

	T_h [°C]	ΔH_h [J/g]	T_c [°C]	ΔH_c [J/g]
B45	58.8	62.9	57.7	-61.3
Behenic acid	80.1		76.1	
S65	39.9	62.7	37.7	-74.4
S50	39.1	48.1	37.2	-49.2
S20	34.4	4.3	29.7	-4.9
Stearic acid	69.7		66.6	
L30	-37		--	
L50	-22		-25	
L75	-20.6		-32	
Lauric acid	45.3		-41	
B45-NP	56.8 58.3*		51.2* 45.8	
S65-NP	37.6* 39.2 41.9		34.4* 29.6	
S50-NP	36.4* 39.4 42.1		33.8	
S20-NP	35.2		26.4	

The slight shift to lower temperatures between melting and recrystallization temperature is comparable to triglycerides like glycerol tripalmitate or tristearate [235]. The viscous PGA-S20 doesn't show a distinct melting peak. Nevertheless, the step in the heating curve indicates a phase transition at about 34.4 °C which shifts to 29.7 °C during cooling. All given thermograms do not differ significantly between the three consecutive heating and cooling scans. Only PGA-B45 shows an additional shallow peak in the first heating scan at 22.6 °C. This could be attributed to a transition in the polymer backbone which, however, could not be detected for the other polymers. Melting and crystallization of Lauroyl-PGAs, which are viscous at room temperature, takes place at temperatures far below zero (Table 4-1) and no recrystallization peak could be observed for PGA-L30. T_h and T_c again increased for higher amounts of fatty acid side chains. For Oleoyl-PGAs no DSC peaks could be measured in the range of -50 to 80 °C. Although the neat oleic acid has a melting temperature of 17°C, none of the Oleoyl-PGAs

has shown any indication of a crystalline fraction. This indicates that these polymers seem to be completely amorphous.

Overall, the results of the bulk polymers display an increase of T_h and T_c with increasing esterification degree and increasing length of alkyl side chains. Both observations can be attributed to a more compact packing mode of the polymer leading to a higher order which increases the energy required for melting [236]. Side chain crystallization depends on a certain length of the alkyl chains, usually > 12 carbon atoms [236]. Nevertheless, melting and crystallization was observed for Lauroyl-PGAs in this study, even though at very low temperatures. This might be owing to the flexible PGA backbone which facilitates the adoption of a close side chain packing [236].

DSC heating curves of PGA-S50, PGA-S65 and PGA-B45 nanoparticles (Figure 4-7b) are characterized by three consecutive peaks (Δ , \square , $\#$). Such a sequence of transition peaks is likely to correspond to the melting of particle fractions differing in size and shape [69]. This theory was already demonstrated for SLNs [237] where the successive melting of SLNs with different thickness was shown. For PGA based nanoparticles, the melting temperature of the first occurring peak (Δ) was about 2–3 °C lower than the maximum of the respective bulk polymer. This maximum was almost identical with the second occurring peak (\square) in the nanoparticle thermogram. Surprisingly, the melting curves of PGA-S50 and PGA-S65 particles showed a small third peak ($\#$) at higher temperatures than the bulk polymers. Commonly, decreased melting points are observed for colloidal systems which are assigned to the large surface-to-volume ratio [77]. For *in vivo* application it is crucial to know if body temperature influences the drug carrier system. During heating, at 37 °C part of the PGA-S50 and also some PGA-S65 nanoparticles were already molten. This might influence targeting, fate and drug release *in vivo*. Therefore Behenoyl-PGA nanoparticles have been developed which are solid up to over 50 °C. As for PGA-B45 bulk polymer, the additional shallow first transition could also be detected for the nanoparticles (\circ) at the same temperature. For the particles, however, this transition occurred not only during the first heating scan but also in the following and was moreover discovered in the cooling curves.

Recrystallization of the nanoparticles took place in two steps with a first sharp peak followed or overlapped by a broader second one. Compared to the first melting peak (Δ), the sharp crystallization peak was shifted 2.6–3.2 °C for the Stearoyl-PGAs and 5.6 °C for PGA-B45 towards lower temperatures. In comparison to the last melting event ($\#$) the shifts accounted for 7.1–8.3 °C. The thermogram of PGA-S20 nanoparticles was almost identical to that of the bulk polymer but also with a greater peak shift in the cooling curve. The step in the heating curve indicates the existence of non-crystalline PGA-S20 nanoparticles that undergo phase transition at about 35 °C.

The supercooling for all examined nanoparticles was considerably lower compared to SLN dispersions [235]. The phenomenon of supercooling is a problem for the production of SLN with triglycerides such as glycerol trilaurate and trimyrystate. These SLN are completely or partly in the supercooled state at room temperature and therefore

metastable. In contrast to that, recrystallization for PGA based nanoparticles was completed at about 25 °C or higher.

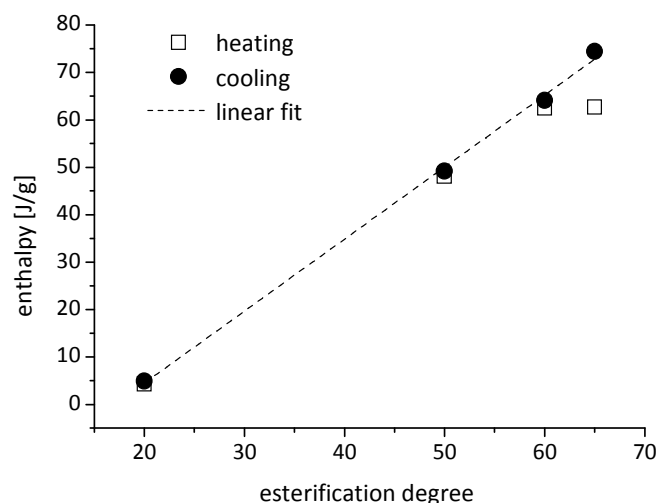


Figure 4-8. Heating and cooling enthalpies of Stearoyl-PGAs measured by DSC (correlation of cooling enthalpies: $R^2=0.999$).

Transition enthalpies were calculated for some bulk polymers (Table 4-1). Heating and cooling enthalpies for the respective polymers were similar except for PGA-S65. The plot of the cooling enthalpies versus the esterification degree of the polymers shows a linear dependency with a good correlation (correlation coefficient $R^2=0.999$) (Figure 4-8). This indicates a linearly increasing crystallinity with the degree of esterification, confirming that crystallization is only referring to the alkyl side chains.

The degree of crystallinity can considerably influence drug incorporation and release rates [67]. In general, non-crystalline systems have a higher capability to incorporate other molecules whereas crystallization often leads to expulsion. PGA based nanoparticles with lower esterification degrees as well as Lauroyl- and Oleoyl-PGA nanoparticles might therefore be promising carriers for high drug loads. As Lauroyl- and Oleoyl-PGA nanoparticles did not show any transition peaks or steps above 10 °C, they can be regarded as highly viscous nanoemulsions rather than solid particles. This assumption was verified by $^1\text{H-NMR}$ spectroscopy measurements (4.1.7).

4.1.7 $^1\text{H-Nuclear magnetic resonance spectroscopy of nanoparticles}$

$^1\text{H-NMR}$ spectroscopy measurements were carried out to get more information about the aggregate state of the nanoparticles at room and body temperature as well as their structure and surface properties.

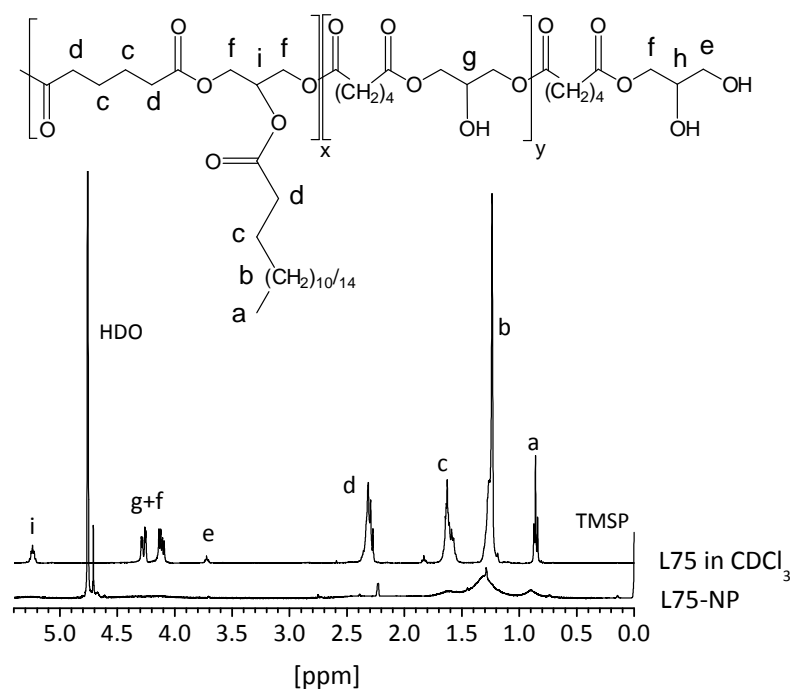


Figure 4-9. ¹H-NMR spectra of PGA-L75 bulk polymer (dissolved in CDCl₃) and nanoparticles (NP; in H₂O/D₂O) at room temperature (TMSP: 3-(trimethylsilyl)propionic-2,2,3,3-*d*₄ acid as a standard). The signals are signed corresponding to the positions of the protons in the chemical formula above.

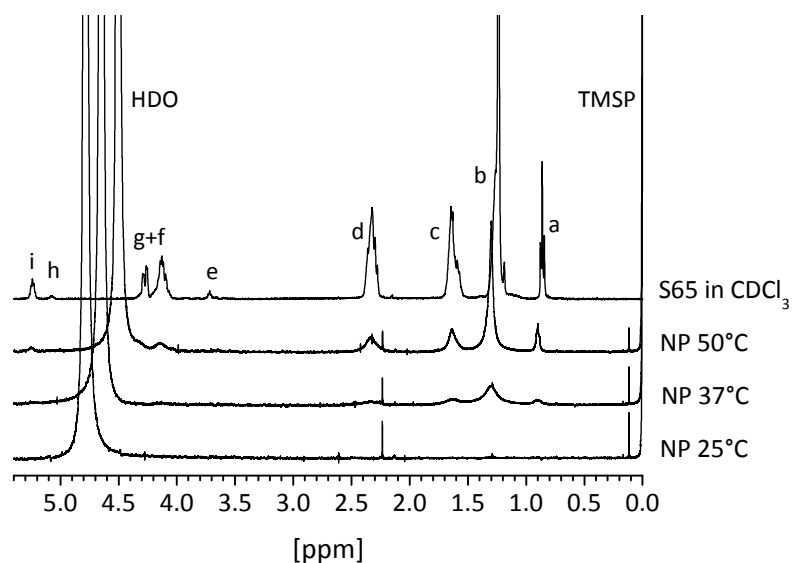


Figure 4-10. ¹H-NMR spectra of PGA-S65 bulk polymer (dissolved in CDCl₃) and nanoparticles (NP; in H₂O/D₂O) at room temperature (TMSP: 3-(trimethylsilyl)propionic-2,2,3,3-*d*₄ acid as a standard). The signals are signed corresponding to the positions of the protons in the chemical formula of Figure 4-9.

For PGA-L75 nanoparticles (Figure 4-9) at room temperature only peaks a and b are detectable clearly albeit very broad and shallow. Peak a, observed at 0.88 ppm and peak b at 1.25 ppm are the characteristic peaks for the terminal CH₃ group and the CH₂ groups of aliphatic chains and fatty acids. This confirms that the fatty acid chains of PGA-L75 are not crystalline at room temperature but highly viscous, just as it is the corresponding bulk polymer. The small sharp peak at about 2.2 ppm probably

corresponds to a marginal amount of acetone remaining from the preparation procedure of the nanoparticles. Other peaks of the bulk spectrum are not visible for the nanoparticles. Peaks e–i, corresponding to the hydrophilic polymer backbone, could not be detected for the nanoparticles. This indicates that the backbone parts are not flexible but rigidly integrated in the particle structure. The architecture of PGA based nanoparticles therefore has to be distinguished from the structure of the well-known PEG-PLGA. This polymer forms particles of the core–corona type with flexible PEG chains extending out into the aqueous environment [238].

For PGA-S65 nanoparticles, temperature dependent measurements were performed in order to study aggregate state and viscosity of the particles with increasing temperature (Figure 4-10). The chemical shift for HDO is temperature dependent and was detected in good agreement with literature data (± 0.01 ppm) [239]. At 25 °C no other peaks could be observed, indicating solid particles without any flexible parts. The sharp peak at about 2.2 ppm is again corresponding to acetone residues. At 37 °C some broad peaks (a–d) are visible with small amplitudes. The broad peaks originate from highly viscous chains with moderate mobility, pointing to the beginning of the melting event. This finding is in good agreement with DSC data (Figure 4-7) which shows the melting onset at about 35 °C. At 50 °C all peaks of the bulk spectrum are also visible for the nanoparticles. Peak amplitudes are increased compared to 37 °C but peaks e–i appear only very weak. These results demonstrate the melting of the fatty acid side chains and the increasing flexibility during heating.

4.1.8 X-ray diffraction

As indicated in TEM micrographs, PGA based nanoparticles reveal different architectures, probably driven by nanophase separation due to the immiscibility of backbone and side chain material. To obtain more detailed information about the inner structure of the nanoparticles and to investigate the influence of side chain type and esterification degree, XRD measurements have been performed on the dispersions.

Ordering phenomena in the investigated systems occur at two different length scales (Figure 4-11). In the SAXS range the supramolecular nanostructure can be detected, i.e. the arrangement of the side chain phase and the amorphous phase formed by the PGA backbones – as also directly observed by TEM. In WAXS, characteristic X-ray scattering peaks yield information on the molecular arrangement of the fatty acid chains and the resulting subcell structure.

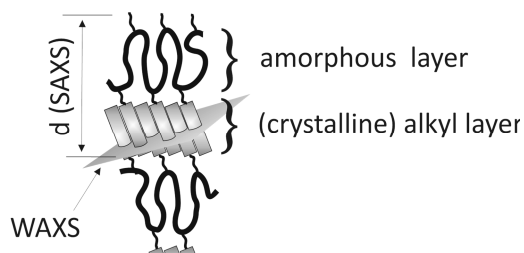


Figure 4-11. Structural model of nanophase separated PGA fatty acid esters and the accessibility of the structural domains by XRD. WAXS reports about the arrangement of the side chains whereas SAXS yields information about the superstructure and the characteristic long spacing d of one repeating unit.

To get an overview of the X-ray scattering reflections, at first, PGA-S20 and PGA-S85 were investigated in bulk by simultaneous temperature controlled SAXS and WAXS measurements. Figure 4-12a shows the combined SAXS/WAXS trace for PGA-S85 during a heating and cooling cycle. Starting at 17.5 °C, the first order small-angle peak appears at a scattering vector of $q^* = 1.65 \text{ nm}^{-1}$ ($q = 4\pi\sin\theta/\lambda$, with λ being the wavelength of the Cu K_{α} radiation and 2θ the scattering angle) together with three small peaks representing the next higher order reflections. As the higher order reflections appear in equidistant positions of $2q^*$, $3q^*$ and $4q^*$, a lamellar supramolecular structure is evidenced. Figure 4-11 shows a schematic model, based on the idea that alkyl side groups belonging to different backbone molecules form layer-like crystalline nanodomains which are separated by backbone chains. According to Bragg's law, the position of the first maximum q^* can be related to the domain spacing $d = 2\pi/q^*$, which is in this case representing the average distance of the lamellae $d = 3.81 \text{ nm}$. From the relative intensity of the higher order peaks a volume fraction of the crystalline polymer part can be estimated according to

$$\frac{\int_0^{\infty} I_1(n) ds}{\int_0^{\infty} I_1(1) ds} = \frac{\sin^2(\pi\phi n)}{\sin^2(\pi\phi) \cdot n^2} \quad [240].$$

Equation 4-2. Estimation of the crystalline volume fraction from the ratio of the integrated intensities of the higher order peaks $I_1(n)$ to the integrated intensity of the first order peak $I_1(1)$ according to [240].

Applying a fit function to the obtained SAXS peaks, a crystalline volume fraction of 0.58 was obtained. This is in good agreement with the calculated volume fraction of the side chains (0.57), indicating a strong separation of the two phases. On this basis, the crystalline layer thickness was calculated as 2.2 nm, which is slightly thinner than the stearyl side-chain length of $\approx 2.4 \text{ nm}$. This supported the assumption of interdigitated side chains and indicated a side chain tilt angle of $\approx 20^\circ$.

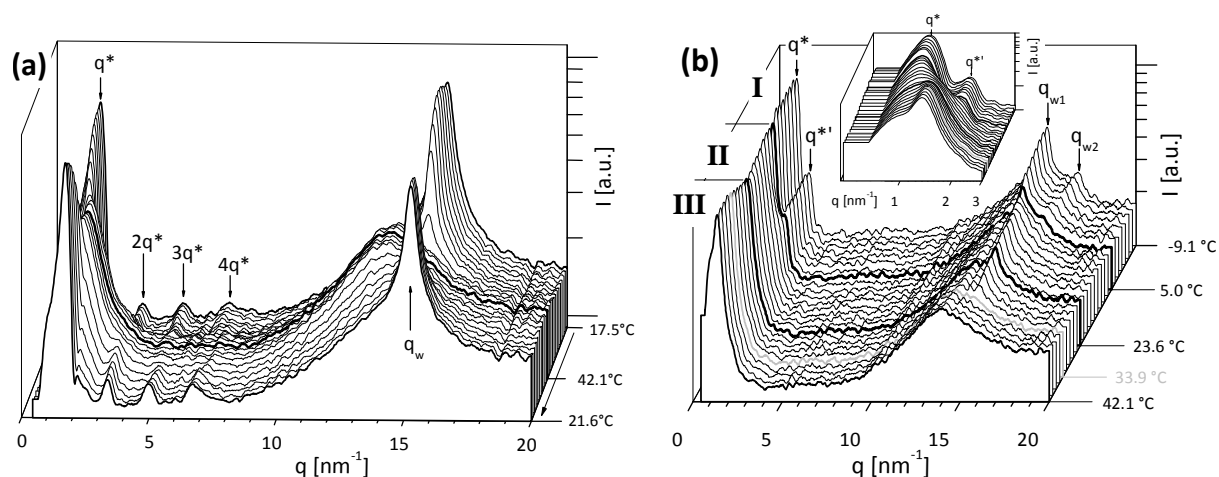


Figure 4-12. (a) Combined SAXS and WAXS traces of PGA-S85 during a heating and cooling cycle (2.05 K steps from 17.5 to 42.1 °C and back to 21.6 °C, each point 5 min equilibration and 10 min data acquisition). (b) Combined SAXS and WAXS traces of PGA-S20 during a heating run (2.05 K steps from -9.3 to 42.1 °C, each point 5 min equilibration and 10 min data acquisition). The inset is a close-up of the SAXS region in a logarithmic scale. (slightly modified from Weiss et al., *Macromol. Rapid Commun.*, 33 (2012) 35-40)

In the wide-angle regime, a single reflex appears at $q_w = 15.30 \text{ nm}^{-1}$ corresponding to the (110) direction of a hexagonal packing of the side chains with a lattice parameter $a = 0.474 \text{ nm}$. This can be assigned to the hexagonal rotator phase R II of alkanes [241-243], which typically occurs in the case of *n*-alkyl-substituted comb-like polymers [244,245].

During heating, the SAXS traces do not show significant changes until the beginning of melting at about 28 °C, whereas the WAXS peak q_w is shifted slightly to 15.21 nm^{-1} . During melting, the peak in the WAXS range disappears into an amorphous halo which shifts to smaller q -values due to thermal expansion. At the same time, the main SAXS peak becomes broader and shifts to higher q^* -values (1.98 nm^{-1}) and the higher order reflections virtually disappear. This means that the lamellar phase becomes more disordered and the characteristic length scale of the supramolecular arrangement in the melt is reduced to $\approx 3.2 \text{ nm}$. This can be attributed to the higher flexibility of the polymer, especially of the backbone chain, in the melt. It should be noted that in both SAXS and WAXS, there were still – albeit broad – reflections visible at 42 °C, indicating a pre-structured melt with a preferential ordering among the nanophases [206,245].

For PGA-S20, the measurement was started at -9.1 °C where in the small-angle range two peaks at $q^* = 0.94 \text{ nm}^{-1}$ and $q^{*'} = 1.62 \text{ nm}^{-1}$ were observed (Figure 4-12b, region I), showing a ratio of approximately $1:\sqrt{3}$. This indicates a (pseudo-)hexagonal superstructure. In the wide-angle region, also two peaks were observed ($q_{w1} = 15.01 \text{ nm}^{-1}$ and $q_{w2} = 16.80 \text{ nm}^{-1}$), which can be identified as the (110) and (020) directions of an orthorhombic rotator phase R I of the alkyl side chains [241-243,246] with lattice parameters $a = 0.505 \text{ nm}$ and $b = 0.748 \text{ nm}$. During the heating process above $\approx 5 \text{ °C}$ (region II), the R I rotator phase transforms into the R II rotator phase, indicated by a single peak at $q_w = 15.21 \text{ nm}^{-1}$ ($T = 11.3 \text{ °C}$) in the WAXS range. Thus, in

this temperature range, the same hexagonal packing of the stearyl side chains can be observed for PGA-S20 and PGA-S85. The occurrence of rotator phases and its transitions in the case of medium length alkanes, fatty acids, and lipids has been discussed extensively in literature [241,242].

With further increase in temperature, the first SAXS peak shifts to $q^* = 1.18 \text{ nm}^{-1}$ and merges with the $\sqrt{3}$ peak (q^*) into a single broad peak. This can be assigned to a reorientation of the stearyl phase in the PGA matrix. The WAXS peak q_w is also slightly shifted to 15.22 nm^{-1} ($T = 23.6 \text{ }^\circ\text{C}$). During melting, above $24 \text{ }^\circ\text{C}$ (region III), the SAXS peak shifts further to $q^* = 1.32 \text{ nm}^{-1}$ and the wide angle reflex vanishes. At about $34 \text{ }^\circ\text{C}$ (middle part of region III) only an amorphous halo remains in the wide-angle regime indicating complete melting.

The internal morphology of the nanoparticles formed by PGA-S85 and PGA-S20 is summarized in Figure 4-13. The lamellar supramolecular arrangement of PGA-S85 leads to spherical nanoparticles with an onion-like morphology (Figure 4-13a, left). The detailed lamellar structure of the alternating crystalline and amorphous phases with the dimensions obtained from SAXS measurements is represented in the middle part of Figure 4-13a. The crystallographic packing of the n -alkyl side chains in the hexagonal rotator phase R II is shown on the right. As illustrated, rotator phases are characterized by rotational disorder about the long axes of the alkyl chains [247], resulting in a scattering of the axial orientations.

For PGA-S20, nanodomains are assumed to be arranged in a board-like pattern (Figure 4-13a, left). The pseudo-hexagonal arrangement of the phase separated domains of side chains and polymer backbone (Figure 4-13b, middle) is finally the reason for the nanoparticle formation with polygonal shapes and apparent lamellar arrangement (Figure 4-13b, left) as observed in TEM images (Figure 4-4i). The packing of the side chains at low temperatures, corresponding to an orthorhombic rotator phase R I, is shown on the right [248].

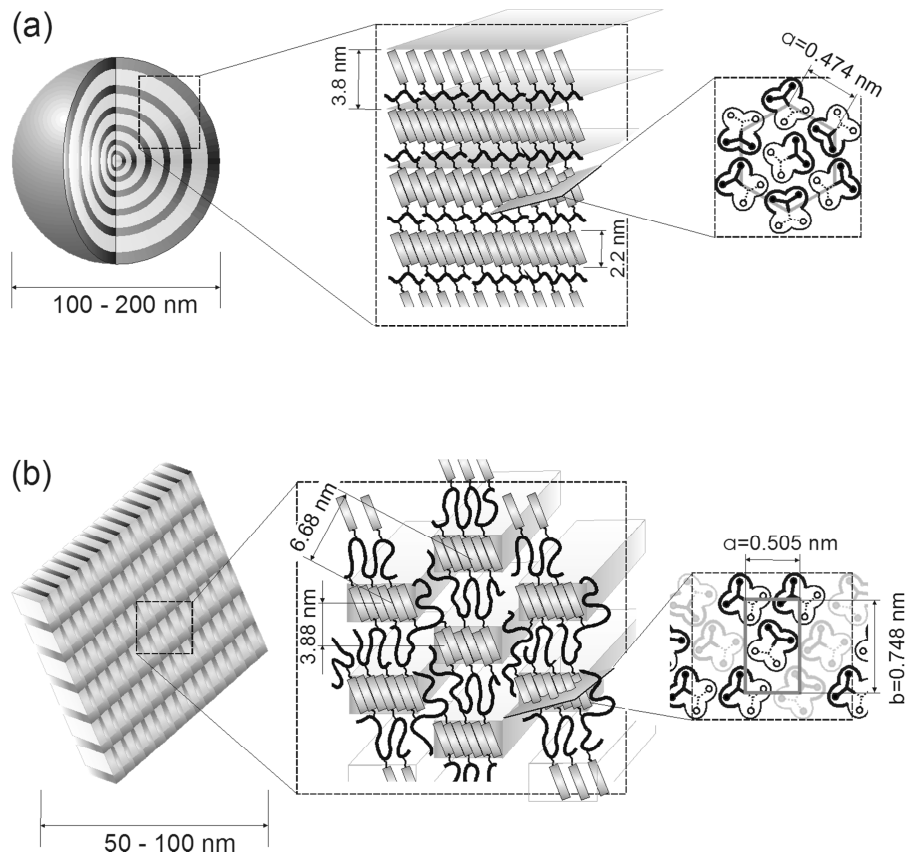


Figure 4-13. Schematic illustration of the hierarchical structures proposed for (a) PGA-S85 and (b) PGA-S20. The morphology of the nanoparticles, the arrangement of the nanodomains and the packing of the stearoyl side chains in a plane normal to their axis are depicted from left to right. (taken from Weiss et al., (2012), *Macromol. Rapid Commun.*, 33:35-40, with permission from E. Amado).

To further elucidate the peaks in the small angle range and to also include the other polymers as well as their nanoparticles in the study, detailed SAXS measurements were performed using a rotating anode.

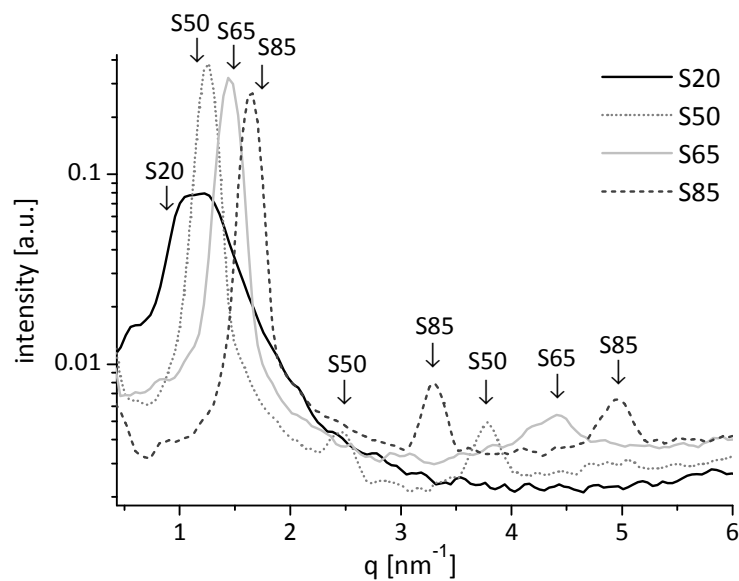


Figure 4-14. SAXS profiles of Stearoyl-PGA bulk polymers.

The position q^* of the first maximum in the SAXS profiles of bulk polymers (Figure 4-14) and nanoparticles (not shown due to a poor signal-to-noise ratio) shifts to higher q values with increasing esterification degree of PGA (Figure 4-14). This reflects a decrease in the long spacing with increasing amount of fatty acid side chains. This can be explained as follows based on the structural model of these polymers (Figure 4-13). The long spacing reflects the average thickness of one repeating unit in the polymer which is the sum of the crystalline side chain layer and the amorphous backbone layer. With increasing degree of esterification the average distance between the ester bonds in the PGA backbone is decreasing, leading to a more condensed packing and thus to a reduction in the amorphous layer thickness. At the same time, the thickness of the crystalline layer remains constant since it is determined by the stearyl chain length.

The peak of PGA-S20 is considerably broadened which possibly might be attributed to the different inner structure and the limited size of the crystal-like structures in this polymer [206]. No peaks of higher order could be resolved for PGA-S20 bulk and nanoparticles. In contrast, the SAXS traces of PGA-S50, -S65 and -S85 reveal several higher order peaks. As already seen in the combined SAXS/WAXS trace, for PGA-S85 equidistant peaks indicate a highly ordered lamellar superstructure. The same is visible for PGA-S50. At first sight, it was surprising that PGA-S65 only shows one peak of higher order at $3q^*$ but the peak at $2q^*$ is missing. Nevertheless, this is not pointing to a different nanostructure in this polymer but can be explained in a short excursus:

The intensities of the Bragg peaks in a diffraction pattern are not equal as the amplitudes are determined by the scattering function of the sample. Derived from Porod's scattering function of lamella [249], the ratio of the integrated intensity of the n^{th} order peaks $I_1(n)$ to the first order peak $I_1(1)$ in an ideal periodic lamellar lattice of the crystallinity ϕ is given by Equation 4-2:

$$\frac{\int_0^\infty I_1(n) ds}{\int_0^\infty I_1(1) ds} = \frac{\sin^2(\pi\phi n)}{\sin^2(\pi\phi) * n^2} \quad [240].$$

When this ratio is plotted against the crystallinity ϕ , the function yields zero for distinct values of ϕ with

$\sin^2(\pi\phi n) = 0$. This applies for $\pi\phi n$ as an integer multiple of π :

$$\pi\phi n = N\pi$$

$$\phi n = N$$

$$\phi = \frac{N}{n} \quad \text{with } N, n \in \mathbb{N} \quad \text{and } \phi < 1.$$

As an example, the intensity of the 2nd order peak ($n = 2$) approaches 0 for $\phi = \frac{1}{2}$, the 3rd order for $\phi = \frac{1}{3}$ and $\frac{2}{3}$, etc.

In the case of PGA-S65, the volume fraction of the stearyl side chains was calculated as 51 %, which complies approximately with the above described situation of $\phi = 50$ % where the second order peak disappears. Overall, a lamellar superstructure of PGA-S50, PGA-S65 and PGA-S85 bulk polymers can be concluded from the SAXS measurements. Apart from the poor signal-to-noise ratio, the same was indicated for the nanoparticles.

In order to verify this and to get deeper insight into the nanoparticle samples of PGA-S20 and Oleoyl-PGA, simultaneous temperature controlled SAXS/WAXS experiments were carried out using synchrotron radiation.

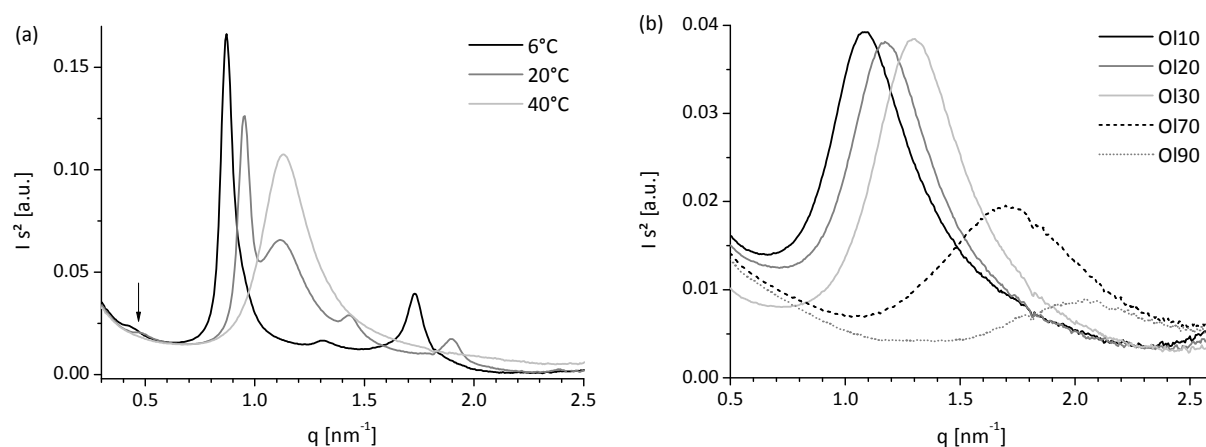


Figure 4-15. a) SAXS profiles of PGA-S20 nanoparticles at 6°C, 20 °C and 40 °C. The small prepeak is indicated by an arrow. b) SAXS profiles of Oleoyl-PGA nanoparticles at 20 °C.

The highly resolved SAXS profiles of the synchrotron experiments reveal that several peaks are present for PGA-S20 (Figure 4-15a) in the range of $q = 0.8$ - 2.5 where in the SAXS profile of the rotating anode only one broad peak has been visible (Figure 4-14). The appearance of the main peaks is similar to the above described SAXS/WAXS trace (Figure 4-12b), shifting to higher q values with increasing temperature. However, additional peaks are detected here, indicating a more complex superstructure. The ratio of the main peak ($q^* = 0.87$ or 0.95 nm^{-1} for 6 or 20 °C) and the peak at 1.73 or 1.90 nm^{-1} is 2, reflecting a lamellar structure. The small prepeak (marked by an arrow), visible at approximately $0.5q^*$, the peak at $1.5q^*$ and the very small reflection at $2.5q^*$ (only visible at 20 °C) point to the existence of another long period, possibly with double spacing. Whereas these peaks are all decreasing and shifting to higher q values with increasing temperature, the position of the emerging peak at 1.12 nm^{-1} does not change in the range of 20 to 40 °C. This refers to an initial contraction of the long period and a subsequent complete reorientation of the polymer chains at higher temperatures. The relatively broad reflection at 40 °C indicates that nanophase separation is still present and the domains keep a preferred orientation even in the melt.

For PGA-S20 in bulk, a similar pattern was recorded but with a slight shift to higher q values. This points to shorter spacings in the bulk compared to the nanoparticles. For the solid Stearoyl-PGAs, in contrast, spacings for bulk and nanoparticles were about equal and no additional peaks were detected compared to the results of the rotating anode.

In the synchrotron, also the viscous Oleoyl-PGA nanoparticles have been investigated. WAXS experiments revealed only an amorphous halo and no crystalline peaks have been observed for all Oleoyl-PGA samples (not shown). This confirms the results of the DSC measurements (4.1.6). Nevertheless, in SAXS (Figure 4-15b) a distinct scattering peak

was observed, indicating phase separation. During heating from 20 °C to 60 °C no considerable change of q^* could be observed. As this behavior and also the position of the PGA-OI20 peak is similar to the high temperature peak of PGA-S20 ($q = 1.12 \text{ nm}^{-1}$), the same superstructure can be assumed for the Oleoyl-PGAs and PGA-S20 at high temperatures. As no higher order peaks could be detected for the Oleoyl-PGAs – owing to the limited q range of the measurement setting – no identification of the phase morphology was possible.

The relating long spacings d , calculated from the positions of the main peak q^* , are depicted in Figure 4-16. For Oleoyl-PGA nanoparticles, this length depends nearly linearly on the oleoyl volume fraction, indicated by the dotted fit line. The solid Stearoyl-PGA particles show a similar behavior but with a longer domain spacing. This is most likely resulting from the different packing mode of the saturated and unsaturated fatty acid side chains as well as the higher rigidity in the solid polymer. The value for the highly viscous PGA-S20 is therefore deviating less from the Oleoyl-PGA data. Above the melting temperature of the stearoyl side chains, all spacings move closer to the Oleoyl-PGA fit line which confirms the influence of polymer flexibility on the domain spacing.

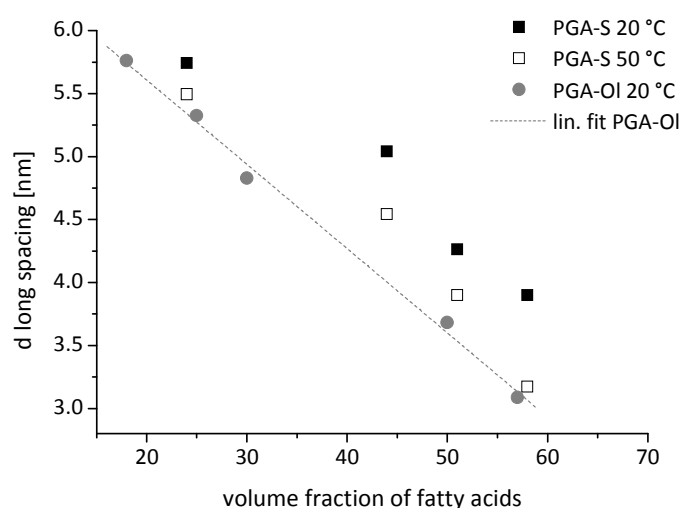


Figure 4-16. The domain spacing d as a function of side chain volume fraction is depicted for Oleoyl- and Stearoyl-PGA nanoparticles. For Stearoyl-PGA spacings above the stearoyl melting temperature have been added (open circles).

4.1.9 Multispectral fluorescence imaging of Nile red loaded particles

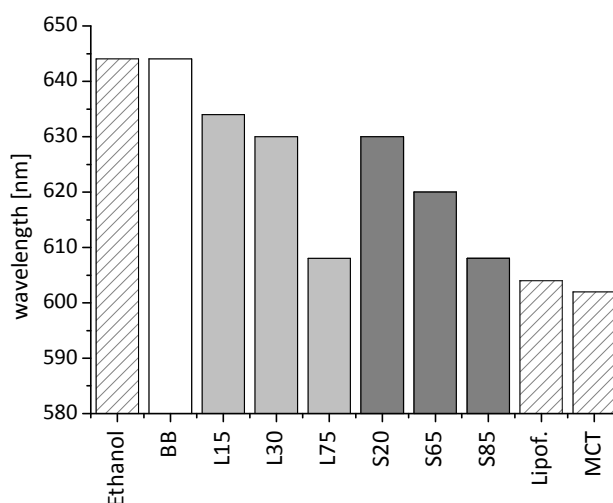


Figure 4-17. Spectral emission maxima of Nile red fluorescence in PGA based nanoparticles and reference substances (Lipof.: Lipofundin® N, MCT: medium chain triglycerides).

Different PGA based nanoparticles were loaded with the solvatochromic dye Nile red in order to investigate the environment inside the particles. Due to the lipophilicity of this dye [97], Nile red molecules are most likely to be incorporated in the fatty acid modified PGA nanoparticles during preparation. It is, however, known that Nile red can also diffuse into water to a very small extent. Nevertheless it can be expected that only the spectra of molecules which are incorporated or attached to the particles are detected by MSFI since Nile red fluorescence intensity in water is almost fully quenched [98].

In general, the excitation and emission maxima of the solvatochromic dye can shift over a span of 100 nm and both spectra move to shorter wavelengths with decreasing polarity of the environment. In Figure 4-17, it is visible that the fluorescence emission maxima of Nile red shift to shorter wavelengths with increasing esterification degree of PGA. This demonstrates an increasing lipophilicity, resulting in similar values as those obtained from the parenteral fat emulsion Lipofundin® N and neat medium chain triglycerides, serving as references.

Comparing the viscous backbone and the three Lauroyl-PGAs, it seems to be an almost linear relationship ($R^2=0.996$, fit not shown) between esterification degree and polarity, indicated by the Nile red wavelength. The emission maximum of the viscous PGA-S20, in comparison, lies a little below this fit line. This is an indication of the higher lipophilicity of Stearoyl-PGA polymers due to the longer fatty acid chains. However, the solid PGA-S65 and PGA-S85 have comparatively higher wavelength maxima. This shift of Nile red fluorescence between viscous and solid particles can be ascribed to the different aggregate states of its environment. Crystallization of the fatty acid chains might lead to partial expulsion of the dye from the lipid matrix into more polar environment. This has also been shown for SLN, where solidification of the triglycerides strongly influenced the fluorescence of Nile red [80]. Due to the range of polarities of the investigated PGA

polyesters, they are promising carriers for a variety of different drugs. PGA with high esterification degrees and long fatty acid chains provide the potential for incorporating highly lipophilic drugs while polymers with lower esterification degrees or shorter fatty acid chain lengths might be promising systems for the incorporation of amphiphilic or slightly lipophilic molecules. For the solid particles, however, a lower loading capacity might be expected than for the liquid or liquid crystalline ones.

4.1.10 Determination of drug loading

The experiment was planned in order to compare the loading capacity of different PGA based nanoparticles, especially the solid particles with the viscous ones. After preparation, the viscous particles macroscopically showed good incorporation efficiencies. No remaining free drug or dye was visible in the water or on the glass wall. However, during the separation step in the PD-10 column, the viscous particles stuck to the column material and were only eluted marginally. The same problem occurred when applying dialysis as separation method where the viscous particles were adhering to the membrane.

In view of this, the study was focused only on the loading of solid PGA-S65 nanoparticles. Fluorescent substances were selected in order to establish the method, determine the elution volume of particles and remaining small molecules and ensure highly sensitive detection.

The first experiments were performed with the highly lipophilic fluorescent dye DiI. During the preparation of PGA-S65 nanoparticles loaded with either 0.25 wt% or 1 wt% of DiI, no free drug was obvious in the water or on the glass walls. After gel filtration about 95 % of the dye could be detected in the nanoparticle fraction calculated in relation to the non-separated references (Table 4-2). This points to a high loading efficiency. After application of 2 wt% DiI in the preparation process, a pink ring was visible on the glass wall after nanoprecipitation, indicating excess dye and an overloading of the particles.

As a lipophilic model drug, the porphyrin derivate THPP was applied. The substance was easily detectable by measurement of its fluorescence intensity. The absorption of THPP in the UV/VIS measurement was determined with a maximum at 421 nm which was in good accordance with literature [208,209]. The calibration of fluorescence vs. concentration ensured linearity in the concentration range of 2 µg/ml up to 75 µg/ml (data not shown). To stay in this linear range, the acetone volume for solution of the drug after lyophilization was increased to 2 ml instead of 1 ml for the highest applied concentration of 10 wt% THPP.

Table 4-2. Recovery rate of DiI and THPP after SEC ($n \geq 3$).

Applied dye/drug [wt% / polymer]	Effectively loaded dye/drug [% of applied dye/drug]	Range [%]
DiI	0.25	94.3
	1	95.4
	2	free dye visible
THPP	1	94.4
	5	100.6
	10	97.9
	15	free drug visible

During the preparation of PGA-S65 nanoparticles loaded with 1, 5 and 10 wt% of THPP, macroscopically no free drug was visible. The particles showed a narrow size distribution ($PDI < 0.09$) and with 140-160 nm, their size was in the same range as for unloaded particles. The recovery rates of the drug in the nanoparticle fraction after SEC are shown in Table 4-2. For all concentrations up to 10 wt% of applied drug almost 100 % could be found after gel filtration. By adding more than 10 wt% of THPP to the polymer, a slight violet ring was visible on the glass wall after nanoprecipitation, indicating an overloading of the particles.

The interpretation of this data is yet ambiguous. The results indicate high loading efficiencies of 94-100 % in the nanoparticles up to 1 wt% of applied DiI and 10 wt% of THPP. This is, however, no clear proof that the small molecules are actually incorporated *in* the nanoparticles. In fact, the molecules could also be adsorbed to the surface of the particles and due to the highly hydrophobic nature and the practical insolubility of DiI and THPP in water don't detach during SEC to a relevant extent. Thus, this experiment doesn't necessarily show the efficiency of incorporation but at least the efficiency of drug loading in or on PGA-S65 nanoparticles.

4.1.11 Hemolytic activity

Hemolytic activity was determined by incubating freshly separated RBCs with 1 % (10 mg/ml) or 0.1 % (1 mg/ml) of nanoparticle suspension for 1 h at 37 °C. Hemolysis was assessed in reference to 2 % aqueous sodium dodecyl sulfate (SDS) solution as 100 % value (positive control); the value of PBS was set as zero (negative control). The nanoparticles of PGA-BB, PGA-S50 and PGA-S65 showed only marginal hemolytic values in the highest applied concentration of 10 mg/ml (Table 4-3). In contrast, for nanoparticles of PGA-S20, hemolysis of approximately 28 % was observed in this concentration. The hemolytic effect might be ascribed to the different hydrophilic-lipophilic ratio of this polymer with only 20 mol% converted hydroxyl groups, leading to pronounced amphiphilic properties. The effect is, however, concentration dependent, as for 1 mg/ml nanoparticles the value dropped to about 1 %. The hemolytic activity of PGA-S20 nanoparticles could also be decreased by adding Poloxamer 188 to the polymer

during the preparation process (1:1). Poloxamer 188 is a triblock copolymer composed of a central hydrophobic chain of polyoxypropylene (POP) flanked by two hydrophilic chains of polyoxyethylene (POE). During the nanoprecipitation process, it is likely that the hydrophobic POP blocks become incorporated in the particles while the hydrophilic POE blocks extend into the water phase, forming a corona-like structure [250]. Because of their hydrophilicity and steric repulsion, these POE chains appear to prevent the interaction of the PGA-S20 particles with the RBCs and thus reduce hemolytic activity [131,251]. With this, hemolysis of the 1 % suspension was only 6 % compared to 28 % without Poloxamer. For the 0.1 % suspensions the hemolytic effect dropped to 1 % for both preparations.

Table 4-3. Hemolytic activity of 10 mg/ml and 1 mg/ml nanoparticle dispersions after 1 h incubation at 37 °C. The extinction of PBS was subtracted from the other measurement data and set to zero. All values are given in reference to the 100 % hemolytic SDS solution. The mean values with the respective range are given (n = 3, references n = 9).

	Hemolysis of 10 mg/ml nanoparticles		Hemolysis of 1 mg/ml nanoparticles	
	mean [%]	range [%]	mean [%]	range [%]
PBS	set as 0	0.71		
PGA-BB	-0.84	0.50	-0.65	0.39
PGA-S20	27.7	5.24	1.1	0.20
PGA-S20 + Pol188	6.1	0.59	0.9	0.18
PGA-S50	1.8	1.04		
PGA-S65	0.49	0.07		
SDS 2 %	100	8.78		

4.1.12 Cell culture studies

4.1.12.1 Cell viability and proliferation

The optimal cell number per well was determined by correlation of the seeded cell number with the resulting fluorescence intensity after 3 d (data not shown). Assays based on measuring metabolic activity of living cells require good linear correlation and a high slope of this curve to provide accurate and sensitive results [252,253]. When the initially seeded cell numbers are too high, linearity of the slope is lost and results in the upper fluorescence range can be underestimated. With 10^3 to 10^4 seeded cells per well, the cell number vs. fluorescence curve showed good linear correlation ($R^2 = 0.999$). When the initially seeded cell numbers exceeded 10^4 linearity of the slope was lost. Therefore, with 5×10^3 cells per well a rather low initial concentration of cells was seeded (5×10^4 cells/ml), so that linearity was assured for the three day duration of the experiment. Assays based on measuring metabolic activity of living cells require good linear correlation and a high slope of this curve to provide accurate and sensitive results

[252,253]. When the initially seeded cell numbers are too high, linearity of the slope is lost and results in the upper fluorescence range can be underestimated.

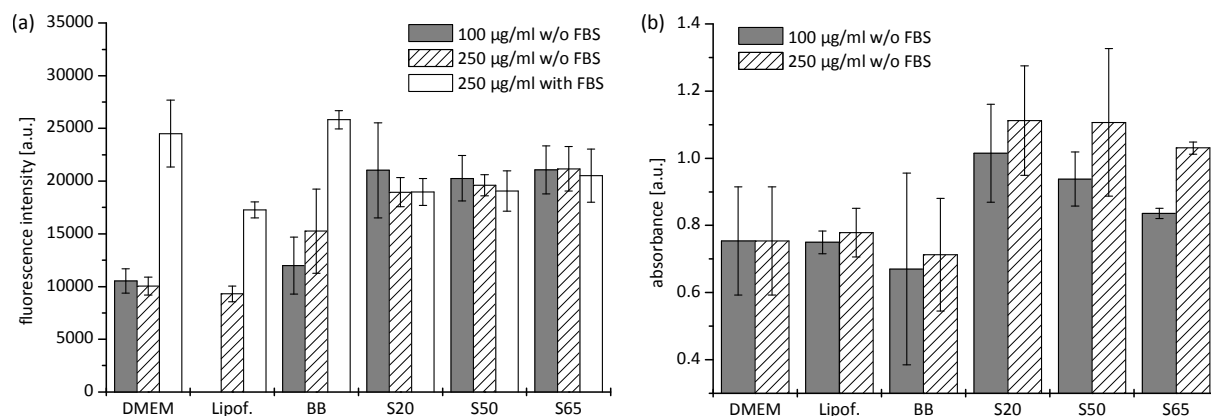


Figure 4-18. Cell proliferation of HepG2 cells after 24 h incubation with nanoparticle samples in different concentrations without (grey and hatched columns) or with (white columns) addition of 10 % FBS to the medium. Pure medium (DMEM) and the commercially available Lipofundin® N (Lipof., only in the concentration of 250 µg/ml) served as references. (a) QBlue assay as a measure of metabolic active cells and (b) modified LDH assay as indication of the cell amount. For each sample the mean and the standard deviation are shown ($n = 6$).

The QBlue viability assay was firstly performed in standard procedure without the addition of FBS to the culture medium. Pure culture medium (DMEM) and Lipofundin® N served as references. Lipofundin® N is a commercially available nanoemulsion for parenteral nutrition based on soya oil stabilized by lecithin and sodium oleate. It was used as a second reference for the high concentration samples. As expected, the metabolic activity of HepG2 cells did not change compared to DMEM. Nor did PGA-BB nanoparticles show a significant difference in the measured fluorescence intensity (Figure 4-18a, grey and hatched columns). In contrast, for the PGA-S20, -S50 and -S65 samples with 100 µg/ml and 250 µg/ml of nanoparticles an increased metabolic activity compared to DMEM was observed. However, no difference between the two concentrations could be detected.

In addition to the QBlue viability test, a modified LDH assay was applied to obtain information about the cell amount. The results of the LDH assay looked almost equal to those of the QBlue experiment although the standard deviations of the measured values were quite large (Figure 4-18b). Lipofundin® N and PGA-BB particles again didn't show any significant difference after 24 h compared to the culture medium whereas the Stearoyl-PGA nanoparticles showed higher absorbance values that indicate increased cell numbers, especially for the higher sample concentration.

The observed increase in metabolic activity (QBlue assay) and cell amount (LDH assay) after 24 h incubation might be an indication for metabolization of the Stearoyl-PGA polymers by the cells leading to increased cell activity and proliferation. As the PGA backbone did not show higher cell numbers or increased activity, it could be assumed

that the stearic acid fractions are primarily used by the cells, which is also in good accordance with the physiologic conditions [254].

To investigate whether better growth conditions for the cells would influence the results, the QBlue assay was performed again with DMEM containing 10 % of FBS as mitogen. Supplementation of FBS increased the metabolic activity of the untreated cells compared to cells in pure DMEM [255] to about double values (Figure 4-18a). The cells incubated with Lipofundin® N and PGA-BB particles also showed higher activities. The values for the Stearoyl-PGA samples, however, were about the same for both conditions. This supports the above stated hypothesis that in the absence of FBS, cells used the polymers for metabolic activity.

4.1.13 *In vivo* experiments

4.1.13.1 Tumor growth

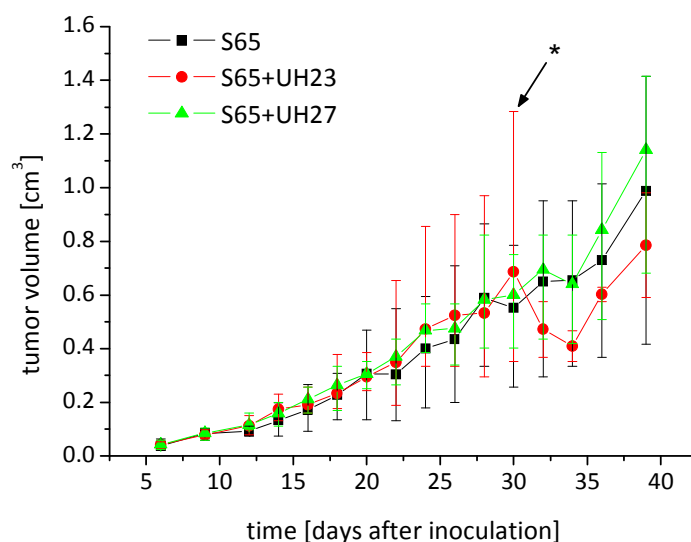


Figure 4-19. Comparison of tumor volume in different groups. Median and range are displayed respectively. * In group 2 one mouse had to be sacrificed after 30 d because of high tumor burden and weight loss.

All subcutaneous HT29 tumors grew gradually and their volumes increased about exponentially overall (Figure 4-19). After 26 d, the mice were randomized into three groups according to their tumor volume and injected with the respective nanoparticle samples. The tumor volume was comparable between the different groups until after 30 d – which was 4 d after nanoparticle injection – one mouse of group 2 had to be sacrificed because of high tumor burden and weight loss. All other mice initially gained weight and did not lose more than 2 g afterwards until the end of the study.

4.1.13.2 Fade of fluorescence after injection

PGA-S65 nanoparticles were selected for the *in vivo* study. They are solid, spherical in shape and their crystallinity accounts for about 50 %. With these features, they can be regarded as “standard” particles. Their body fate was monitored and compared with

physically and covalently coated PGA-S65 particles by measuring the *in vivo* fluorescence intensity of DiR by MSFI. The DiR signal was intended to track the location of the nanoparticles as the highly lipophilic dye ($\log P \geq 20$) with virtually no water solubility has practically no tendency to diffuse from the lipophilic nanoparticle core into the bloodstream. In the applied NIR detection range, the autofluorescence of the mouse body is negligible.

Figure 4-20a displays the fade of the DiR fluorescence signal in healthy SKH1 mice after injection of the different DiR loaded PGA-S65 nanoparticles.

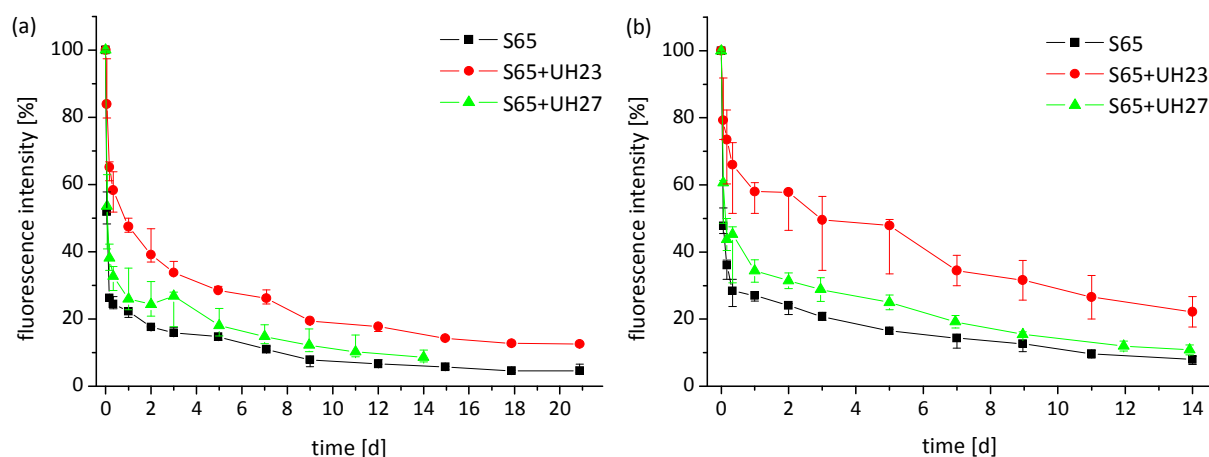


Figure 4-20. (a) Fade of NIR fluorescence signal in SKH1 mice. Median with minimum and maximum value are shown respectively ($n = 3$ in each group). Group 3 was monitored for only 2 weeks. (b) Fade of NIR fluorescence signal in tumor bearing Nude-Foxn1 mice. Median with minimum and maximum value are shown respectively ($n = 3$ in each group).

The signal of the uncoated nanoparticles dropped very fast to about 25 % of the initial intensity during the first 4 hours. Afterwards, the intensity faded gradually towards a value of about 5 % after 3 weeks. The fluorescence of the physically coated nanoparticles (S65+UH23), in contrast, did not show such a great loss of signal in the first day. About 50 % of the initial signal was still observed after 24 h, 25 % were measured after 1 week and at the end of this study, after 3 weeks, approximately 13 % were still remaining. This indicates that the physical coating with the HPMA copolymer was beneficial to protect the nanoparticles from MPS uptake and thereby to prolong their circulation time. The covalently coated nanoparticles, however, only revealed a smaller benefit in this study. The initial loss was not quite as high as for the uncoated nanoparticles with about 40 % remaining intensity after 4 h but after 1 week, the average intensity values were just around 3-4 % higher than those of the uncoated particles. Unexpectedly, the covalent coating with UH27 seemed to be less efficient than the physically attached UH23. The reasons for this discrepancy are a matter of speculation. Possible reasons are a higher thickness of the coating layer with the 31 kDa UH23 vs. the 20 kDa UH27, a differently structured shell with another density due to the different methods of attachment and particularly a more efficient coating reaction for UH23 compared to UH27.

In the Nude-Foxn1 mice (Figure 4-20b), the benefit of the UH23 coating was even higher than in the SKH1 mice. The signal of the physically coated particles was considerably higher than that of the uncoated sample from the beginning until the end of the experiment after 2 weeks. A loss of 50 % of the initial intensity wasn't reached before 3 d had passed. 22 % of the first signal were still remaining after 2 weeks compared to about 8 % for the uncoated nanoparticles. The covalently coated nanoparticles again showed only slightly higher intensities compared to the plain PGA-S65 particles.

Given that the only major difference between the SKH1 and the Nude-Foxn1 mice was the subcutaneous HT29 tumor in Nude-Foxn1, the slower fate of all nanoparticle samples, and especially of S65-UH23, in these mice could be caused by an extravasation of the particles in the tumors by the EPR effect. Due to the fact that solid tumors tend to lack lymphatics [32,139,141] the dye cannot be eliminated quickly, leading to an accumulation and retention in the tumor tissue and prolonged detectability. The higher circulation time of S65-UH23 particles in the bloodstream (as shown in healthy SKH1 in Figure 4-20a) could lead to a greater exploitation of the EPR effect and thus higher tumor accumulation.

4.1.13.3 *In vivo* distribution and tumor accumulation in Nude-Foxn1 mice

In vivo distribution of the nanoparticles is discussed here only in Nude-Foxn1 mice as the overall distribution in SKH1 mice was similar except for the tumor.

To compare all nanoparticle samples, the distribution of the DiR signal was firstly studied over time. As expected for nanoparticles [108,122,256], all samples showed high fluorescence signals in the liver already at the first measuring time point after 5 min. The high signal intensity reduced the automatically adjusted exposure time of the camera to such an extent that signals in other organs could hardly be detected in some cases. Therefore, in order to visualize other organs, the area of the liver was covered by a black plastic plate in selected images.

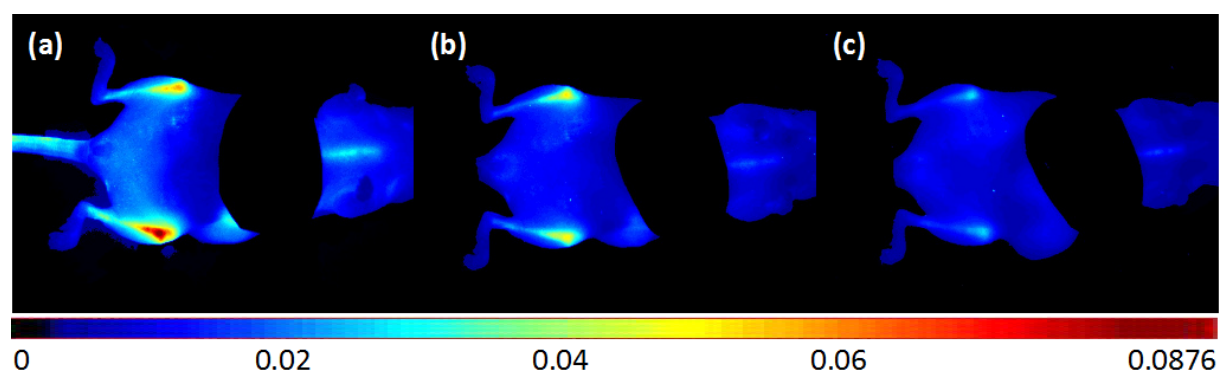


Figure 4-21. Distribution of PGA-S65 nanoparticles containing DiR in a Nude-Foxn1 mouse after (a) 5 min, (b) 24 h (2-fold magnification) and (c) 2 weeks (4-fold magnification).

For the uncoated PGA-S65 nanoparticles, DiR signal of considerable intensity was detected in the bones already after 5 min and remained until the end of the experiment after 2 weeks (Nude-Foxn1, Figure 4-21) or 3 weeks (SKH1, not shown). This points to

an accumulation of the particles in or on bones which was afterwards investigated in more detail (4.1.15).

After injection of the physically coated nanoparticles in SKH1 mice, a high Dy676 signal in the bladder was obvious in the first fluorescence image after 5 min and a lower signal after 90 min (Figure 4-22). This shows that the dye was rapidly eliminated via the kidneys and thus present in the urine. Given that the amide bond between Dy676 and the HPMA copolymer should not be cleaved *in vivo*, this is a strong indication that free unbound UH23 polymer was present in the injected sample. With about 31 kDa, the molecular weight of UH23 is below the renal threshold of 45-50 kDa for HPMA copolymers [148,257]. However, it was reported [148,149] that amphiphilic HPMA copolymers bearing cholesterol, similar to UH23, *in vitro* self-assemble into micelles with an average hydrodynamic diameter of about 30 nm which are too large for renal filtration [148]. The presence of such micelles was also observed for the UH23 copolymer in AF4 measurements (Figure 4-6). Yet the high Dy676 signal in the bladder points to dilution of the micelles below the critical micelle concentration (2.1×10^{-5} g/ml for a similar copolymer with 3 % cholesterol vs. 2.2 % in UH23 [149]) in the bloodstream and a disassembly into polymeric monomers. This was confirmed by the pure UH23 copolymer sample which was injected as reference and also revealed high signals in the bladder after 5 and 90 min (not shown).

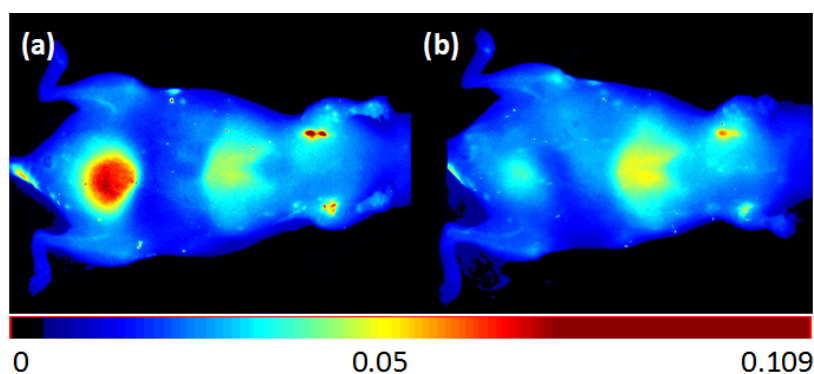


Figure 4-22. PGA-S65+UH23 nanoparticles without ultrafiltration: Distribution of Dy676 signal in SKH1 mouse after (a) 5 min and (b) 90 min.

To remove the free unbound UH23 copolymer from the nanoparticle suspension, the freshly prepared S65+UH23 sample for the Nude-Foxn1 mice was purified by ultrafiltration. After injection of the purified sample, none of the four Nude-Foxn1 mice showed any signal in the bladder after 5 min (e.g. Figure 4-23a). In two of the mice, however, a Dy676 signal was visible after 90 min in the bladder (e.g. Figure 4-23b). This could be either due to a small fraction of remaining free UH23 polymer in the purified sample or resulting from a detachment of the physical coating from the PGA-S65 nanoparticles during circulation in the bloodstream.

The image sequence in Figure 4-23 illustrates the distribution of the Dy676 signal after injection in a Nude-Foxn1 mouse and the successive accumulation in the HT29 tumor. It

is obvious that the intensity initially increased in the liver but already after 4 h considerable signal was found in the HT29 tumor. Again, fluorescence in the bones was visible, mainly in the femurs. The tumor signal continuously increased during the first four days and slightly decreased afterwards. The same applied to the UH23 reference which also showed high tumor accumulation after one day until the end of the experiment. No signal in the bones has been detected.

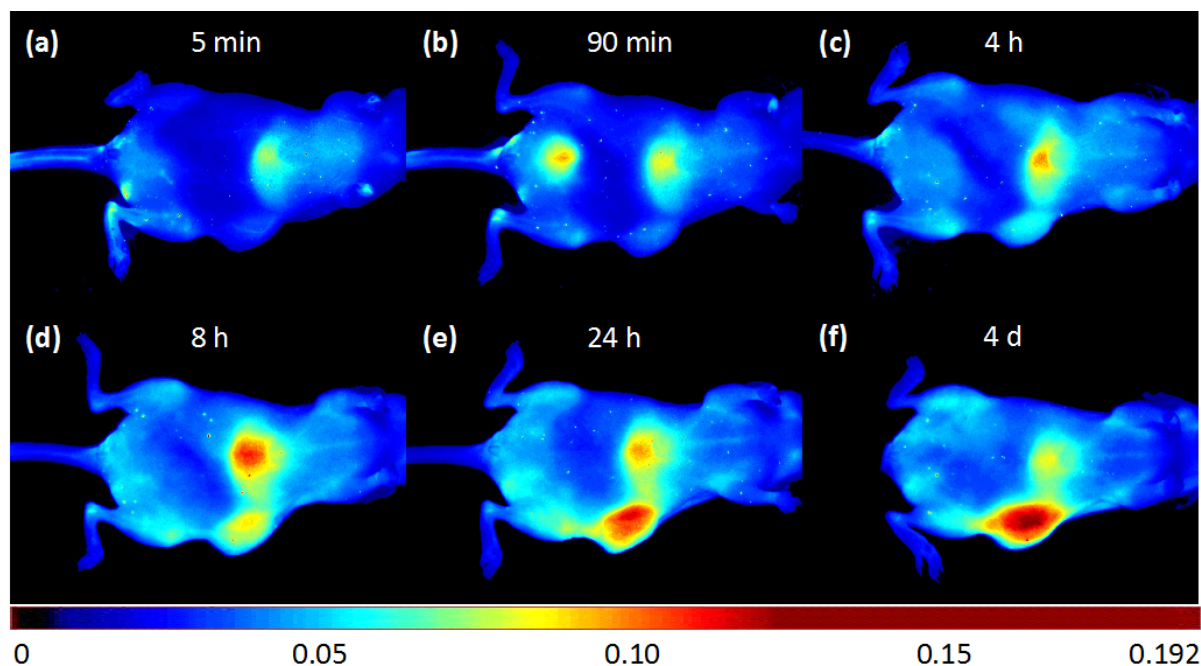


Figure 4-23. PGA-S65+UH23 nanoparticles with ultrafiltration in Nude-Foxn1 mouse: Distribution of Dy676 signal after (a) 5 min, (b) 90 min, (c) 4 h, (d) 8 h, (e) 24 h and (f) 4 d.

Monitoring of the DiR signal revealed high intensities in the liver from 5 min until the end of the experiment. Figure 4-24 displays images with unmixed DiR (green) and Dy676 (red) signals after 4 d. Without coverage of the liver area (a), the DiR signal is only visible in the liver. Nevertheless, covering of the liver area during fluorescence imaging (b) visualized DiR signals in bones and also in the tumor. The yellow signal in the tumor is generated by an overlay of red and green, displaying the presence of both dyes in the HT29 tumor. Separate images of fluorescence intensity distribution for each dye (Figure 4-25) supported this finding.

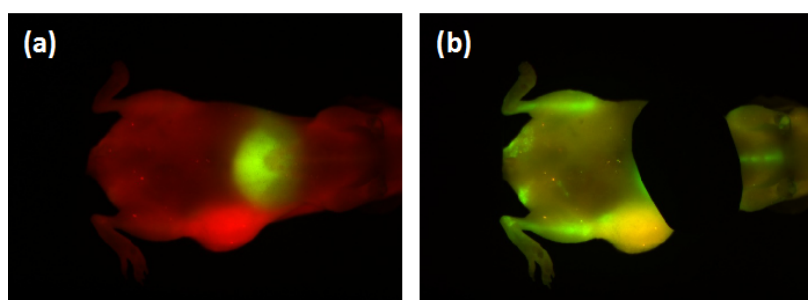


Figure 4-24 PGA-S65+UH23 nanoparticles purified by ultrafiltration in Nude-Foxn1 mouse after 4 d: Unmixed composite with green DiR and red Dy676 signal are shown (a) without and (b) with coverage of the liver.

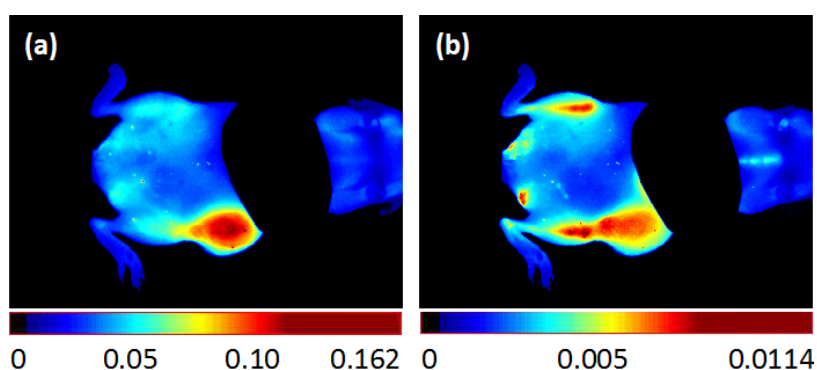


Figure 4-25. PGA-S65+UH23 nanoparticles with ultrafiltration in Nude-Foxn1 mouse after 4 d: signal intensity of Dy676 (a) and DiR (b). The area of the liver was covered with a plastic plate.

Why the intensity distributions of Dy676 and DiR in liver and tumor were so different, cannot be answered easily without further investigation. There are a number of possible explanatory approaches and the true cause might be a combination of various factors. First of all, as mentioned before, some unbound UH23 conjugate might have been present in the sample which was not eliminated by renal filtration and circulated in the bloodstream as micelles. Also a partial detachment of the UH23 coating from the PGA-S65 nanoparticles during circulation might be considered. Uncoated or partially coated nanoparticles would be more likely to be taken up in the liver and coated nanoparticles as well as UH23 micelles would show prolonged circulation and enhanced uptake into the tumor. The quite effective tumor accumulation of such micelles has been reported earlier [148] and was confirmed here by the performance of the injected UH23 reference. Another possibility would be the release of DiR from the nanoparticles. Although this is a very lipophilic dye with a very low tendency to diffuse into the blood (the very similar DiI was reported to transfer from lipid nanoparticles $\leq 5\%$ in 2 weeks [258]), it might be possible that DiR which was located on or close to the surface of the particles could be released and accumulated in the liver. Also destabilization of the particles in the bloodstream, e.g. by attached proteins, and a subsequent release of DiR should be considered as reported for liposomes and micelles [125]. A further factor which could influence signal intensities in the liver is the different penetration depth of light as a function of its wavelength [259,260]. It is known, according to Beer-Lambert

law that the intensity of an electromagnetic wave decreases exponentially during the passage through an absorbing material. With increasing wavelength, the absorption coefficient decreases, leading to a higher penetration depth in the given material [260]. For example, a study of Stolik *et al.* [259] reported penetration depths for liver tissue (*in vivo* and *postmortem*) which were about 2.5-fold for $\lambda=780$ nm compared to $\lambda=633$ nm (the wavelengths which are closest to the excitation wavelengths of DiR and Dy676). In view of this, it is likely that the NIR dye DiR (710-760 nm) is excited to a considerably higher extend in deeper tissues, especially in the liver, than Dy676 which is excited in the red wavelength range (615-665 nm). For the excitation of Dy676 in the subcutaneous tumor, however, the light only has to pass the already tensioned skin without the “hindrance” of many blood vessels, etc. Aware of this, simultaneous measurements of differently excited dyes must be generally interpreted with caution.

For the covalently coated PGA-S65 nanoparticles the observations were similar as described for the physically coated sample (images not shown). Here as well Dy676 signal was found in the bladder after 5 min, 90 min and in some of the mice still after 4 h. This was rather surprising as neither the amide bond to the covalently attached UH27 conjugate nor the amide bond of the linked dye should be cleaved *in vivo*. Under this assumption, this was evidence for the presence of free unbound UH27 in the sample. In contrast to UH23, this conjugate doesn't have hydrophobic moieties for self-assembly and is with about 20 kDa also substantially smaller. For such HPMA copolymers rapid elimination from the bloodstream and quick elimination by renal excretion is known [139]. The accumulation in the tumor seemed to be lower than for the UH23 coated particles.

In order to quantify or rather estimate tumor accumulation of the different nanoparticle samples, the tumor accumulation value (TAV) was calculated according to Equation 3-2 [119].

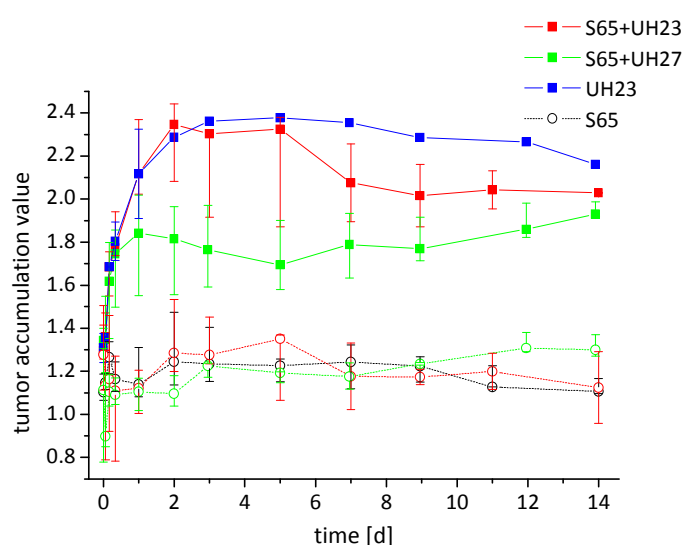


Figure 4-26. Tumor accumulation value of the Dy676 signal (solid lines) and the DiR signal (dotted lines, open symbols) in the different groups. Median with minimum and maximum value are shown respectively.

The TAV of the Dy676 signal (Figure 4-26, solid lines) sharply increased during the first 24 h after injection of all samples. For the PGA-S65+UH27 sample, the signal afterwards remained about constant before it slightly increased again after 9 d. The signals of the UH23 coated sample and the UH23 reference first increased until 48 and 72 h before remaining constant and decreasing after 5 d. After 2 weeks, the TAV of the Dy676 signal was between 1.9-2.2 for all groups. Similar values have been reported for the accumulation of linear and star-like HPMA copolymers in HT29 tumors [119]. The variation between the 3-4 mice within one group was rather high at the beginning and decreased towards the end of the experiment. The data of the UH23 control resulted from two mice until 24 h and from only one mouse afterwards. As already assumed on the basis of the prolonged circulation and prolonged detectability of the S65+UH23 sample as well as the unmixed fluorescence images, tumor accumulation was considerably more effective for the physically coated sample than for the covalently coated, at least for the most part of this study. Why the TAV decreased for S65+UH23 towards the end while it increased for S65+UH27, cannot be elucidated by this data.

The TAV of the uncoated nanoparticles could only be calculated by means of the DiR signal. Within all groups, the TAV of the DiR signal (Figure 4-26, dotted lines) also showed high variation and the values were much smaller than those for Dy676. These lower numbers of DiR are primarily a result of the much higher DiR signals in the liver. The calculation method of the TAV is based on the ratio of the fluorescence signal of the tumor area and the overall signal of the mouse body without the tumor area. Thus, the high DiR intensities in the liver lead to high values for the denominator of this equation and thereby to smaller values for the TAV.

There was no considerable difference of the TAV for DiR between the three groups for 9 d. After 7 d, the TAV of the covalently coated particles increased whereas the value of the uncoated NPs slightly decreased which finally lead to a higher accumulation of the covalently coated particles in the tumor compared to the uncoated sample.

These results seem to indicate that the HPMA coating and the prolonged circulation time did not automatically lead to higher accumulation of DiR loaded nanoparticles in the tumor which was rather unexpected. In fact, this calculation method suggests that the coated particles extravasate only about as effective as the uncoated sample. Under the assumption that the lipophilic DiR is not released from the particles to a relevant extend, this would consequently mean that the high TAVs of Dy676 only resulted from the accumulation of free HPMA copolymers, not attached to nanoparticles. But as discussed above, this assumption is not unquestionable.

However, these are only the results of one method, which is influenced by many variable factors. As already mentioned, the variability within the groups was high for both dyes. Moreover, mouse handling lead to unavoidable variation when placing the mice in lateral position for imaging. The determination of tumor contours in the analyzation program was sometimes highly ambiguous as well.

The above described direct interpretations of the fluorescence images seemed to show higher DiR signals in the tumor for the coated particles, especially for S65+UH23, compared to the uncoated particles both in single spectra images and in unmixed composites.

4.1.14 *Ex vivo* experiments

To shed more light on the body distribution, various organs were removed and analyzed after the mice had been sacrificed at the end of the study. Stomach and intestine could not be used for analysis because of high autofluorescence in the red filter set which was used for the detection of Dy676.

As also observed *in vivo*, the signal intensity in the organs was different for the two dyes. Figure 4-27a depicts the distribution of the DiR signal, which was – as already seen in the *in vivo* images – predominantly found in the liver for all samples. The percentage for the PGA-S65+UH23 group in the liver was higher than for the other groups and thereby lower in most other organs. The second highest intensity in all groups was detected in the spleen which is, besides the liver, also known as a preferential side for nanoparticle accumulation [108,122,256,261]. This data demonstrates that the HPMA coating was not beneficial to avoid uptake of PGA-S65 nanoparticles in these organs of the MPS.

For the uncoated PGA-S65 nanoparticles, the concentration in bones, adrenal glands and lung seem slightly higher than for the coated nanoparticles. DiR intensity in the tumors was only about 2-4 %.

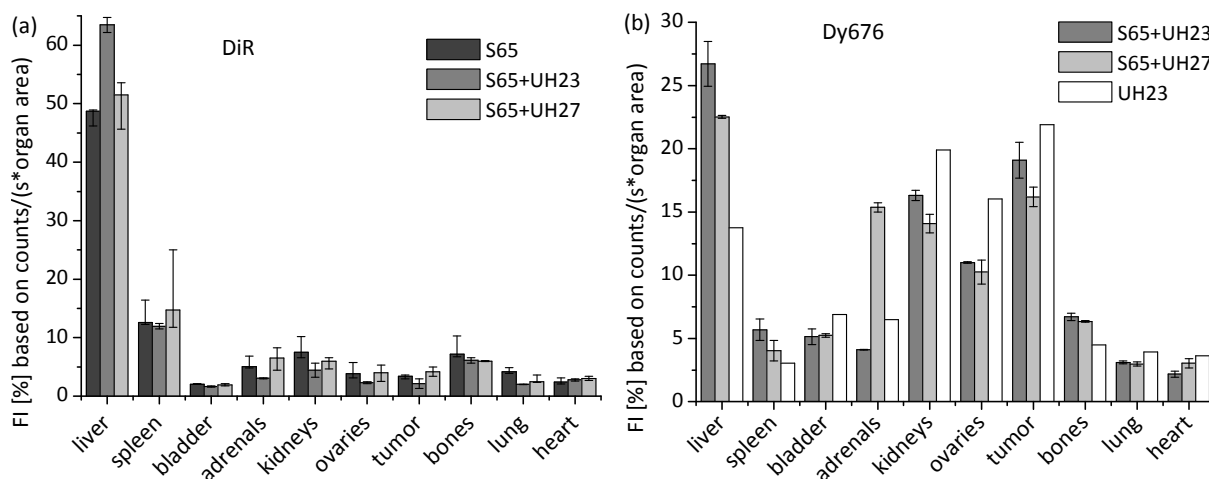


Figure 4-27. *Ex vivo* (a) DiR and (b) Dy676 fluorescence intensity (FI) of the mouse organs after 14 d displayed in percent based on the data of three mice per group for the particles and one mouse for the UH23 control. The FI values are calculated by dividing the organ signal (counts/s exposure time) by the organ area (mm) projected in the image. Median with minimum and maximum value are shown respectively.

The intensity distributions of the Dy676 signal, corresponding to the coated nanoparticles as well as the free HPMA copolymers, are displayed in Figure 4-27b. As larger nanoparticles are more likely to be taken up by the MPS [94,129] than free polymers or small micelles, it is unsurprising that both particle samples showed higher

accumulation in liver and spleen than the UH23 control. The percentage of Dy676 signal in liver and spleen was, however, less than half compared to the DiR signal for the coated nanoparticles.

Intensity in the tumor showed the same pattern as the calculated TAV (Figure 4-26) with about 16 % for S65+UH27, 19 % for S65+UH23 and 22 % for the UH23 control. Magnified images of transected tumors revealed the highest accumulation in the center and on the ventral side of the tumor for all samples as exemplarily shown in Figure 4-28. Most likely, vascularization of these areas was higher, leading to better blood supply than in the skin facing exterior parts of the solid tumor.

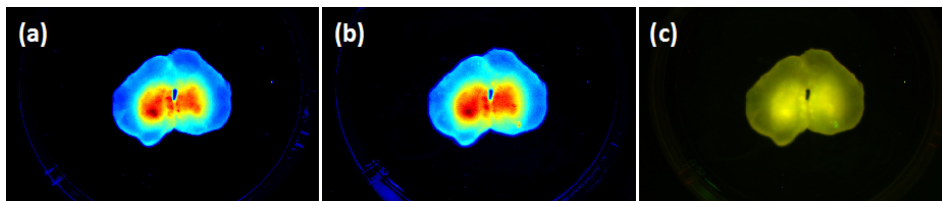


Figure 4-28. Exemplary fluorescence image of an autopsied tumor (cross section). The curved surface of the tumor, here lying on the outside, was the side facing the skin in vivo. (a) Intensity weighted single spectrum image of DiR. (b) Intensity weighted single spectrum image of Dy676. (c) Unmixed composite with overlaid signals (red Dy676, green DiR). The mouse had been treated with S65+UH23 nanoparticles.

Surprisingly, the signals in the adrenal glands and the ovaries showed also relatively high values for all samples. Figure 4-29 displays images of the removed organs.

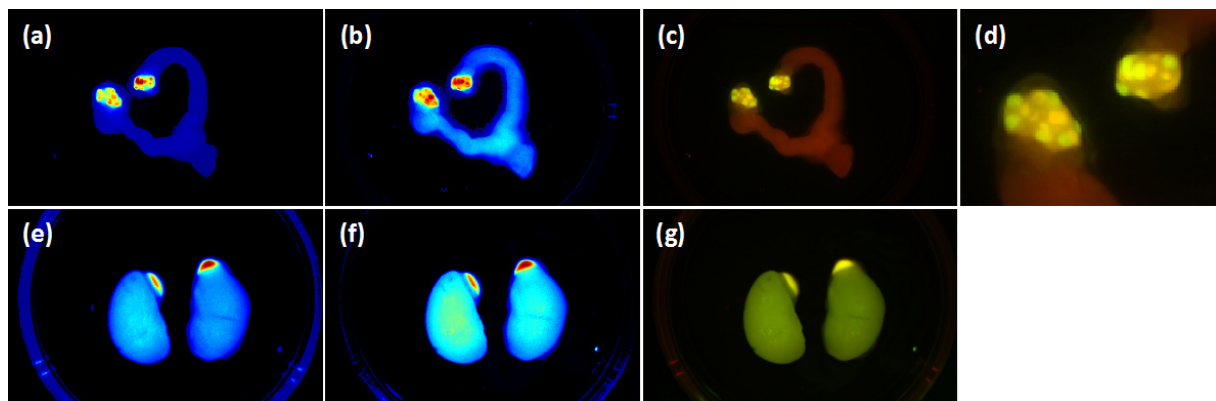


Figure 4-29. Exemplary images of removed ovaries with fallopian tubes (top, a-d) and kidneys with adrenals (bottom, e-g). From left to right are shown respectively: (a,e) Intensity weighted single spectrum image of DiR. (b,f) Intensity weighted single spectrum image of Dy676. (c,g) Unmixed composite with overlaid signals (red Dy676, green DiR). (d) Magnification of ovaries. The mouse had been treated with S65+UH23 nanoparticles.

Accumulation of nanoparticles or liposomes in mouse ovaries has been reported before, e.g. in [122,262-266] and was studied in more detail by Schädlich *et al.* [262]. As visualized in the magnification of the ovary in Figure 4-29 (d), the fluorescence was not equally distributed in the ovary but elevated signal was observed in round substructures. This could indicate an enrichment in tertiary follicles or – as suggested in

other studies [262,263] – in the cells of the corpus luteum. For this highly proliferating and highly vascularized tissue [267] an accumulation similar to the EPR effect has been proposed [262]. However, accumulation in ovaries has been reported only for nanoparticles ≥ 45 nm and not for free polymers ≤ 35 nm so far. The high Dy676 signal for the free UH23 conjugate was therefore highly surprising and might be attributed to the accumulation of the self-assembled micelles of the polymer.

Accumulation of nanoparticles and certain aminated polymers in adrenal glands was also reported before [264,266,268-271] but without any further investigation of reasons. This could also not been studied in more detail here.

For S65+UH23 and the UH23 control, Dy676 intensity in the bladder and the kidneys were similar respectively. In contrast, the PGA-S65+UH27 sample showed threefold signals in the kidneys without higher intensities in the bladder. The signal of DiR in the kidneys (Figure 4-27a) was only about twice compared to S65+UH23. This indicates an accumulation of UH27 coated nanoparticles and free UH27 conjugate by specific interaction of UH27 with the kidneys apart from the normal excretion via this route. Kidney accumulation of certain HPMA copolymers was already observed in several studies before [119,272-276]. Different structural aspects have been suggested to increase accumulation, such as high modification through attached drugs, peptide moieties or functional groups [272,273,276], negative charge [274,275] or interaction of free hydrazide groups with the anionic membrane of the kidney cortex [119]. For the different accumulation of UH23 and UH27, however, the reason is not obvious at all. Hydrazide groups are only present in UH23 and not in UH27, which excludes this thesis. As the zeta potential of both nanoparticle samples was very similar, the argument of negative charge does also not apply here, at least not for accumulation of the coated particles. Structural differences between the two HPMA conjugates are the lower molecular mass of UH27, the possible self-assembly of UH23, the higher Dy676 content of UH27 and the different spacers between backbone and dye (6-aminohexanoic acid for UH23 and β -alanine for UH27). From the finding of Lammers *et al.* [272,273] who reported a higher accumulation of drug-functionalized HPMA copolymers, it could be speculated that the higher content of Dy676 might promote the accumulation of UH27 in the kidneys while the attached dye in UH23 might be hidden within the micelles and protected from direct contact with the environment.

In view of the already mentioned (Figure 4-21) observation of fluorescence signals in the bone regions, the left femur of each mouse was also removed and measured by MSFI along with the other organs. The nanoparticle samples showed higher signals in the bones compared to the UH23 control, though, no huge enrichment could be detected in the bones at the end of the study. However, the mice which were autopsied after 24 h showed higher bone signals of about 10 % for the uncoated particles, supporting the observations of the *in vivo* images (Figure 4-21). This accumulation points to a specific interaction of the PGA polyester with bones which was investigated in more detail afterwards (4.1.15).

The signals in lung and heart were similar to each other and comparable to the autofluorescence of these organs in the red filter set.

In general, all of the presented fluorescence data must be treated with caution. Although the method was designed to minimize measurement errors, the different light absorption within the autopsied organs and their variable thickness still biased the results considerably. The signal intensity was calculated in counts per [second exposure time × organ area] by normalizing the measured fluorescence to the applied exposure time and to the projected organ area which was viewed from above. Thereby the thickness or volume of the organ was neglected which would have been rather complex to assess and to include in the calculation. Undoubtedly, the recorded intensity from a thicker organ is higher than from a thinner organ of the same area, albeit the excitation in deeper layers is lower and the emitted signal attenuated. For this reason, signal intensity of large organs with high thickness, especially the liver, was most likely overestimated compared to thin organs such as adrenal glands, ovaries and bones. Although the autopsied tumors were also voluminous, the situation was rather contrary due to the irregular distribution of the signal. Because the fluorescence signal was mainly concentrated in the center of the tumors and they were measured as a whole, the obtained value was probably underestimated. The different absorption coefficients for the organs and the resulting discrepancies in penetration depth for the exciting light as well as the variable extent of scattering and absorption of the emitted fluorescence are further parameters of major influence which could not be taken into account in this method.

4.1.15 Investigation of “bone targeting”

The observed attraction of PGA-S65 nanoparticles to bones could be caused by various reasons. Possible mechanisms are an attachment of PGA to the inorganic matrix, mainly hydroxylapatite (HA) or calcium ions, an attachment to the organic matrix or phagocytic uptake by mononuclear macrophages of the MPS lining the bone marrow sinusoids [160-162]. To further elucidate the relevant mechanism, the possible binding of the nanoparticles to Ca^{2+} ions was investigated by complexometric titration and a binding assay with HA.

Both methods of Ca^{2+} titration led to unsatisfying outcomes despite various efforts in optimization of the experimental set-ups. The first applied method [213] with calcein solution as indicator didn't reveal a sharp titration end point and thus yielded variable results. The indication of the end point in test experiments was better with Eriochrome black T in the second method [214]. However, when performing the assay with the addition of nanoparticles, higher volumes of EDTA- Na_2 solution were spend to reach the titration end point compared to blank samples. This indicated that the centrifugation of the samples after the incubation did not completely eliminate all nanoparticles from the supernatant which then probably bound EDTA- Na_2 during titration. Not even centrifugation at 40000g for 30 min led to satisfying values.

Nevertheless, the results of the hydroxylapatite (HA) assay support the *in vivo* discovered phenomenon of the attraction of Stearoyl-PGA nanoparticles to bones. HA as an integral part of bones also revealed to bind PGA-S65 nanoparticles in this assay (Figure 4-30a) so that decreased fluorescence intensity in the supernatant was measured after centrifugation. In contrast, cetyl palmitate (CP) SLNs which were used for comparison did not bind to the HA powder at all (Figure 4-30b). This indicates that the binding effect is not unspecific but at least somewhat specific for the PGA based nanoparticles.

The relative part of nanoparticles bound to HA decreased about exponentially (Figure 4-31a; $R^2 = 0.995$) from 73 to 14 % by rising the concentration tenfold, yet the absolute amount thereby increased from 7.5 to 14 %. The second experiment with different amounts of HA (Figure 4-31b) showed a linear dependency ($R^2 = 0.9996$, fit not shown) between the HA mass and the bound fraction of PGA-S65 nanoparticles. The CP SLNs again did not show any binding effects. Both results indicate an equilibrium reaction for the binding of PGA-S65 nanoparticles to HA. The more HA is available, proportionately more nanoparticles attach to it. However, the more nanoparticles are present in the mixture, the more saturated does the surface of HA get so that the increase of the binding is only moderate.

Linearity of fluorescence vs. concentration in the range of the experiment was ensured by calibration (data not shown).

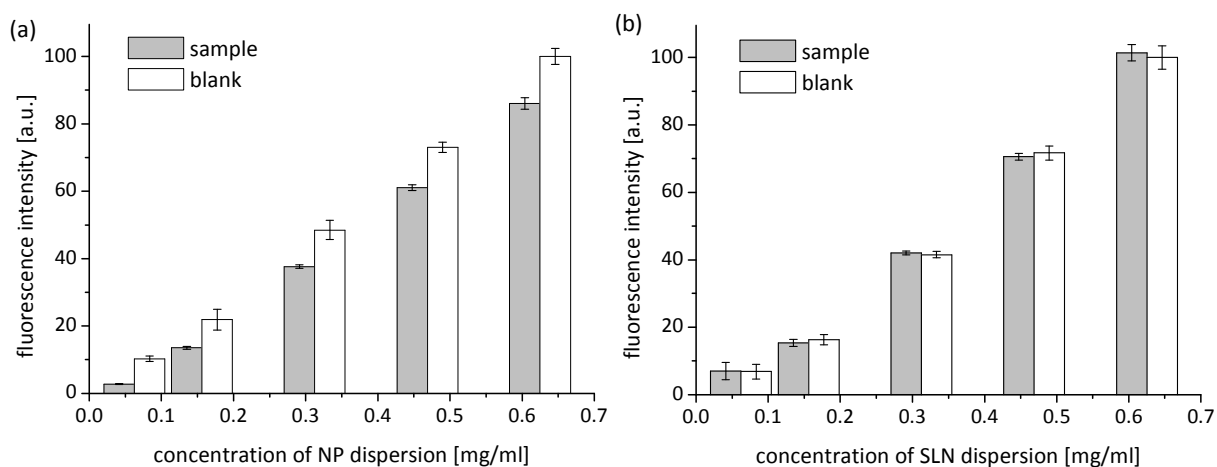


Figure 4-30. Fluorescence intensity of supernatant in samples (grey columns) and blanks (white columns) of PGA-S65 nanoparticles (a) and CP SLNs (b). For better comparability, the intensity of the blank with the highest concentration was set to 100.

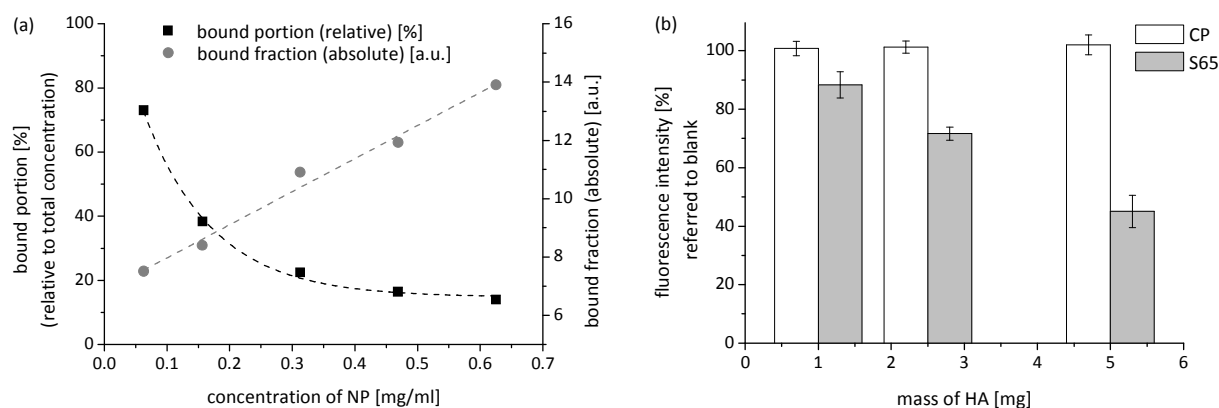


Figure 4-31. (a) Dependency of the binding of PGA-S65 nanoparticles from the total nanoparticle concentration. (b) Influence of HA amount incubated with PGA-S65 and CP nanoparticles (medium concentration of 0.3125 mg/ml).

A possible reason for the binding of PGA based nanoparticles to HA might be the presence of free carboxyl groups on their surface. It is known that Ca^{2+} binding domains of several proteins, such as osteonectin, are acidic regions with aspartic (Asp) and particularly glutamic acid (Glu) sequences [277-279]. It has been shown that small acidic peptides are preferentially adsorbed on the surface of HA *in vitro* [280]. *In vivo*, fluorochromes with carboxyl groups, like calcein, were used to target microcracks by chelating Ca^{2+} ions of bone surfaces [281]. Moreover, molecules and nanoparticles functionalized with Asp or Glu were reported as bone targeting moieties [282-284]. In view of this, the enhanced fluorescence signal of the bones, especially for uncoated PGA-S65 nanoparticles, could result from the higher number of free carboxyl groups compared to the covalently coated sample and the more exposed carboxyl groups compared to the physically coated particles.

4.1.16 Further investigations of coated nanoparticles

In view of the *in vivo* results which indicated an incomplete coating reaction for PGA-S65 nanoparticles with UH23 and particularly with UH27, all coated samples were investigated in more detail.

4.1.16.1 Physical coating

The PGA-S65 nanoparticles loaded with DiR and coated with UH23 which were used for the *in vivo* study were applied to gel filtration in a Sephacryl® S-300 column. Only one peak was observed after separation, corresponding to the nanoparticles and no evidence of free HPMA copolymer was found. With regard to the *in vivo* study, where unbound UH23 was detected, it was hypothesized that free UH23 formed high molecular weight micelles as already known for similar cholesterol bearing HPMA copolymers [148,149]. It is possible that these micelles could not be separated from the nanoparticles by gel filtration due to the limited length of the column. To elucidate this, the one observed peak was divided into three fractions and analyzed by VIS spectrophotometry (Figure 4-32). The peak at 681 nm corresponds to Dy676 of the coating polymer and the peak at

756 nm to DiR which was incorporated in the nanoparticles. Due to the sloped baseline and the overlapping peaks, a quantitative interpretation of the spectra was not possible. Nevertheless, it is obvious that the content of nanoparticles drastically decreased from fraction 1 to 3. This finding supports the hypothesis of UH23 micelles with a molecular weight too high to be separated from the nanoparticles during the passage in the Sephacryl® column. The higher intensity of Dy676 in fraction 2 and 3 indicates the presence of free unbound HPMA copolymer in this sample.

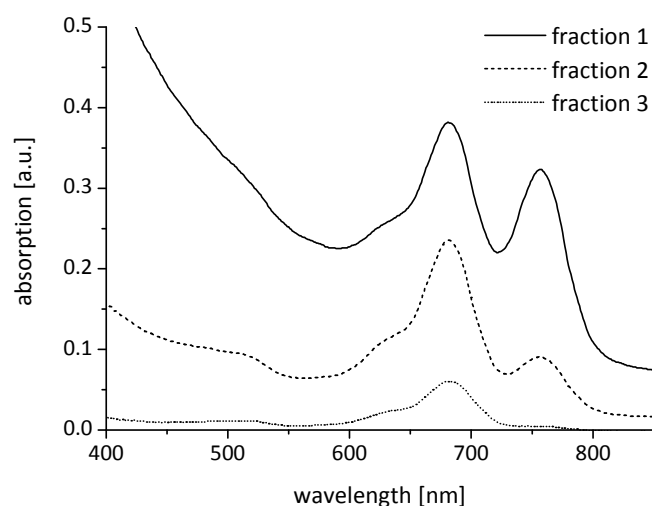


Figure 4-32. VIS spectra of 3 peak fractions after gel filtration of PGA-S65-DiR-UH23 nanoparticles.

4.1.16.2 Covalent coating with UH26

During gel filtration of PGA-S65 nanoparticles coated with the Dox-bearing UH26 on Sephacryl® S-300 there was no evidence of free unbound UH26 conjugate. It seemed that the majority of the coating polymer was covalently attached to the surface of the nanoparticles in all cases (different ratios polymer/nanoparticles). This was further studied by amino acid analysis which revealed 8.5 wt% of Doxorubicin in UH26. This means that a quantitative coating with the ratio 2/1 would result in coated nanoparticles with 2.8 wt% of Dox. For two fractions of coated nanoparticles which were analyzed after gel filtration contents of 1.7 and 2.6 wt% of Dox were observed. Due to the limited amount of sample, both fractions were measured only once and no further experiments could be conducted. Nevertheless, it seemed that the coating process was almost quantitative for one analyzed fraction and about 60 % for the other. The zeta potential, which was close to 0 mV for both fractions, indicated a complete conversion of carboxyl groups for this sample.

4.1.16.3 Covalent coating with UH27

After the linking reaction, the nanoparticles were colored blue-green which indicated successful coating with the Dy676-bearing HPMA copolymer UH27. During purification by centrifugal ultrafiltration, however, the eluates of the first washing steps were colored. This demonstrated that the reaction did not proceed quantitatively as still free

UH27 was present. The zeta potential of -11.1 mV supported this finding. Repetition of the coating reaction with the same and with a freshly synthesized UH27 conjugate again showed only partial conversion, verified by VIS-spectrophotometry.

Most probably, the reason for the incomplete reaction was steric hindrance of the functional groups. As the few carboxyl groups of the PGA backbone are distributed in the structure of the nanoparticles and the terminal amino groups of UH27 are likely to be hidden in the polymer coil, the functional groups hardly ever meet each other in the reaction mixture.

The same assumption applies to the coating reaction with UH26 where, however, the reaction seemed to be efficient. A possible explanation for the seemingly successful coating might be the structure motif GlyPheLeuGly-DOX of this polymer which is hydrophobic and thus working like a hydrophobic anchor similar to cholesterol. With it, the unbound polymer molecules can attach physically to the nanoparticles, pretending a quantitative coupling reaction. As this hydrophobic structure is missing in the UH27 conjugate, the unbound molecules are in this case not or only weakly attached to the nanoparticles and can thus be separated by ultrafiltration.

4.2 PGA based implants

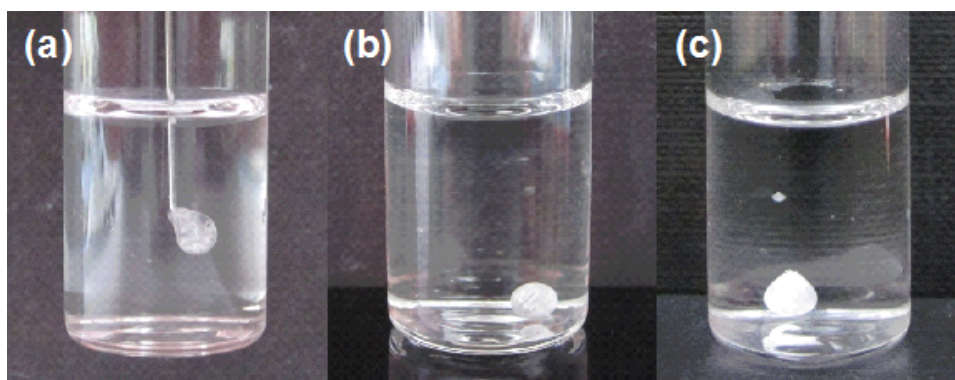


Figure 4-33. Injection of PGA-L25 into PBS. (a) during injection with a 25 G needle. (b) 1 min after injection. (c) 6 h after injection.

After injection of Lauroyl-PGA into PBS buffer, which is exemplarily shown for PGA-L25 in Figure 4-33, the polymer formed a rather spherical shape. This indicated surface minimization to decrease the contact area of the lipophilic polymer with the buffer. For different samples, this allows good comparability due to a similar surface area. The same behavior was also reported for hexPLA [187] which is a promising material for injectable viscous implants.

4.2.1 $^1\text{H-NMR}$ relaxometry

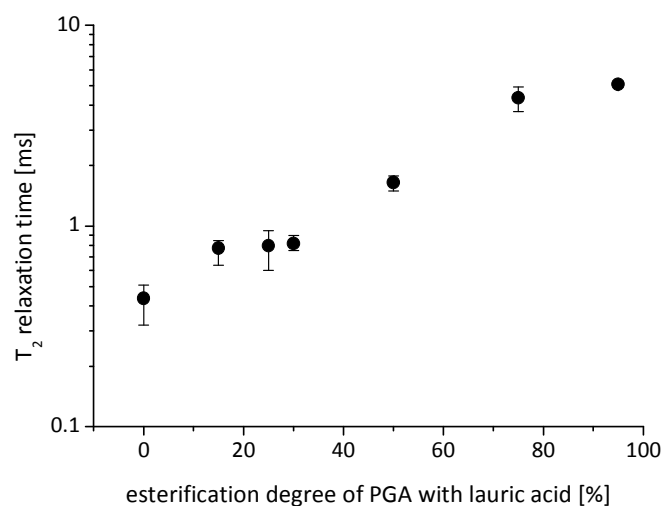


Figure 4-34. Influence of the esterification degree of Lauroyl-PGA on the transversal relaxation time T_2 of the polymers. The mean value and the range are displayed for 3 measurements each.

The non-invasive method of $^1\text{H-NMR}$ relaxometry provides information about the physical state and the mobility of protons [285]. The transverse relaxation time T_2 , characterizing the signal decay, decreases with reduced mobility [191-193]. In this study, T_2 relaxation times of different Lauroyl-PGA polyesters were measured in order

to get information about the mobility of their protons and thereby indication about the viscosity of the polymers [194].

As depicted in Figure 4-34, the obtained T_2 relaxation times of the samples with low esterification degrees PGA-L15, -L25 and -L30 were only slightly higher than the value of the unsubstituted PGA backbone. The low relaxation times below 1 ms indicate high viscosity of the polymers with rather immobile polymer chains. For $T_2 < 1$ ms, obtained values should be considered with caution, as information is lost in the CPMG measurement when the relaxation times approach a similar magnitude than the echo spacing (0.135 ms) [194]. The protons of the polymers with higher amounts of lauroyl side chains (PGA-L50 and particularly PGA-L75 and -L95) show increased mobility, which is expressed by higher T_2 relaxation times. However, compared to e.g. the T_2 of pure oleic acid (173 ± 7 ms) which is a fluid fatty acid, the transverse relaxation time in these polymers is still rather low. This demonstrates a strong immobilization of the chains in Lauroyl-PGA.

4.2.2 Texture analysis

Texture analysis was performed in order to get further information about the mechanical properties of Lauroyl-PGA polyesters. The following parameters were calculated from the compression curves as illustrated in Figure 4-35a [286-288]:

- Hardness (1, peak positive force): The load detected at the highest peak during compression. Hardness is the force necessary to attain a given deformation.
- Work (2, total positive area): The integrated area under the compression cycle. It displays the total energy required to penetrate the sample which is a measure of the internal strength of bonds within a product.
- Adhesive force (3, peak negative force): The maximum negative load. It is the force required to “pull” the probe from the sample.
- Adhesiveness (4, total negative area): The integrated area under the negative peak as the probe withdraws from the sample after the compression. Adhesiveness is the work necessary to overcome the attractive forces between the material and the surface of the probe as it retracts, thus being a measure of stickiness.

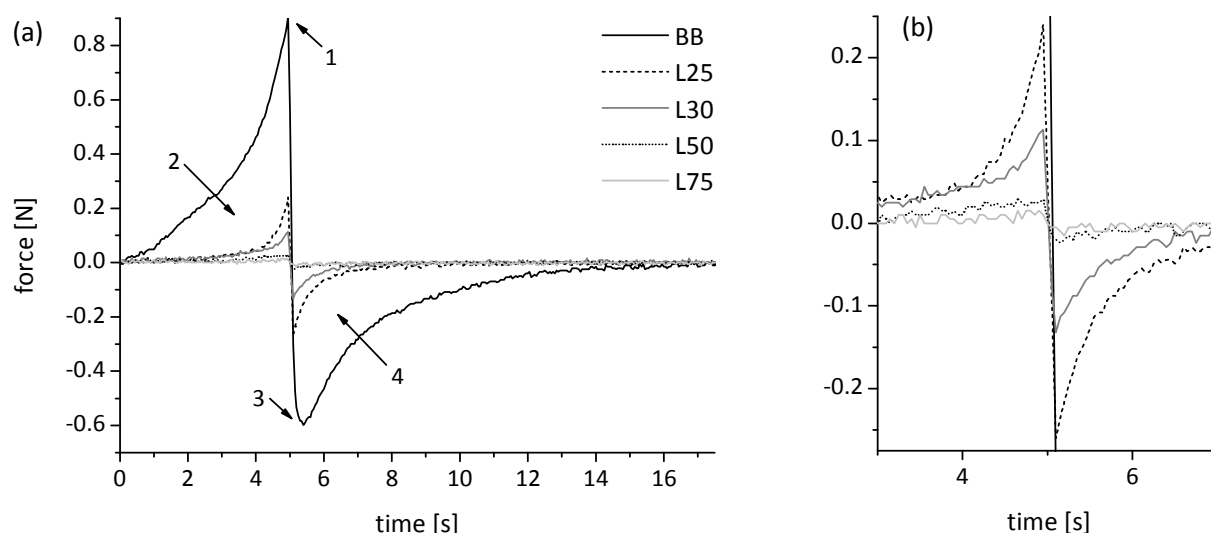


Figure 4-35. (a) Force-by-time plot through one cycle of penetration of different Lauroyl-PGA polyesters and PGA-BB to determine texture profile analysis parameters. The positive peak force 1 is the hardness of the polymer; the total positive area 2 displays the total energy required to penetrate the polymer, which is a measure of its consistency; the negative peak force 3 is the adhesive force; the total negative area 4 displays the work that is necessary to overcome attractive forces as the probe retracts and is a measure of the adhesiveness of the polymer. (b) Cut-out from the left graph to visualize the force-by-time plots of the Lauroyl-PGA polyesters, which show much smaller forces than PGA-BB.

In Figure 4-35a, it is obvious that the PGA backbone by far is the most rigid of the examined polymers. The substituted Lauroyl-PGAs exhibited much smaller deformation curves, decreasing with increasing esterification degree. This is also expressed by the calculated hardness of the polymers (Figure 4-36a). The force necessary to attain the predetermined deformation of PGA-BB was about 6 times higher than for PGA-L25 and about 50 times higher than for PGA-L75. PGA-L95 was too soft to measure, as the probe did not detect the polymer surface at the lowest possible trigger force. The effect of the esterification degree on the total work of compression showed the same dependency as the hardness and is not depicted here. These findings are in agreement with the results of the $^1\text{H-NMR}$ relaxometry study described above. With decreasing hardness in texture analysis, the T_2 relaxation time in $^1\text{H-NMR}$ relaxometry increases, indicating decreasing viscosity. The large difference between the esterified Lauroyl-PGAs and PGA-BB was, however, less pronounced in $^1\text{H-NMR}$. As already mentioned, this could be a result of the inaccuracy of T_2 values below 1 ms in the CPMG measurement [194]. Nevertheless, it was shown in both experiments that esterification of the PGA backbone with lauroyl side chains causes a rising fluidity of the polymers.

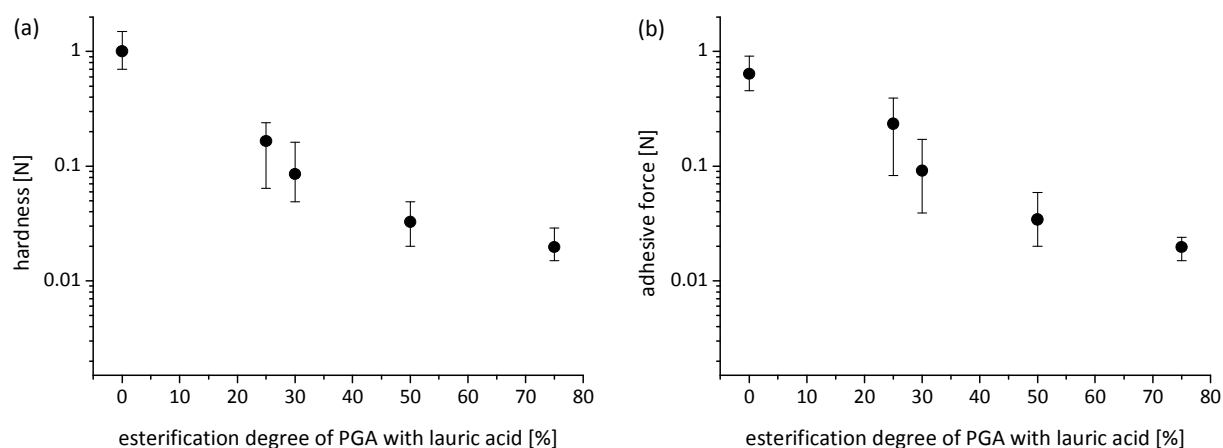


Figure 4-36. The effect of the esterification degree of Lauroyl-PGA on the hardness (a) and the adhesive force (b) of the polymers. The mean value and the range are displayed for 3-5 measurements respectively.

As also apparent in the force-time plots (Figure 4-35), the adhesive force of the polymers is considerable, displayed by the large negative peak during the withdrawal of the probe. The adhesive force (Figure 4-36b) approximately reached the same values as the hardness and the adhesiveness (not shown) exhibited similar values as the total work of compression. This sticky behavior might be a drawback for polymer handling, particularly for those with lower degree of esterification and the PGA-BB.

With the methods of $^1\text{H-NMR}$ relaxometry and texture analysis it has been shown that the degree of esterification in Lauroyl-PGA polymers considerably influences their mechanical properties. Viscosity, hardness and adhesiveness of the polymers decrease with increasing amount of esterified OH groups of the PGA backbone.

4.2.3 Spectral spatial ESR imaging of model implants

Spectral spatial ESRI gives insight into the processes going on within the implants during incubation in the buffer medium. Through the extraction of spectra from distinct slices of the image, differences inside the implant can be revealed. The specially designed sample holder with the cuboidal cavity (Figure 3-1) improved interpretability of images compared to the formerly used round containers. Due to the rectangular geometry, edge effects in the images were minimized. It was, however, still not unambiguous to definitely determine the top and bottom edge of the implants from the images. Nevertheless, one bottom slice was defined in each of the samples which served as reference for the spatial positions within the implant.

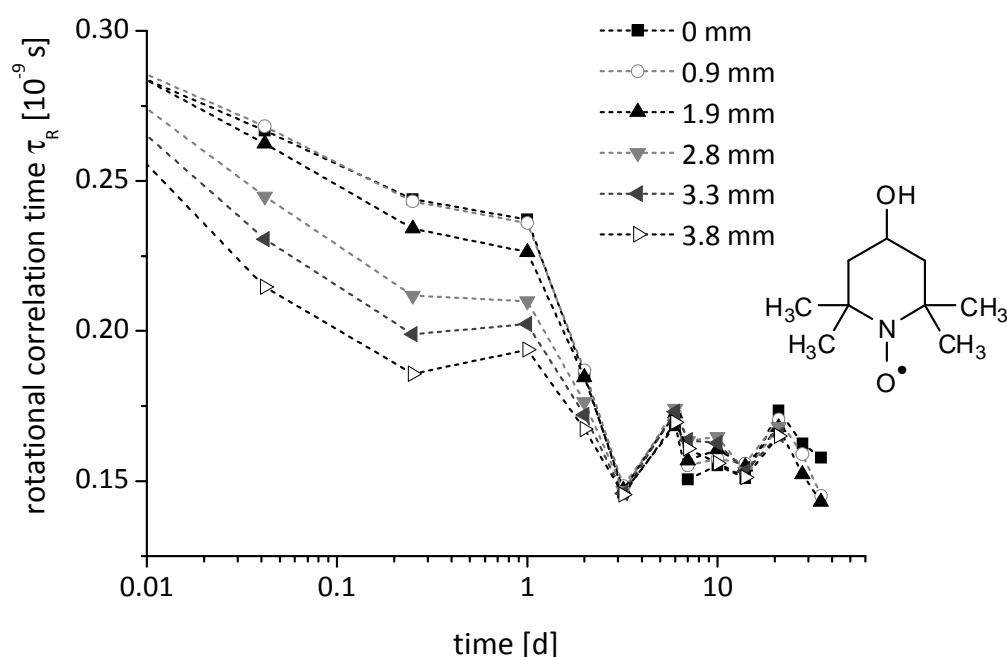


Figure 4-37. Rotational correlation times of Tempol in the different slices over time.

The rotational correlation time τ_R quantifies the state of rotational motion of a spin probe. It is the period of time after which it is not possible anymore to deduce from the present orientation of the spin label how the orientation was before this period of time [289]. τ_R is a measure of mobility and thereby of the viscosity of the local environment of the spin probe [217]. Low τ_R indicates high mobility of the spin probe and thus, in this study, most likely the contact of Tempol with penetrating buffer medium. The rotational correlation time was calculated from the parameters of the first derivative spectra as described in 3.2.3. Figure 4-37 depicts the time course of τ_R in six distinct slices of the implant. In the dry state, τ_R is quite high, owing to the limited mobility of Tempol in the dry implant. After placing the implant into the buffer medium, a rapid decay of τ_R is obvious within the first days of incubation. In the top layers, τ_R is decreasing faster than at the bottom of the implant during the first 2 d. This displays the progressing penetration of the buffer medium into the implant from top to bottom. The first drop of τ_R from the dry state to 1 h incubation which is obvious in all layers might be resulting from the temperature rise to 37 °C in the buffer medium and the concomitant decreased viscosity of the polymer. After 3 d of incubation, the rotational correlation times are similar in the different layers and the minimum values are reached. This points to a complete hydration of the implant. In the further experiment, the rotational correlation times stay on a constant level. Towards the end of the experiment, the signal-to-noise ratio gets worse because of the decreasing Tempol concentration. Therefore, the analyzation of the parameters gets more and more imprecise and the slightly fluctuating values should not be overinterpreted. After 28 d, the spectra of the 3 top layers cannot be analyzed properly anymore because of the low signal of the remaining spin probe. Comparing the final values of the rotational correlation time with the value of Tempol in pure buffer, where τ_R is about one order of magnitude lower, it is obvious that the

motion of the spin probe is still quite restricted within the implant after buffer penetration. This difference is also visible directly from the ESR spectra (Figure 4-38) when comparing the line widths. The highly mobile Tempol in pure buffer medium, gives a spectrum of three sharp lines (c) whereas the spin probe in the dry implant (a) shows a strong line broadening due to restricted motion in the highly viscous environment [290]. During the hydration of the implant, the line widths ΔB of the ESR lines continually decreased (b).

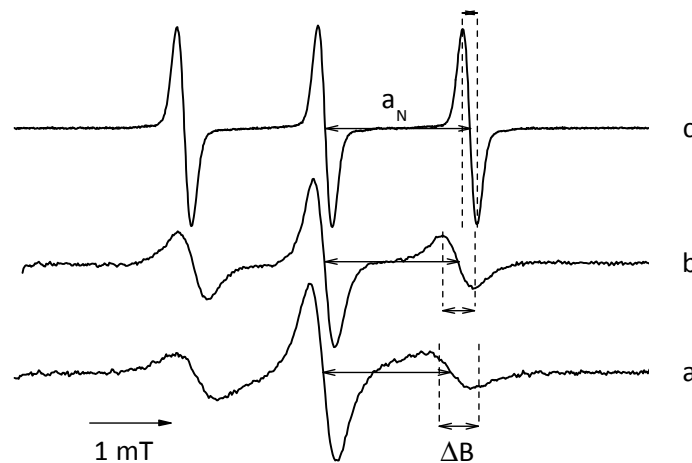


Figure 4-38. Exemplary ESR spectra of Tempol. a: Middle layer of the implant in the dry state, b: same layer after 3 d, c: pure buffer. a_N marks the hyperfine splitting, ΔB indicates the line width.

The hyperfine splitting a_N (Figure 4-38) of the lines in an ESR spectrum is another parameter that provides information about the local environment of the spin probe. The hyperfine splitting of Tempol is sensitive to the polarity of the spin probe nitroxide group environment and increases with increasing polarity [291]. For higher sensitivity, not a_N but $2a_N$, the distance between the first and third line [181] was evaluated in this study (Figure 4-39a). The top layers of the implant show a greater splitting than the bottom layers (Figure 4-39a), indicating higher polarity. This can be attributed to the surrounding buffer medium. During the first week of incubation the hyperfine splitting is steadily increasing, demonstrating the progressing hydration of the implant. This is in good accordance with the results of the rotational correlation times (Figure 4-37). After an incubation of 21 d, the hyperfine splitting was not analyzable anymore due to the poor signal-to-noise ratio.

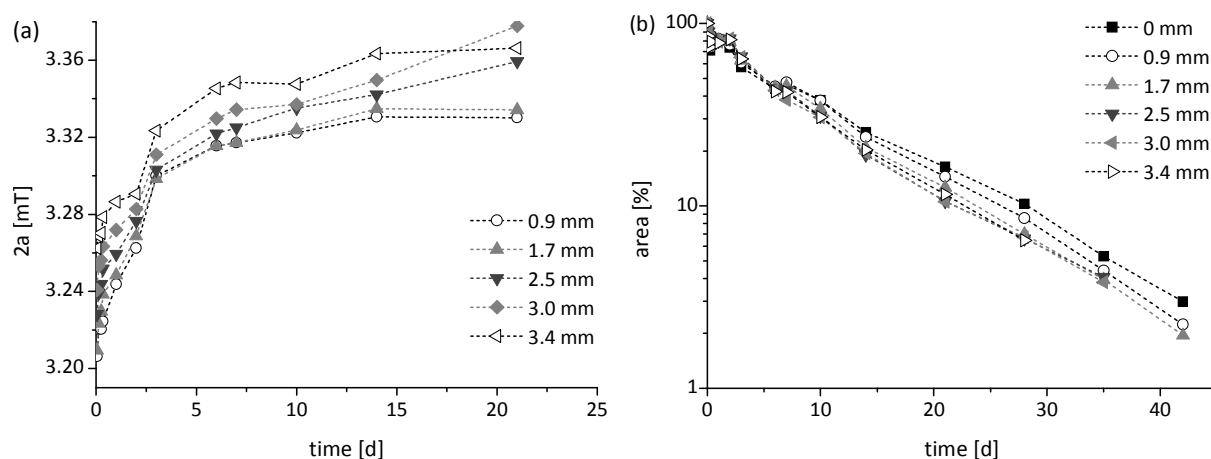


Figure 4-39. (a) Hyperfine splitting of Tempol in 5 distinct layers of the implant ($2a_N$ = splitting of low- and high-field line). (b) Release of Tempol from the different layers, determined from the areas under the ESR spectra, shown in reference to the start value of the respective layer.

The release of Tempol from the implant, determined from the areas under the ESR spectra, roughly shows first order kinetics (Figure 4-39b) with $t_{1/2}$ of about 5 d ($k_e \approx 0.14$ - 0.15 d $^{-1}$). The decrease of the signal in the top layers seems a bit faster than in the bottom layers. This phenomenon was, however, expected to be even more evident, particularly in the beginning of the release. Due to the hindered diffusion and the slower penetration of buffer, the release from the bottom of the implant should have taken more time.

The interpretation of intensity data from ESR spectra is, however, not an easy task and – at least for the release of drug delivery systems, containing water – by far an absolute method. There are various factors influencing signal intensity such as water content, sample positioning in the cavity of the ESR spectrometer, drying of the sample, heat development during the measurement, frequency fluctuations of the resonator etc. The accuracy of sample positioning was to some degree ensured by the design of the sample holder which restricted the insertion into the cavity by a special nose at the end of the holder (Figure 3-1). The drying of the sample through heating was sought to be prevented by covering the opening of the sample holder with plastic film. Nevertheless, despite all efforts to keep the measurement conditions constant, variation of room temperature, humidity and resonator frequency could still have been influencing parameters. Another influencing effect on the signal intensity is the shielding of ESR signals by water. Changing water content furthermore affects the development of heat during the measurement as the dielectric loss increases with increasing amount of water in the sample. These factors were addressed by removing excess buffer from the implant and by drying of the sample holder before each measurement. However, particularly during the first days of incubation, the water content inside the implant is naturally increasing by hydration of the polymer, leading to reduced signal intensity by the shielding effect of water. Additionally, it was just discovered recently (after this study was finished) that water may penetrate into certain slots of the sample holder, resulting

in a signal loss of about 10-20 % during the first 12 hours [292]. But not only signal loss by shielding and higher heat development but also the fact of penetrating buffer through the bottom and the sides of the sample holder, most likely falsified the presented results of this ESRI study. It should therefore be kept in mind that this is regarded as a preliminary study and the results should be considered with caution.

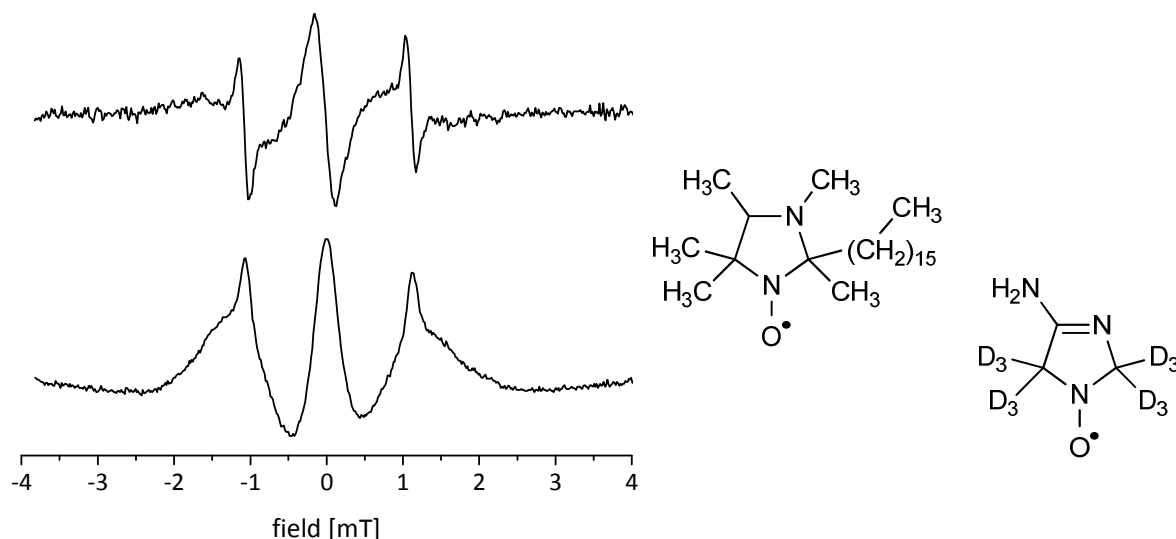


Figure 4-40. Left: Exemplary ESR signal (top: derivative, bottom: integrated), extracted from a contour plot image: the broad 3-line spectrum of ^{14}N -HD-PMI is superimposed by the 2 narrow lines of ^{15}N -AT (at about -1 and +1 mT) in PGA-L30 after 6 d of buffer exposition. Right: Chemical structures of HD-PMI and D- ^{15}N -AT.

In addition to the experiments with Tempol, the same implants were prepared with a mixture of ^{14}N -HD-PMI and D- ^{15}N -AT. Exploiting the different nuclear spins I of the two nitrogen isotopes (^{14}N $I = 1$, ^{15}N $I = 1/2$) which result in different numbers of lines in the ESR spectrum, the simultaneous study of a lipophilic and hydrophilic model drug was possible. As displayed in Figure 4-40, the two narrow lines of the deuterated ^{15}N nitroxide can be distinguished from the 3-line spectrum of the ^{14}N nitroxide.

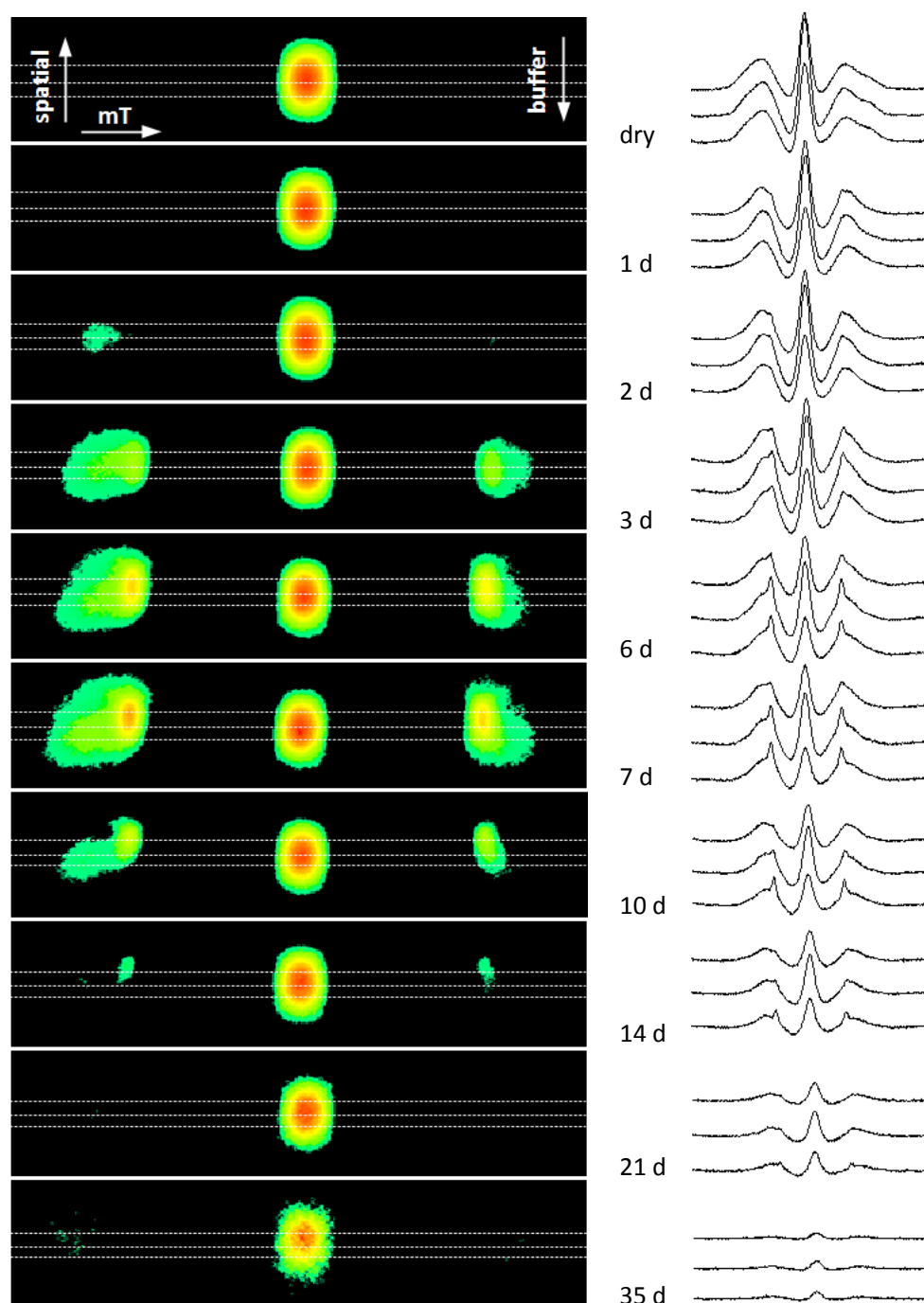



Figure 4-41. Left: Contour plots of integrated ESR spectra (the intensity increases from green via yellow through to red ; intensities < 50 % are masked. Each contour plot is scaled to its maximum amplitude; the signal-to-noise ratio gets therefore worse towards the end). Right: extracted spectra of 3 distinct slices, corresponding to the white dotted lines in the contour plots.

In the dry state of the implant, only a broad signal of HD-PMI is visible in all slices (Figure 4-41), indicating a high degree of immobilization. After 1 d exposition to the buffer medium, the first small shoulders appear in the spectra of the top layer, corresponding to the spectrum of rapidly tumbling $^{15}\text{N-AT}$. This displays the penetration of the buffer into the outer layer of the implant, solubilizing the hydrophilic spin probe. After 2 d, the $^{15}\text{N-AT}$ signal is visible in the middle of the implant and after 3 d also in the

bottom slice. Furthermore, the ^{15}N -AT lines increase and sharpen within the first week. This nicely illustrates the penetrating buffer front from outside to inside and the concomitant hydration of the implant. The signal in the top layer does not get very high at all time points, indicating a continuous release of the spin probe. After 14 d, the ^{15}N -AT lines are only obvious in the bottom layer and after 21 d there is hardly any signal left. This displays the gradual release of the hydrophilic spin probe from top to bottom. Simultaneously, the HD-PMI signal also decreases and is only very weak after 35 d.

The area under the central line of the ESR derivatives of HD-PMI over time is depicted in Figure 4-42a.

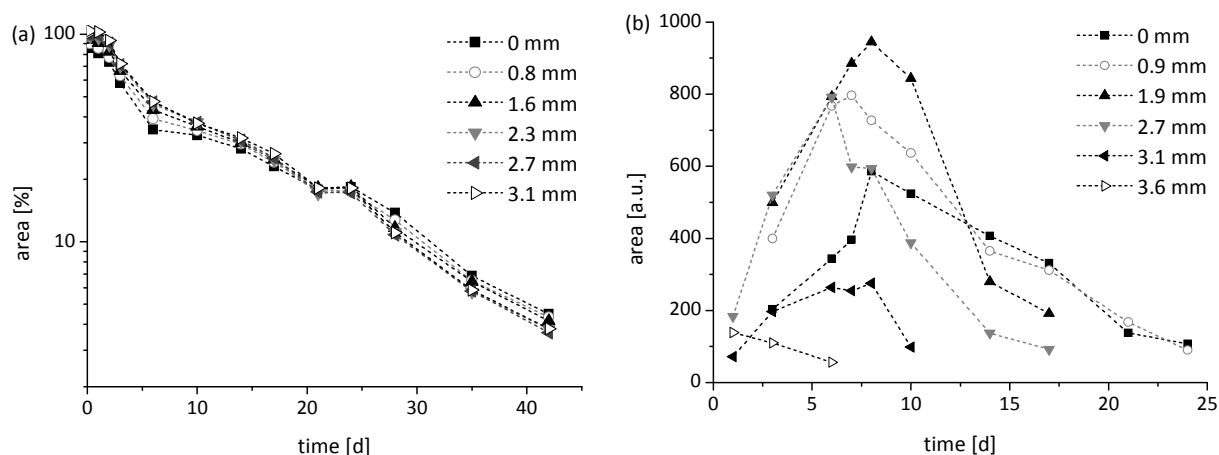


Figure 4-42. Area under (a) HD-PMI signal (calculated from the central line of the derivative) and (b) ^{15}N -AT signal over time, indicating the release of the spin probes.

The signal of the lipophilic spin probe HD-PMI showed the highest intensity in the dry implant and is almost constantly decreasing over time. The plot resembles first order kinetics with 2 phases. The release during the first week seems to be faster than afterwards. There is no relevant difference between the different layers of the implant. After 42 d, at the end of the experiment, only about 3-4 % of the HD-PMI signal was left in the implant. This indicates a gradual release of HD-PMI from the implant into the 0.01 % (w/v) surfactant containing buffer medium.

The release of ^{15}N -AT from the implant on the basis of the evaluated areas is shown in Figure 4-42b. In addition to the information from the contour plots (Figure 4-41), the analysis of the areas provides a more detailed picture on the ^{15}N -AT concentrations in the different layers of the implant. As already mentioned, the signal of ^{15}N -AT was not visible at the beginning of the incubation. Therefore, the presentation of the areas under the ^{15}N -AT lines (Figure 4-42b) is different from HD-PMI (a) where all values were normalized to the initially measured area of each layer. For ^{15}N -AT, in contrast, the absolute numbers are displayed, illustrating the measured areas in different spatial positions of the implant. The first signal appeared after 24 h in the 3 top slices, displaying the penetration of the buffer medium which solubilized the hydrophilic spin probe. The highest signals appeared after 6-8 d, followed by a constant decrease of the

area due to the release of the spin probe. The signal in the top layer gets lost in the noise after 6 d already. The release of ^{15}N -AT is slower the greater the distance from the implant surface, shown by the steepness of the signal decay. Only in the 2 bottom layers, analyzable lines of ^{15}N -AT could still be found after 24 d.

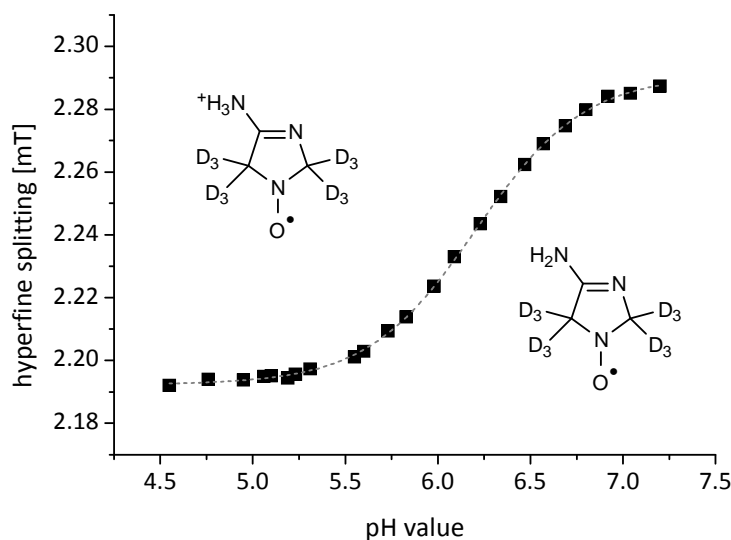


Figure 4-43. Dependency of the hyperfine splitting of D - ^{15}N -AT on the pH value of the buffer medium (pH value adjusted with 0.001 M HCl). The experimental data was fitted by a Boltzmann fit with a correlation of $R^2 = 0.9997$. The chemical structures of D - ^{15}N -AT are displayed in the respective pH environments. By protonation in the acidic milieu, the spin density at the nitroxyl nitrogen decreases which results in a decreased hyperfine splitting [293].

^{15}N -AT is a pH sensitive spin probe [196,293]. The hyperfine splitting of the two ESR lines is influenced by the pH value of the environment in the range from about pH 5 to 7.3 as shown in Figure 4-43. By means of a calibration curve, the pK_a value of the spin probe in the applied release buffer was determined as about 6.2. Based on the sigmoidal Boltzmann fit of the calibration data, the pH value of a particular layer could be calculated from the hyperfine splitting of the respective ^{15}N -AT spectrum. Thus it was possible to follow the microacidity inside the degrading implants. Figure 4-44 displays the process of the pH value over time in the different implant slices. Reliable pH values could be calculated after 3 d when enough water was penetrated into the polymer and the sharp lines of rapidly tumbling ^{15}N -AT were visible. The pH could be assessed only as long as the ^{15}N -AT signal in the layer was large enough to be analyzed.

However, the pH value is not the only parameter influencing the hyperfine splitting of the ^{15}N -AT lines. As seen for Tempol (Figure 4-39a), also the polarity of the surrounding environment is having an impact. For Tempol, it has been shown that the hyperfine splitting decreases with increasing distance from the top of the implant. This is also seen here and should therefore not be overinterpreted in terms of the pH value. In general, due to the overlay of both effects for ^{15}N -AT, the pH values shown in Figure 4-44 are not claimed to be absolute. Nevertheless, they are at least minimum values for the pH in these slices. The important result of this study is the relative stability of the pH value

which doesn't drop under 5.8 during the duration of the experiment. In comparison, for degrading PLGA implants pH values as low as pH 3 or 2 have been reported [181,182] which could be very unfavorable for the stability of incorporated proteins, peptides and small molecules [197]. Furthermore, the biocompatibility of the implant with respect to surrounding cells and tissue could be affected [182].

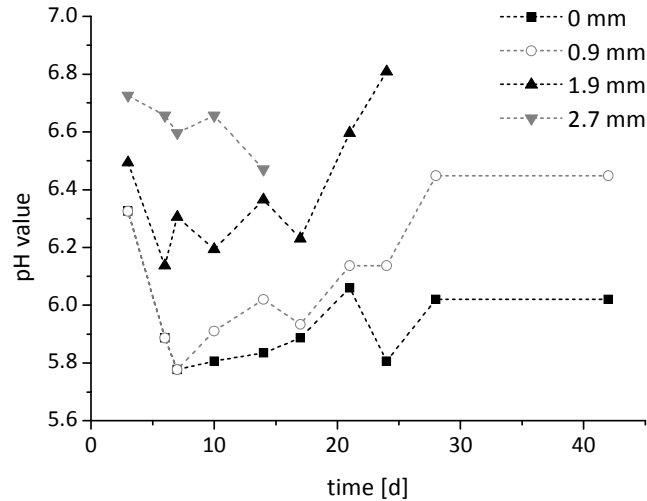


Figure 4-44. Process of the pH value in different slices of the implant over time. The pH values are calculated from the equation of the Boltzmann fit of the calibration curve (Figure 4-43).

4.2.4 *In vitro* release study by multispectral fluorescence imaging

Multispectral fluorescence imaging is a fast and powerful tool to investigate the release behavior of implants *in vitro* and *in vivo*. For the *in vitro* experiments, the lipophilic fluorescence dye DiI and the hydrophilic Rhodamine110 were included into different Lauroyl-PGA implants as model drugs.

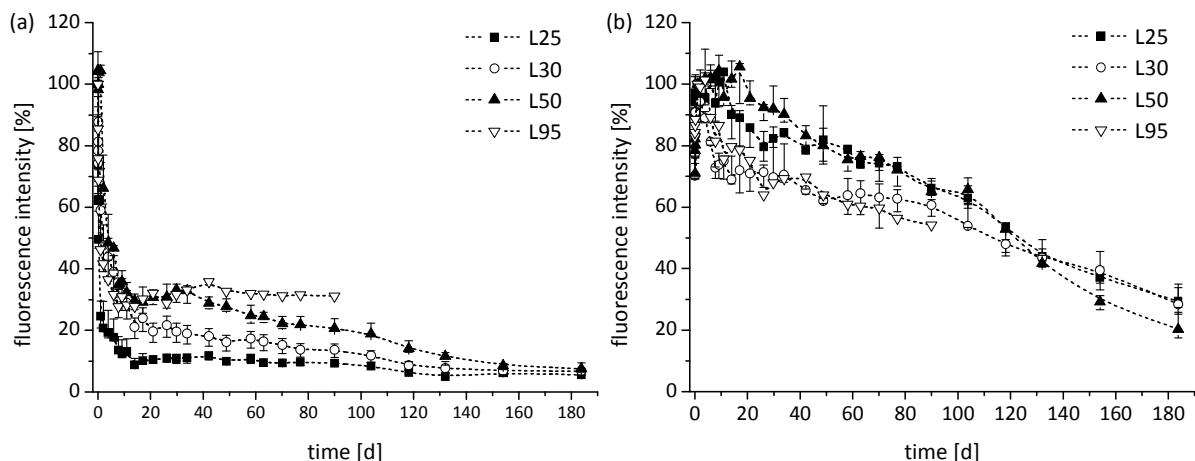


Figure 4-45. Fluorescence intensity of (a) Rhodamine110 and (b) DiI in the different Lauroyl-PGA implants over time. Median and range of 3 implant models are shown respectively. For PGA-L95 data of only one model is shown as the implants in the two other models moved and stuck to the covering PET network which falsified the results.

The fluorescence intensity of the hydrophilic dye Rhodamine110 dropped rather fast during the first week. Thereby, the speed of release from the three Lauroyl-PGA polyesters was slightly different with a dependency on the esterification degree. From PGA-L25, the polymer with the lowest amount of lauroyl chains, the fluorescence was reduced by half after 4 h already. For PGA-L30, this took about 2 d and for PGA-L50 almost 4 d. A residual content of 10 % was reached for PGA-L25 after approximately 20 d, for PGA-L30 after about 100 d and for PGA-L50 after about 140 d. Overall, Rhodamine110 was released slower from the polymers with higher esterification degree than from those with lower degree of lauroyl side chains. The data of one PGA-L95 implant followed this tendency but is not representative. Due to the low viscosity of this polymer, two of the implants and also the third after some time, moved to one side of the container and stuck to the covering PET network, so the analysis of the fluorescence data was falsified.

In comparison to the hydrophilic Rhodamine110, the lipophilic dye DiI was released very slowly from all of the implants (Figure 4-45b). It took about 4 months until the intensity reached half the initial values. After some fluctuations in the first week, the fluorescence intensity decreased almost linearly until at the end of the experiment after 6 months about 20-30 % of the dye were still remaining. An explicit dependency of the release of DiI on the esterification degree of the polymer could not be detected.

4.2.5 *In vivo* release study by multispectral fluorescence imaging

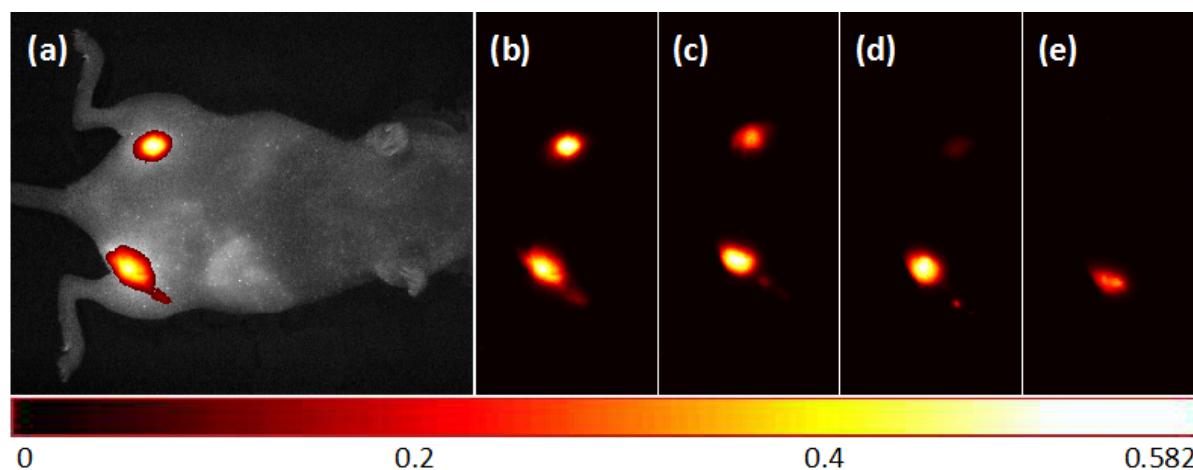


Figure 4-46. Fluorescence images of one mouse carrying a PGA-L25 implant on the left thigh (bottom) and a PGA-L95 implant on the right thigh (top). The pictures b-e show the fluorescence after 1 day, 2 weeks, 4 weeks and 5 months.

For the preliminary *in vivo* study, DiI was incorporated as a lipophilic model drug in the two polymers with the most different properties, PGA-L25 and PGA-L95. A reliable *in vivo* monitoring of the hydrophilic dye Rhodamine110 would not have been possible as the mouse body shows high absorption and autofluorescence in the blue wavelength range [115,294] which is used to detect this dye. Furthermore is the penetration depth of blue light into tissue very limited due to the relatively short wavelength [259,260].

The primary result of this study was the much faster degradation of PGA-L95 compared to PGA-L25 as it can be followed by the decrease of the fluorescence signal in Figure 4-46. In view of the only slight differences of DiI release in the *in vitro* study (Figure 4-45b), the faster signal fate of PGA-L95 can be mainly attributed to faster polymer degradation rather than only faster release of the dye. Whereas for the PGA-L25 implants at least 30 % of the initial intensity was measured after 6 months (Figure 4-47b), the intensity of the PGA-L95 implants dropped by half after 2 weeks (Figure 4-47a). After 7 weeks, only a marginal fluorescence intensity of about 5 % could be detected for PGA-L95.

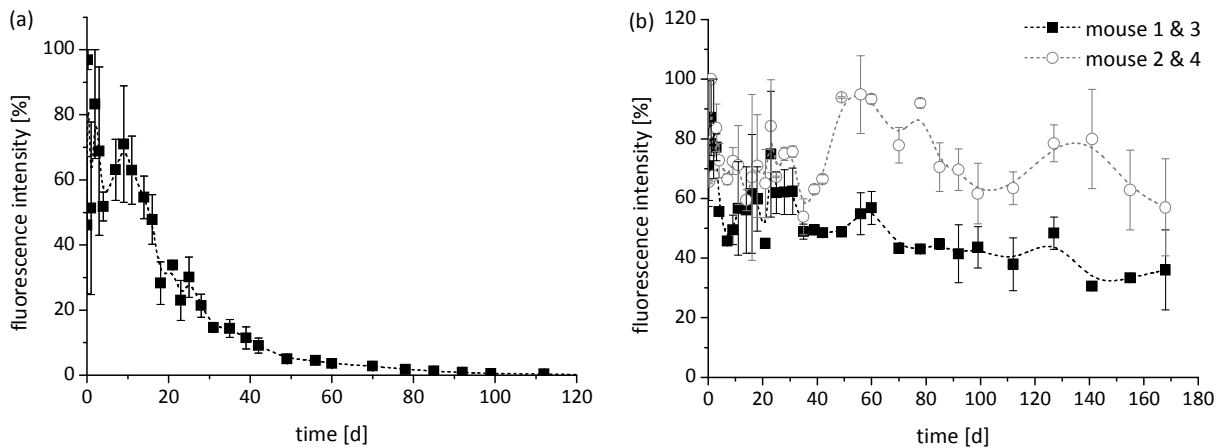


Figure 4-47. (a) Fluorescence intensity of DiI in PGA-L95 implants. The average value and the range of two mice are shown. (b) Fluorescence intensity of DiI in PGA-L25 implants. Each line shows the data of two mice. The solid line displays the data of two mice with good compatibility and the dashed line depicts the data of two mice with slight irritations (elevations over the location of the implant).

The data of the two mice with PGA-L95 implants was in good accordance with each other and the implants were well tolerated. No indications for inflammation or edema have been detected. The PGA-L25 implants were also well tolerated by two of the mice (mouse 1 & 3) but the two others (mouse 2 & 4) showed slight elevations of the skin over the location of the implants after about 40-50 d. This difference is also reflected by the fluorescence data (Figure 4-47b) where the values for mice 2 & 4 steeply increased after about 45 d and stayed on a high level during the whole experiment. The elevations subsided afterwards but were visible again after 127 d, especially in mouse 2. The tensioning of the skin brought the implants closer to the camera which might be the reason for the subsequent high fluorescence intensities in these mice. After 141 d, mouse 2 showed a small bite wound in the skin over the implant which resulted in a very high signal, displayed by the top of the error bar.

The elevations of the skin could be an indication of slight edema, developed around the implants. This could be caused by irritation and inflammation of the surrounding tissue or by an increased water attraction of the implant [295] or by a combination of both. The continuously high signals in these mice could be an indication for a fibroblastic reaction, leading to encapsulation of the implant by connective tissue as often observed

for solid implants and injectable biomaterials [296,297]. This capsule, as an additional barrier, could hinder the further degradation of the implant and the release of the dye [298]. Why two of the mice did show signs of irritation and two did not, could not be elucidated in this study. Tissue response towards implants is influenced by many factors including the extent of injury by the needle, the loss of basement membrane structures, the extent of inflammatory reaction, the degree of cellular necrosis, etc. [299], all of which can be different for the individual mice. Apart from that, all mice stayed healthy during the whole period of the study without any loss of weight or other pathological signs.

It should be mentioned that it is generally a challenge for *in vivo* imaging to place the mice in the same position for every measurement. Slight variations in handling as well as changes of the mouse body itself can influence the results of the measured fluorescence intensity unintentionally which can result in high variance of the measured signals.

The huge difference in signal fate of PGA-L25 and PGA-L95 implants suggested a faster degradation of the PGA-L95 implants *in vivo*. This seemed surprising at first glance as faster degradation was expected for PGA-L25 due to its higher hydrophilicity. Given that polyesters degrade mainly via hydrolysis, the reaction velocity is influenced by water accessibility to the ester bonds [300-302]. As lipophilic polymers in contrast to hydrophilic ones can only take up small quantities of water, the velocity of degradation is usually decreased [11,301]. It was therefore presumed prior to the study that the more lipophilic PGA-L95 would degrade slower than PGA-L25. However, the uptake of water is not the only factor influencing polymer degradation *in vivo*. It has also been reported that other polymer properties, in particular viscosity, are influencing factors for encapsulation and *in vivo* degradation [299,303], e.g. by enzymes. Polyester implants with higher fluidity might be accessed more easily by esterases than rigid ones. Furthermore, it is assumed that softer implants with lower viscosity tend to be better accepted than solid implants which stimulate encapsulation reactions by high mechanical resistance to the surrounding tissue [303]. As the T_2 relaxation time of PGA-L25 is about one order of magnitude lower (see 4.2.1) – indicating higher viscosity – and its hardness, measured by texture analysis, about one order of magnitude higher (see 4.2.2) compared to PGA-L95, this could be a possible explanation for the slower degradation and adverse tissue effects.

4.2.6 *Ex vivo* investigation of implants by confocal laser scanning microscopy

To examine the remaining size and structure of the implants at the end of the study, the four mice have been sacrificed and autopsied after 6 months. No remains of the PGA-L95 implants could be found after this period of time. The residual parts of the PGA-L25 implants, however, could be dissected; some of them were subcutaneously disintegrated into small fractions. Most pieces were easily relocatable and removable. Some of the larger remnants, especially those of mice 2 & 4, were surrounded by a thin membrane

which could be appearance of a fine capsule of connective tissue. This points to a normal mild foreign body reaction which was reported for many other biocompatible implants before [296,303,304]. This finding supported the above mentioned considerations of implant encapsulation hindering polymer degradation and drug release.

The remaining implant of mouse 2 which was adhering to surrounding dermal tissue was investigated by confocal microscopy (Figure 4-48). The micrographs indicate ingrowth of connective tissue into the implant. There is, however, no evidence that a substantial inflammation had taken place.

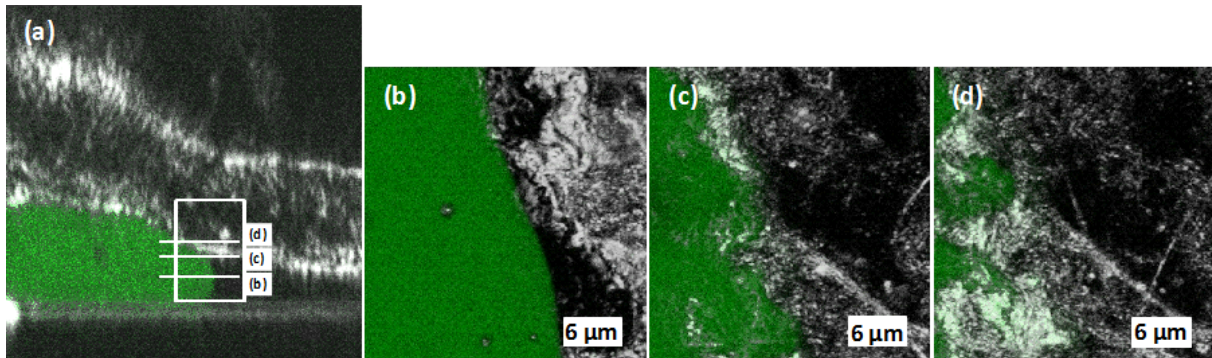


Figure 4-48. Ex vivo micrograph (a) of a PGA-L25 implant (green fluorescence) at the contact area with the surrounding dermal tissue (marked with white box). The 3 lines indicate distinct layers of a confocal z-stack series which are displayed in the 3 details (b-d), from bottom to top.





More detailed investigation of the biocompatibility of PGA based implants should include sectioning and histological staining of the implants together with adjacent tissue at various time points after injection. Only a closer look to the different stages of tissue response and the precise determination of involved cells can provide a reliable picture of biocompatibility.

5 Summary and perspectives

Poly(glycerol adipate) is an interesting biodegradable polymer with great potential for the application in various drug delivery systems. The free pendant hydroxyl group of the PGA backbone provides the possibility for versatile modification and thus flexible adjustment of its properties. By esterification of the hydroxyl groups with different fatty acids, promising amphiphilic polymers with a wide range of characteristics could be obtained.

The major part of this work reports about the preparation and comprehensive characterization of nanoparticulate drug carriers from fatty acid modified PGA. Based on the optimization of the interfacial deposition method, self-stabilizing Lauroyl-, Stearoyl-, Oleoyl- and Behenoyl-PGA nanoparticles with defined sizes and narrow size distributions could be prepared. Their characteristics have been intensely studied and it has been shown that the chain length of the attached fatty acids as well as their esterification degree substantially influence the physicochemical properties of bulk polymers and nanoparticles. Driven by nanophase separation between the polymer backbone and domains formed by the fatty acid side chains, diverse nanostructured polymeric aggregates were obtained which was demonstrated by TEM and XRD. The grafting density and the corresponding volume fraction of the alkyl chains strongly influenced the aggregation of the polymer in water and thus the nature of the resulting colloidal system (Table 5-1).

Table 5-1. Influence of esterification degree on polymer aggregation.

Substitution degree	zero	low	medium	high
polymer structure				
expected structures in water	swollen PGA chains	PGA network with spherical alkyl domains as cross-links	cylindrical/elongated domains	lamellar domains

Contrary to existing literature [24], different TEM techniques revealed that not only spherical particles were formed, as it is typical for esterification degrees over 50 %. Furthermore, non-spherical particles with well-defined geometries could be prepared by Stearoyl-PGAs with lower esterification degrees, which was not known before. By AF4/MALLS measurements combined with PCS, additional shape information regarding the third dimension of the particles was gained. SAXS and WAXS measurements gave deep insight into the inner architecture of various PGA based nanoparticles and also revealed differences as a result of the grafting density. On the basis of these findings, two

structural models were created, suggesting the different architectures inside the nanoparticles.

The diverse shapes and structures could qualify the formulations for different applications and incorporation strategies. As it is known that geometry, surface properties and internal structures might substantially influence drug incorporation and *in vivo* behavior, a thorough investigation of shape and structure is absolutely vital for the rational design of nanoparticulate drug carriers.

Not only structural diversity of PGA based nanoparticles could be detected but also other characteristics, such as aggregate state, degree of crystallinity, thermal behavior and polarity were variable in different formulations. These properties can be tailored by varying parameters like esterification degree, length of side chains and use of unsaturated fatty acids. Another possible variation could be the use of another dicarboxylic acid for polycondensation with glycerol in the synthesis of the polymer backbone. This toolbox provides the flexibility to adjust the PGA delivery systems according to the requirements of various drug molecules and applications. This is a major advantage over most other polymeric systems as well as SLNs. Furthermore, compared to SLNs, which are reported as quite promising carriers for lipophilic drugs, the absence of any emulsifier or stabilizer and the lower degree of crystallinity are advantageous. The studied PGA based polyesters form intermediate systems, somewhere in between highly ordered crystals and viscous emulsions which is favorable for both drug protection and incorporation.

For the determination of drug loading capacity, an own procedure has been developed and an exemplary study was conducted with PGA-S65 nanoparticles. For these nanoparticles, drug loads up to 1 % of the highly lipophilic fluorescent dye DiI and 10 % of the lipophilic THPP were observed which are quite high values compared to other polymeric nanoparticles or SLNs [74,258]. This was, however, only a pilot study which needs to be extended to the other PGA based particles and to other drugs to get a better picture of the different possible applications.

In the next step towards *in vivo* experiments, cell compatibility studies were carried out in which different PGA based nanoparticles were tested with respect to hemolysis of red blood cells as well as their influence on metabolic activity and growth of HepG2 cells. It was shown that nanoparticles of Stearoyl-PGA with medium and higher degrees of esterified hydroxyl groups as well as those of the PGA backbone do not show any hemolytic activity up to a concentration of 10 mg/ml. For PGA-S20 nanoparticles in high concentrations, however, considerable hemolysis was detected which could be reduced by the addition of Poloxamer 188. All tested PGA based nanoparticles were nontoxic for HepG2 cells. Stearoyl-PGA particles rather increased cell activity and proliferation which can be most likely ascribed to the metabolization of their stearic acid fractions by the cells.

On the basis of these promising results, a preliminary *in vivo* experiment in healthy mice was carried out with DiR loaded PGA-S65 nanoparticles in order to get information

about body distribution and fate of the nanoparticles after i.v. application. In view of the relatively fast clearance – which is typically observed for hydrophobic nanoparticles – strategies for prolonged circulation have been considered. In cooperation with the IMC in Prague, PGA-S65 nanoparticles have been coated with HPMA copolymers by physical attachment as well as covalent bonding. By use of two different fluorescent dyes – Dy676 was labeled to the HPMA copolymer and DiR was loaded on the nanoparticles – simultaneous tracking of coating polymer and particles was possible *in vivo*. The results of the *in vivo* study showed that the physical coating with the HPMA copolymer was beneficial to protect PGA-S65 nanoparticles from rapid uptake by the MPS and thus to prolong their circulation time in healthy and even more in tumor-bearing mice. Unexpectedly, the effect of the covalently coated nanoparticles, in comparison, was less efficient in both groups. This could be afterwards explained by an incomplete coating reaction. All studied nanoparticle samples showed high fluorescence signals in the liver. Particularly for the uncoated particles, considerable intensity was additionally detected in the bone regions. This phenomenon was further investigated and confirmed by an *in vitro* assay in which PGA-S65 nanoparticles were bound by hydroxylapatite. When the mechanism of this affinity could be elucidated and the polymer appropriately modified, PGA might be an interesting material for the application in bone targeting.

For the coated samples, Dy676 signal was observed in the bladder of the healthy mice, revealing that the attachment of HPMA copolymers was not quantitative. This indication was later verified *in vitro* by VIS spectrophotometry after gel filtration. The samples injected in the tumor-bearing mice were therefore purified again by ultrafiltration, which, however, did not completely eliminate the bladder signal.

Apart from that, a successive accumulation of the fluorescence signal in the xenograft HT29 tumor was detected for the coated nanoparticles over time; again a higher benefit was achieved with the physical coating. Why especially the Dy676 signal was visible in the tumor region – also expressed by increased tumor accumulation values (TAV) compared to DiR – is comprehensively discussed in this work. A number of explanatory approaches have been proposed which can, however, only be enlightened by further *in vitro* and *in vivo* investigations. Some important questions for future work would be: Why is there still free unbound coating polymer present in the sample after ultrafiltration? Is there a partial detachment of the physical coating *in vivo*? Are the nanoparticles destabilized in the bloodstream and is DiR released? What impact does the different penetration depth of red and NIR light have on the intensity results?

Ex vivo autopsy confirmed the *in vivo* observed body distribution and tumor accumulation of Dy676. Additionally, relatively high Dy676 signals were found in the adrenal glands and the ovaries. For the covalently coated sample, also an accumulation in the kidneys was observed. The reasons of these findings are still a matter of speculation and could be only partly elucidated by literature review. It was, however, remarkable that several nanoparticle studies were found in literature where quite high signals in these organs have been reported without paying further attention to it. The

issues of nanoparticle accumulation in ovaries together with the possible diffusion of DiR out of nanoparticles *in vivo* are currently highly topical and still under investigation in our laboratory.

Nevertheless, the results of the *in vivo* study demonstrate that the coating of PGA based nanoparticles could retard body fate and enhance tumor accumulation. Certainly, the HPMA copolymer coating requires further improvement to achieve a quantitative and strong attachment. Regarding the physical coating, HPMA copolymer with higher content of cholesterol or with stearate chains instead of cholesterol might be beneficial to strengthen the hydrophobic interaction between the amphiphilic HPMA copolymer and the nanoparticles. However, the question of detachment *in vivo* would always be open for any physically attached coating. Therefore, the covalent coating reaction should be studied in more detail to reveal the reasons of the incomplete process and achieve quantitative conversion. A possible approach for the optimization of this reaction might be the introduction of groups designed for copper-free click-chemistry in the PGA backbone prior to nanoparticle preparation. In particular, dibenzylcyclooctyne (DBCO) moieties could be introduced on hydroxyl groups of PGA where afterwards the HPMA copolymer, bearing azide groups, could be clicked. Another approach could be the coupling of an HPMA copolymer to a fatty acid modified PGA polyester in an organic solvent, followed by the preparation of nanoparticles from this block/graft copolymer. And certainly, there is room for many other coating approaches, including HPMA copolymers as well as other hydrophilic macromolecules.

Since the *in vivo* distribution study as well as the HPMA coating was only carried out with solid spherical PGA-S65 nanoparticles, it would be interesting to study and compare also the behavior of the viscous particles and the particles with different shapes. Thereby it could be investigated if these characteristics actually influence the distribution pattern and the extravasation in tumor tissue.

In the second part of this work the use of viscous Lauroyl-PGAs as implants for sustained drug release is reported. This application of PGA was completely new ground, entered in this study. In comparison to currently used market products, viscous Lauroyl-PGA combines several advantages, qualifying it as a promising implant material. Due to its biodegradability, it does not have to be removed after the treatment period, as necessary for some RCM implants composed of non-biodegradable polymers. Furthermore, it can be injected by standard needles which increases patient compliance compared to solid preformed implant systems. An advantage over *in situ* forming implants – which also comply with the above mentioned benefits – is the possible injection without the addition of organic solvents or with only $\leq 5\%$ of NMP. Moreover, in contrast to the widely used PLA or PLGA, the pH value inside the implant does not drop into highly acidic regions during polymer degradation, at least during the measurement period of 40 d.

The methods of $^1\text{H-NMR}$ relaxometry and texture analysis provided information about the viscosity and the mechanical properties of the polymers and the influence of their

esterification degree. Lauroyl-PGAs with higher grafting density revealed lower viscosity, hardness and adhesiveness which enable them to be mixed and injected more easily. An *in vitro* study of four Lauroyl-PGAs displayed a rather fast release of the hydrophilic dye Rhodamine110 with half-lives from 4 h to about 4 d, increasing for higher esterification degrees. The lipophilic DiI, in contrast, was released very slowly with only slight differences between the polymers and a half-life of about 4 months. The different release rates of the hydrophilic substance and the relatively constant slow release of the lipophilic dye indicates a broad range of possible applications for the sustained release of drugs by these polymers.

By ESRI it was possible to monitor the progress of buffer penetration inside the implant. It was shown that in a one side open container it took about 3 d until all parts of the PGA-L30 implants had been hydrated. Full hydration with an equilibrium state seemed to be reached after about 6 d. The release of the hydrophilic spin probe Tempol from PGA-L30 roughly showed first order kinetics with a half-life of about 5 d. By means of the pH-sensitive nitroxide ¹⁵N-AT, not only water penetration and spin probe release but also the pH value in different layers of the implant could be assessed non-invasively over time. With the fact that the pH inside the implant did not drop under about 5.7, this polymer could be an appropriate alternative for the incorporation of acid-labile small drugs and therapeutic peptides or proteins.

In a small *in vivo* study, conducted with four mice, PGA-L95 was degraded much faster than PGA-L25 which was presumed to be a result of its softer characteristics. PGA-L95 was well tolerated and completely degraded subcutaneously. The half-life of the monitored fluorescence intensity of the lipophilic DiI was about 2 weeks. In contrast, the fluorescence signal of the PGA-L25 implants still amounted to about 30 % at the end of the study after 6 months. Two mice out of four showed slight irritation reactions towards PGA-L25 implants and fine fibrous capsules were detected after autopsy surrounding some of the remaining PGA-L25 pieces. However, the remnants were easily relocatable and no evidence of a stronger inflammation could be found.

This very different degradation behavior for the two polymers *in vivo* indicates a high flexibility of the desired treatment period, tailored by the esterification degree. Certainly, this has to be confirmed in a larger study with other Lauroyl-PGAs. To increase the variation spectrum, the also viscous Oleoyl-PGAs could be investigated for this application as well. Thereby, it should be kept in mind that oleic acid is known to be a skin penetration enhancer with modulating effects on the stratum corneum [305,306]. If these characteristics are also relevant in a subcutaneous environment needs to be elucidated in a detailed biocompatibility study. In general, the biocompatibility of PGA based implants requires further investigation with detailed histologic staining and analysis of the involved cells after various time points. This is the only way to get a true picture of the tissue reaction towards the foreign material.

Overall it has been shown that PGA offers an interesting toolbox for the preparation of various biodegradable materials. In order to tailor their properties, not only different

fatty acids with different grafting densities can be used but also other side groups might be attached to the free hydroxyl groups. Even the coupling of active substances to the polymer backbone could be an attractive alternative. The wide range of applications in drug delivery – from nanoparticles to implants – is very promising just as many of the *in vitro* and *in vivo* results of this study. Yet, there are still some remaining questions to be answered. The suggested explanatory approaches and further ideas give impetus to deeper investigation and further development of PGA based polymers and delivery systems which is certainly both necessary and worthwhile.

6 References

- [1] A.S. Hoffman, The origins and evolution of "controlled" drug delivery systems, *J. Controlled Release*, 132 (2008) 153-163.
- [2] D.A. Wood, Biodegradable drug delivery systems, *Int. J. Pharm.*, 7 (1980) 1-18.
- [3] G.A. Boswell, Polylactide-drug mixtures, US Patent 3,773,919 (1973)
- [4] F.G. Hutchinson and B.J.A. Furr, Biodegradable polymer systems for the sustained release of polypeptides, *J. Controlled Release*, 13 (1990) 279-294.
- [5] J.S. Chawla and M.M. Amiji, Biodegradable poly(ϵ -caprolactone) nanoparticles for tumor-targeted delivery of tamoxifen, *Int. J. Pharm.*, 249 (2002) 127-138.
- [6] C.G. Pitt et al., Sustained drug delivery systems II: Factors affecting release rates from poly(ϵ -caprolactone) and related biodegradable polyesters, *J. Pharm. Sci.*, 68 (1979) 1534-1538.
- [7] J. Heller et al., Release of norethindrone from poly(ortho esters), *Polym. Eng. Sci.*, 21 (1981) 727-731.
- [8] D.N. Nguyen et al., Enhancement of poly(orthoester) microspheres for DNA vaccine delivery by blending with poly(ethylenimine), *Biomaterials*, 29 (2008) 2783-2793.
- [9] N. Kumar et al., Polyanhydrides: an overview, *Adv. Drug Delivery Rev.*, 54 (2002) 889-910.
- [10] K. Mäder et al., In Vitro/In Vivo Comparison of Drug Release and Polymer Erosion from Biodegradable P(FAD-SA) Polyanhydrides – A Noninvasive Approach by the Combined Use of Electron Paramagnetic Resonance Spectroscopy and Nuclear Magnetic Resonance Imaging, *Pharm. Res.*, 14 (1997) 820-826.
- [11] K.W. Leong et al., Bioerodible polyanhydrides as drug-carrier matrices. I: Characterization, degradation, and release characteristics, *J. Biomed. Mater. Res.*, 19 (1985) 941-955.
- [12] A. Okamura et al., Synthesis and properties of novel biodegradable polyamides containing α -amino acids, *Polymer*, 43 (2002) 3549-3554.
- [13] E. Jabbari and M. Khakpour, Morphology of and release behavior from porous polyurethane microspheres, *Biomaterials*, 21 (2000) 2073-2079.
- [14] H.R. Allcock et al., Poly[(amino acid ester)phosphazenes] as substrates for the controlled release of small molecules, *Biomaterials*, 15 (1994) 563-569.
- [15] O. Felt et al., Chitosan: A Unique Polysaccharide for Drug Delivery, *Drug Dev. Ind. Pharm.*, 24 (1998) 979-993.
- [16] E. Khor and L.Y. Lim, Implantable applications of chitin and chitosan, *Biomaterials*, 24 (2003) 2339-2349.
- [17] K.L. Douglas and M. Tabrizian, Effect of experimental parameters on the formation of alginate-chitosan nanoparticles and evaluation of their potential application as DNA carrier, *J. Biomater. Sci., Polym. Ed.*, 16 (2005) 43-56.
- [18] M. González Ferreiro et al., Characterization of alginate/poly-l-lysine particles as antisense oligonucleotide carriers, *Int. J. Pharm.*, 239 (2002) 47-59.
- [19] F. Kreye et al., Lipid implants as drug delivery systems, *Expert Opin. Drug Deliv.*, 5 (2008) 291-307.
- [20] S. Schulze and G. Winter, Lipid extrudates as novel sustained release systems for pharmaceutical proteins, *J. Controlled Release*, 134 (2009) 177-185.
- [21] P.Y. Wang, Lipids as excipient in sustained release insulin implants, *Int. J. Pharm.*, 54 (1989) 223-230.
- [22] R.H. Müller et al., Solid lipid nanoparticles (SLN) for controlled drug delivery - a review of the state of the art, *Eur. J. Pharm. Biopharm.*, 50 (2000) 161-177.
- [23] H. Bunjes, Lipid nanoparticles for the delivery of poorly water-soluble drugs, *J. Pharm. Pharmacol.*, 62 (2010) 1637-1645.
- [24] P. Kallinteri et al., Novel functionalized biodegradable polymers for nanoparticle drug delivery systems, *Biomacromolecules*, 6 (2005) 1885-1894.
- [25] H. Frey and R. Haag, Dendritic polyglycerol: a new versatile biocompatible material, *Rev. Mol. Biotechnol.*, 90 (2002) 257-267.
- [26] K. Strebhardt and A. Ullrich, Paul Ehrlich's magic bullet concept: 100 years of progress, *Nat. Rev. Cancer*, 8 (2008) 473-480.
- [27] H. Ringsdorf, Structure and properties of pharmacologically active polymers, *Journal of Polymer Science: Polymer Symposia*, 51 (1975) 135-153.
- [28] F. Marcucci and F. Lefoulon, Active targeting with particulate drug carriers in tumor therapy: fundamentals and recent progress, *Drug Discov. Today*, 9 (2004) 219-228.

- [29] H. Maeda, The tumor blood vessel as an ideal target for macromolecular anticancer agents, *J. Controlled Release*, 19 (1992) 315-324.
- [30] H. Maeda et al., Tumor vascular permeability and the EPR effect in macromolecular therapeutics: a review, *J. Controlled Release*, 65 (2000) 271-284.
- [31] K. Iwai et al., Use of oily contrast medium for selective drug targeting to tumor: enhanced therapeutic effect and X-ray image, *Cancer Res.*, 44 (1984) 2115-2121.
- [32] Y. Matsumura and H. Maeda, A New Concept for Macromolecular Therapeutics in Cancer Chemotherapy: Mechanism of Tumor-tropic Accumulation of Proteins and the Antitumor Agent Smancs, *Cancer Res.*, 46 (1986) 6387-6392.
- [33] H. Maeda, The enhanced permeability and retention (EPR) effect in tumor vasculature: the key role of tumor-selective macromolecular drug targeting, *Adv. Enzyme Regul.*, 41 (2001) 189-207.
- [34] I. Brigger et al., Nanoparticles in cancer therapy and diagnosis, *Adv. Drug Delivery Rev.*, 54 (2002) 631-651.
- [35] J. Davda and V. Labhasetwar, Characterization of nanoparticle uptake by endothelial cells, *Int. J. Pharm.*, 233 (2002) 51-59.
- [36] P. Decuzzi et al., Adhesion of microfabricated particles on vascular endothelium: a parametric analysis, *Ann. Biomed. Eng.*, 32 (2004) 793-802.
- [37] P. Decuzzi et al., Intravascular delivery of particulate systems: does geometry really matter?, *Pharm. Res.*, 26 (2009) 235-243.
- [38] J. Kopecek, Polymer–drug conjugates: Origins, progress to date and future directions, *Adv. Drug Delivery Rev.*, 65 (2013) 49-59.
- [39] R. Duncan, The dawning era of polymer therapeutics, *Nat. Rev. Drug Discovery*, 2 (2003) 347.
- [40] R. Haag and F. Kratz, Polymer therapeutics: concepts and applications, *Angew. Chem., Int. Ed.*, 45 (2006) 1198-1215.
- [41] J. Khandare et al., Multifunctional dendritic polymers in nanomedicine: opportunities and challenges, *Chemical Society Reviews*, 41 (2012) 2824-2848.
- [42] E.R. Gillies and J.M.J. Fréchet, Dendrimers and dendritic polymers in drug delivery, *Drug Discov. Today*, 10 (2005) 35-43.
- [43] K. Kataoka et al., Block copolymer micelles for drug delivery: Design, characterization and biological significance, *Adv. Drug Delivery Rev.*, 64, Supplement (2012) 37-48.
- [44] V.P. Torchilin, Micellar nanocarriers: pharmaceutical perspectives, *Pharm. Res.*, 24 (2007) 1-16.
- [45] M.C. Jones and J.C. Leroux, Polymeric micelles – a new generation of colloidal drug carriers, *Eur. J. Pharm. Biopharm.*, 48 (1999) 101-111.
- [46] A. Supersaxo et al., Mixed micelles as a proliposomal, lymphotropic drug carrier, *Pharm. Res.*, 8 (1991) 1286-1291.
- [47] A. Krishnadas et al., Sterically Stabilized Phospholipid Mixed Micelles: In Vitro Evaluation as a Novel Carrier for Water-Insoluble Drugs, *Pharm. Res.*, 20 (2003) 297-302.
- [48] A.B.E. Attia et al., Mixed micelles self-assembled from block copolymers for drug delivery, *Curr. Opin. Colloid Interface Sci.*, 16 (2011) 182-194.
- [49] G. Storm and D.J.A. Crommelin, Liposomes: quo vadis?, *Pharm. Sci. Technol. Today*, 1 (1998) 19-31.
- [50] D.C. Drummond et al., Optimizing liposomes for delivery of chemotherapeutic agents to solid tumors, *Pharmacol. Rev.*, 51 (1999) 691-744.
- [51] V.P. Torchilin, Recent advances with liposomes as pharmaceutical carriers, *Nat. Rev. Drug Discovery*, 4 (2005) 145-160.
- [52] P.P. Constantinides et al., Advances in lipid nanodispersions for parenteral drug delivery and targeting, *Adv. Drug Delivery Rev.*, 60 (2008) 757-767.
- [53] S. Tamilvanan, Formulation of multifunctional oil-in-water nanosized emulsions for active and passive targeting of drugs to otherwise inaccessible internal organs of the human body, *Int. J. Pharm.*, 381 (2009) 62-76.
- [54] P.T. Spicer, Progress in liquid crystalline dispersions: Cubosomes, *Curr. Opin. Colloid Interface Sci.*, 10 (2005) 274-279.
- [55] D. Yang et al., Cubic Liquid–Crystalline Nanoparticles, *Angew. Chem., Int. Ed.*, 43 (2004) 4402-4409.
- [56] J. Kuntsche et al., Supercooled Smectic Nanoparticles: A Potential Novel Carrier System for Poorly Water Soluble Drugs, *Pharm. Res.*, 21 (2004) 1834-1843.
- [57] C.E. Mora-Huertas et al., Polymer-based nanocapsules for drug delivery, *Int. J. Pharm.*, 385 (2010) 113-142.

- [58] N.T. Huynh et al., Lipid nanocapsules: a new platform for nanomedicine, *Int. J. Pharm.*, 379 (2009) 201-209.
- [59] C. Preetz et al., Preparation and characterization of biocompatible oil-loaded polyelectrolyte nanocapsules, *Nanomedicine (Philadelphia, PA, US)*, 4 (2008) 106-114.
- [60] K. Jores et al., Investigations on the structure of solid lipid nanoparticles (SLN) and oil-loaded solid lipid nanoparticles by photon correlation spectroscopy, field-flow fractionation and transmission electron microscopy, *J. Controlled Release*, 95 (2004) 217-227.
- [61] R.H. Müller et al., Nanostructured lipid matrices for improved microencapsulation of drugs, *Int. J. Pharm.*, 242 (2002) 121-128.
- [62] S. Doktorovova and E.B. Souto, Nanostructured lipid carrier-based hydrogel formulations for drug delivery: a comprehensive review, *Expert Opin. Drug Deliv.*, (2009).
- [63] A. Kumari et al., Biodegradable polymeric nanoparticles based drug delivery systems, *Colloids Surf. B*, 75 (2010) 1-18.
- [64] L.E. van Vlerken and M.M. Amiji, Multi-functional polymeric nanoparticles for tumour-targeted drug delivery, *Expert Opin. Drug Deliv.*, (2006).
- [65] S. Acharya and S.K. Sahoo, PLGA nanoparticles containing various anticancer agents and tumour delivery by EPR effect, *Adv. Drug Delivery Rev.*, 63 (2011) 170-183.
- [66] F. Danhier et al., PLGA-based nanoparticles: An overview of biomedical applications, *J. Controlled Release*, 161 (2012) 505-522.
- [67] W. Mehnert and K. Mäder, Solid lipid nanoparticles: production, characterization and applications, *Adv. Drug Delivery Rev.*, 47 (2001) 165-196.
- [68] J. Kuntsche and K. Mäder, Solid lipid nanoparticles (SLN) for drug delivery, in: V. Torchilin and M.A. Mansoor (Eds.), *Handbook of Materials for Nanomedicine*, Pan Stanford Publishing, Singapore, 2011, 383-443.
- [69] K. Westesen, Novel lipid-based colloidal dispersions as potential drug administration systems – expectations and reality, *Colloid Polym. Sci.*, 278 (2000) 608-618.
- [70] C. Washington and K. Evans, Release rate measurements of model hydrophobic solutes from submicron triglyceride emulsions, *J. Controlled Release*, 33 (1995) 383-390.
- [71] B. Magenheimer et al., A new in vitro technique for the evaluation of drug release profile from colloidal carriers - ultrafiltration technique at low pressure, *Int. J. Pharm.*, 94 (1993) 115-123.
- [72] K. Westesen et al., Physicochemical characterization of lipid nanoparticles and evaluation of their drug loading capacity and sustained release potential, *J. Controlled Release*, 48 (1997) 223-236.
- [73] T. Govender et al., PLGA nanoparticles prepared by nanoprecipitation: drug loading and release studies of a water soluble drug, *J. Controlled Release*, 57 (1999) 171-185.
- [74] E. Leo et al., In vitro evaluation of PLA nanoparticles containing a lipophilic drug in water-soluble or insoluble form, *Int. J. Pharm.*, 278 (2004) 133-141.
- [75] M.G. Cascone et al., Release of dexamethasone from PLGA nanoparticles entrapped into dextran/poly(vinyl alcohol) hydrogels, *J. Mater. Sci.: Mater. Med.*, 13 (2002) 265-269.
- [76] R.H. Müller et al., Pharmaceutical nanosuspensions as dosage forms with enhanced saturation solubility and dissolution rate, German Patent DE44440337A1 (1996)
- [77] B. Siekmann and K. Westesen, Thermoanalysis of the recrystallization process of melt-homogenized glyceride nanoparticles, *Colloids Surf. B*, 3 (1994) 159-175.
- [78] A. zur Mühlen et al., Solid lipid nanoparticles (SLN) for controlled drug delivery – drug release and release mechanism, *Eur. J. Pharm. Biopharm.*, 45 (1998) 149-155.
- [79] K. Jores et al., Physicochemical investigations on solid lipid nanoparticles and on oil-loaded solid lipid nanoparticles: a nuclear magnetic resonance and electron spin resonance study, *Pharm. Res.*, 20 (2003) 1274-1283.
- [80] K. Jores et al., Solid lipid nanoparticles (SLN) and oil-loaded SLN studied by spectrofluorometry and Raman spectroscopy, *Pharm. Res.*, 22 (2005) 1887-1897.
- [81] R. Sivaramakrishnan et al., Glucocorticoid entrapment into lipid carriers – characterisation by parrlectric spectroscopy and influence on dermal uptake, *J. Controlled Release*, 97 (2004) 493-502.
- [82] V. Jenning et al., Vitamin A-loaded solid lipid nanoparticles for topical use: drug release properties, *J. Controlled Release*, 66 (2000) 115-126.
- [83] C. Freitas and R.H. Müller, Correlation between long-term stability of solid lipid nanoparticles (SLNTM) and crystallinity of the lipid phase, *Eur. J. Pharm. Biopharm.*, 47 (1999) 125-132.
- [84] T. Ameller et al., Polyester-poly(ethylene glycol) nanoparticles loaded with the pure antiestrogen RU 58668: physicochemical and opsonization properties, *Pharm. Res.*, 20 (2003) 1063-1070.

- [85] T. Riley et al., Physicochemical Evaluation of Nanoparticles Assembled from Poly(lactic acid)–Poly(ethylene glycol) (PLA–PEG) Block Copolymers as Drug Delivery Vehicles, *Langmuir*, 17 (2001) 3168-3174.
- [86] S.M. Moghimi et al., Long-circulating and target-specific nanoparticles: theory to practice, *Pharmacol. Rev.*, 53 (2001) 283-318.
- [87] H. Fessi et al., Nanocapsule formation by interfacial polymer deposition following solvent displacement, *Int. J. Pharm.*, 55 (1989) R1-R4.
- [88] M.C. Garnett and P. Kallinteri, Nanomedicines and nanotoxicology: some physiological principles, *Occup. Med. (Lond.)*, 56 (2006) 307-311.
- [89] H. Orafi et al., Novel poly(glycerol-adipate) polymers used for nanoparticle making: a study of surface free energy, *Iran. J. Pharm. Res.*, 7 (2008) 11-19.
- [90] S. Puri et al., Drug incorporation and release of water soluble drugs from novel functionalized poly(glycerol adipate) nanoparticles, *J. Controlled Release*, 125 (2008) 59-67.
- [91] W. Meng et al., Uptake and metabolism of novel biodegradable poly (glycerol-adipate) nanoparticles in DAOY monolayer, *J. Controlled Release*, 116 (2006) 314-321.
- [92] W. Meng et al., Evaluation of poly (glycerol-adipate) nanoparticle uptake in an in vitro 3-D brain tumor co-culture model, *Exp. Biol. Med. (Maywood)*, 232 (2007) 1100-1108.
- [93] A. Vonarbourg et al., Parameters influencing the stealthiness of colloidal drug delivery systems, *Biomaterials*, 27 (2006) 4356-4373.
- [94] D.E. Owens and N.A. Peppas, Opsonization, biodistribution, and pharmacokinetics of polymeric nanoparticles, *Int. J. Pharm.*, 307 (2006) 93-102.
- [95] D.C. Litzinger et al., Effect of liposome size on the circulation time and intraorgan distribution of amphipathic poly (ethylene glycol)-containing liposomes, *Biochim. Biophys. Acta, Biomembr.*, 1190 (1994) 99-107.
- [96] S.E. Gratton et al., The effect of particle design on cellular internalization pathways, *Proc. Natl. Acad. Sci. U. S. A.*, 105 (2008) 11613-11618.
- [97] A. Juarranz et al., Prediction of in situ fluorescence of histochemical reagents using a structure-staining correlation procedure, *Histochem. Cell Biol.*, 84 (1986) 426-431.
- [98] P. Greenspan and S.D. Fowler, Spectrofluorometric studies of the lipid probe, Nile red, *J. Lipid Res.*, 26 (1985) 781-789.
- [99] V. Jenning and S.H. Gohla, Encapsulation of retinoids in solid lipid nanoparticles (SLN), *J. Microencapsulation*, 18 (2001) 149-158.
- [100] S. D'Souza and P. DeLuca, Methods to Assess in Vitro Drug Release from Injectable Polymeric Particulate Systems, *Pharm. Res.*, 23 (2006) 460-474.
- [101] S. Kamiya et al., Preparation and stabilization of nifedipine lipid nanoparticles, *Int. J. Pharm.*, 354 (2008) 242-247.
- [102] Z. Rahman et al., Non-destructive methods of characterization of risperidone solid lipid nanoparticles, *Eur. J. Pharm. Biopharm.*, 76 (2010) 127-137.
- [103] F. Rashid and R.W. Horobin, Interaction of molecular probes with living cells and tissues. Part 2, *Histochem. Cell Biol.*, 94 (1990) 303-308.
- [104] M.O. Senge and J.C. Brandt, Temoporfin (Foscan[®], 5,10,15,20-Tetra(*m*-hydroxyphenyl)chlorin) – A Second-generation Photosensitizer, *Photochem. Photobiol.*, 87 (2011) 1240-1296.
- [105] J. Robbens et al., Eco-, geno- and human toxicology of bio-active nanoparticles for biomedical applications, *Toxicology*, 269 (2010) 170-181.
- [106] A. Nemmar et al., Passage of intratracheally instilled ultrafine particles from the lung into the systemic circulation in hamster, *Am. J. Respir. Crit. Care Med.*, 164 (2001) 1665-1668.
- [107] S.E. Dunn et al., In vitro cell interaction and in vivo biodistribution of poly(lactide-co-glycolide) nanospheres surface modified by poloxamer and poloxamine copolymers, *J. Controlled Release*, 44 (1997) 65-76.
- [108] J. Kreuter et al., Distribution and elimination of poly(methyl-2-¹⁴C-methacrylate) nanoparticle radioactivity after injection in rats and mice, *J. Pharm. Sci.*, 68 (1979) 1443-1447.
- [109] BioChain. Protocol Manual: Cell Viability Assay Kits. 2005. Newark, CA, USA.
- [110] J. O'Brien et al., Investigation of the Alamar Blue (resazurin) fluorescent dye for the assessment of mammalian cell cytotoxicity, *Eur. J. Biochem.*, 267 (2000) 5421-5426.
- [111] S. Anoopkumar-Dukie et al., Resazurin assay of radiation response in cultured cells, *Br. J. Radiol.*, 78 (2005) 945-947.
- [112] BioVision. Data Sheet: LDA-Cytotoxicity Assay Kit. 2007. Mountain View, CA 94043, USA.
- [113] Molecular Probes. Lipophilic Tracers - DiI, DiO, DiD, DiA, and DiR. 2008. Eugene, OR, US.

- [114] J.V. Frangioni, In vivo near-infrared fluorescence imaging, *Current Opinion in Chemical Biology*, 7 (2003) 626-634.
- [115] R. Weissleder, A clearer vision for in vivo imaging, *Nat. Biotechnol.*, 19 (2001) 316-317.
- [116] A.M. Smith et al., Second window for in vivo imaging, *Nat. Nanotechnol.*, 4 (2009) 710.
- [117] A.J. Shuhendler et al., Hybrid quantum dot–fatty ester stealth nanoparticles: toward clinically relevant *in vivo* optical imaging of deep tissue, *ACS Nano*, 5 (2011) 1958-1966.
- [118] A. Schädlich et al., Tumor Accumulation of NIR Fluorescent PEG–PLA Nanoparticles: Impact of Particle Size and Human Xenograft Tumor Model, *ACS Nano*, 5 (2011) 8710-8720.
- [119] S. Hoffmann et al., Dual Fluorescent HPMA Copolymers for Passive Tumor Targeting with pH-Sensitive Drug Release: Synthesis and Characterization of Distribution and Tumor Accumulation in Mice by Noninvasive Multispectral Optical Imaging, *Biomacromolecules*, 13 (2012) 652-663.
- [120] H. Caysa et al., Monitoring of Xenograft Tumor Growth and Response to Chemotherapy by Non-Invasive In Vivo Multispectral Fluorescence Imaging, *PLoS ONE*, 7 (2012) e47927.
- [121] G. Storm et al., Surface modification of nanoparticles to oppose uptake by the mononuclear phagocyte system, *Adv. Drug Delivery Rev.*, 17 (1995) 31-48.
- [122] S.D. Tröster and J. Kreuter, Influence of the surface properties of low contact angle surfactants on the body distribution of ¹⁴C-poly(methyl methacrylate) nanoparticles, *J. Microencapsulation*, 9 (1992) 19-28.
- [123] P.R. Dash et al., Factors affecting blood clearance and in vivo distribution of polyelectrolyte complexes for gene delivery, *Gene Ther.*, 6 (1999) 643-650.
- [124] N. Bertrand and J.C. Leroux, The journey of a drug-carrier in the body: An anatomico-physiological perspective, *J. Controlled Release*, (2011).
- [125] H. Chen et al., Fast Release of Lipophilic Agents from Circulating PEG-PDLLA Micelles Revealed by in Vivo Förster Resonance Energy Transfer Imaging, *Langmuir*, 24 (2008) 5213-5217.
- [126] R.L. Juliano, Factors affecting the clearance kinetics and tissue distribution of liposomes, microspheres and emulsions, *Adv. Drug Delivery Rev.*, 2 (1988) 31-54.
- [127] S.M. Moghimi, Mechanisms regulating body distribution of nanospheres conditioned with pluronic and tetronic block co-polymers, *Adv. Drug Delivery Rev.*, 16 (1995) 183-193.
- [128] C. Monfardini and F.M. Veronese, Stabilization of Substances in Circulation, *Bioconjugate Chem.*, 9 (1998) 418-450.
- [129] S.M. Moghimi et al., An investigation of the filtration capacity and the fate of large filtered sterically-stabilized microspheres in rat spleen, *Biochim. Biophys. Acta, Gen. Subj.*, 1157 (1993) 233-240.
- [130] R. Gref et al., Biodegradable long-circulating polymer nanospheres, *Science (Washington, DC, US)*, 263 (1994) 1600-1603.
- [131] R. Gref et al., The controlled intravenous delivery of drugs using PEG-coated sterically stabilized nanospheres, *Adv. Drug Delivery Rev.*, 16 (1995) 215-233.
- [132] D. Bazile et al., Stealth Me.PEG-PLA Nanoparticles Avoid Uptake by the Mononuclear Phagocytes System, *J. Pharm. Sci.*, 84 (1995) 493-498.
- [133] S.M. Moghimi and J. Szabeni, Stealth liposomes and long circulating nanoparticles: critical issues in pharmacokinetics, opsonization and protein-binding properties, *Prog. Lipid Res.*, 42 (2003) 463-478.
- [134] L. Illum et al., Surface characteristics and the interaction of colloidal particles with mouse peritoneal macrophages, *Biomaterials*, 8 (1987) 113-117.
- [135] D.D. Lasic et al., Sterically stabilized liposomes: a hypothesis on the molecular origin of the extended circulation times, *Biochim. Biophys. Acta, Biomembr.*, 1070 (1991) 187-192.
- [136] V.P. Torchilin and M.I. Papisov, Why do Polyethylene Glycol-Coated Liposomes Circulate So Long?: Molecular Mechanism of Liposome Steric Protection with Polyethylene Glycol: Role of Polymer Chain Flexibility, *J. Liposome Res.*, 4 (1994) 725-739.
- [137] W.R. Gombotz et al., Protein adsorption to and elution from polyether surfaces, in: J.M. Harris (Ed.), *Poly (Ethylene Glycol) Chemistry - Biotechnical and Biomedical Applications*, Plenum Press, New York, 1992, 247-260.
- [138] S.M. Moghimi and A.C. Hunter, Poloxamers and poloxamines in nanoparticle engineering and experimental medicine, *Trends Biotechnol.*, 18 (2000) 412-420.
- [139] Y. Noguchi et al., Early Phase Tumor Accumulation of Macromolecules: A Great Difference in Clearance Rate between Tumor and Normal Tissues, *Cancer Sci.*, 89 (1998) 307-314.
- [140] J. Kopecek and P. Kopeckova, HPMA copolymers: Origins, early developments, present, and future, *Adv. Drug Delivery Rev.*, 62 (2010) 122-149.

- [141] T. Lammers, Improving the efficacy of combined modality anticancer therapy using HPMA copolymer-based nanomedicine formulations, *Adv. Drug Delivery Rev.*, 62 (2010) 203-230.
- [142] R. Duncan and M.J. Vicent, Do HPMA copolymer conjugates have a future as clinically useful nanomedicines? A critical overview of current status and future opportunities, *Adv. Drug Delivery Rev.*, 62 (2010) 272-282.
- [143] K. Ulbrich and V. Subr, Structural and chemical aspects of HPMA copolymers as drug carriers, *Adv. Drug Delivery Rev.*, 62 (2010) 150-166.
- [144] J.G. Shiah et al., Biodistribution and antitumor efficacy of long-circulating N-(2-hydroxypropyl)methacrylamide copolymer–doxorubicin conjugates in nude mice, *Eur. J. Cancer*, 37 (2001) 131-139.
- [145] K. Ulbrich et al., HPMA copolymers with pH-controlled release of doxorubicin: In vitro cytotoxicity and in vivo antitumor activity, *J. Controlled Release*, 87 (2003) 33-47.
- [146] P.A. Vasey et al., Phase I clinical and pharmacokinetic study of PK1 [N-(2-hydroxypropyl)methacrylamide copolymer doxorubicin]: first member of a new class of chemotherapeutic agents–drug-polymer conjugates, *Clin. Cancer Res.*, 5 (1999) 83-94.
- [147] M.J. Vicent and R. Duncan, Polymer conjugates: nanosized medicines for treating cancer, *Trends Biotechnol.*, 24 (2006) 39-47.
- [148] P. Chytil et al., New HPMA copolymer-based drug carriers with covalently bound hydrophobic substituents for solid tumour targeting, *J. Controlled Release*, 127 (2008) 121.
- [149] S.K. Filippov et al., Macromolecular HPMA-Based Nanoparticles with Cholesterol for Solid-Tumor Targeting: Detailed Study of the Inner Structure of a Highly Efficient Drug Delivery System, *Biomacromolecules*, 13 (2012) 2594-2604.
- [150] V. Subr et al., Coating of DNA/Poly(l-lysine) Complexes by Covalent Attachment of Poly[N-(2-hydroxypropyl)methacrylamide], *Biomacromolecules*, 7 (2006) 122-130.
- [151] D. Oupický et al., Steric Stabilization of poly-l-Lysine/DNA Complexes by the Covalent Attachment of Semitelechelic poly[N-(2-Hydroxypropyl)methacrylamide], *Bioconjugate Chem.*, 11 (2000) 492-501.
- [152] C.M. Ward et al., Modification of pLL/DNA complexes with a multivalent hydrophilic polymer permits folate-mediated targeting in vitro and prolonged plasma circulation in vivo, *J. Gene Med.*, 4 (2002) 536-547.
- [153] N.K. Green et al., Extended plasma circulation time and decreased toxicity of polymer-coated adenovirus, *Gene Ther.*, 11 (2004) 1256-1263.
- [154] P.R. Dash et al., Decreased Binding to Proteins and Cells of Polymeric Gene Delivery Vectors Surface Modified with a Multivalent Hydrophilic Polymer and Retargeting through Attachment of Transferrin, *J. Biol. Chem.*, 275 (2000) 3793-3802.
- [155] K.D. Fisher et al., A versatile system for receptor-mediated gene delivery permits increased entry of DNA into target cells, enhanced delivery to the nucleus and elevated rates of transgene expression, *Gene Ther.*, 7 (2000) 1337-1343.
- [156] R. Laga et al., Coating of nanoparticles bearing amino groups on the surface with hydrophilic HPMA-based polymers, *Colloid Polym. Sci.*, 285 (2007) 1509-1514.
- [157] T. Naolou et al., Synthesis of Well-Defined Graft Copolymers by Combination of Enzymatic Polycondensation and Click Chemistry, *Biomacromolecules*, 11 (2010) 3660-3667.
- [158] B.J. Kline et al., One-step biocatalytic synthesis of linear polyesters with pendant hydroxyl groups, *J. Am. Chem. Soc.*, 120 (1998) 9475-9480.
- [159] H. Uyama et al., Lipase-catalyzed polycondensation of dicarboxylic acid–divinyl esters and glycols to aliphatic polyesters, *J. Polym. Sci. A: Polym. Chem.*, 37 (1999) 2737-2745.
- [160] S.M. Moghimi, Exploiting bone marrow microvascular structure for drug delivery and future therapies, *Adv. Drug Delivery Rev.*, 17 (1995) 61-73.
- [161] K. Sou et al., Bone marrow-targeted liposomal carriers, *Expert Opin. Drug Deliv.*, 8 (2011) 317-328.
- [162] C.J.H. Porter et al., The polyoxyethylene/polyoxypropylene block co-polymer Poloxamer-407 selectively redirects intravenously injected microspheres to sinusoidal endothelial cells of rabbit bone marrow, *FEBS Letters*, 305 (1992) 62-66.
- [163] R. Deanesly and A.S. Parkes, Biological properties of some new derivatives of testosterone, *Biochem. J.*, 31 (1937) 1161.
- [164] C.D. Kochakian, A comparison of the renotropic with the androgenic activity of various steroids, *Am. J. Physiol. Legacy Cont.*, 142 (1944) 315-325.
- [165] J. Folkman et al., Silicone rubber: a new diffusion property useful for general anesthesia, *Science (Washington, DC, US)*, 154 (1966) 148-149.

- [166] M.F. Armaly and K.R. Rao, The Effect of Pilocarpine Ocuser With Different Release Rates on Ocular Pressure, *Invest. Ophthalmol. Vis. Sci.*, 12 (1973) 491-496.
- [167] I. Sivin et al., Norplant: Reversible Implant Contraception, *Stud. Fam. Plann.*, 11 (1980) 227-235.
- [168] J.R. Cardinal et al., Hydrogel devices for the controlled release of steroid hormones, in: R. Baker (Ed.), *Controlled Release of Bioactive Materials*, Academic Press, New York, USA, 1980, 123.
- [169] F. Theeuwes and S.I. Yum, Principles of the design and operation of generic osmotic pumps for the delivery of semisolid or liquid drug formulations, *Ann. Biomed. Eng.*, 4 (1976) 343-353.
- [170] J.C. Wright et al., An in vivo/in vitro comparison with a leuprolide osmotic implant for the treatment of prostate cancer, *J. Controlled Release*, 75 (2001) 1-10.
- [171] J.M. Anderson and M.S. Shive, Biodegradation and biocompatibility of PLA and PLGA microspheres, *Adv. Drug Delivery Rev.*, 28 (1997) 5-24.
- [172] E. Mathiowitz and R. Langer, Polyanhydride microspheres as drug carriers I. Hot-melt microencapsulation, *J. Controlled Release*, 5 (1987) 13-22.
- [173] X.L. Bai et al., Effect of polymer compositions on the fabrication of poly(ortho-ester) microspheres for controlled release of protein, *J. Appl. Polym. Sci.*, 80 (2001) 1630-1642.
- [174] H. Reithmeier et al., Lipid microparticles as a parenteral controlled release device for peptides, *J. Controlled Release*, 73 (2001) 339-350.
- [175] R.L. Dunn et al., Biodegradable in-situ forming implants and methods of producing the same, US Patent 4,938,763 (1990)
- [176] N.H. Shah et al., A biodegradable injectable implant for delivering micro and macromolecules using poly (lactic-co-glycolic) acid (PLGA) copolymers, *J. Controlled Release*, 27 (1993) 139-147.
- [177] S. Kempe and K. Mäder, In situ forming implants – an attractive formulation principle for parenteral depot formulations, *J. Controlled Release*, (2012).
- [178] D. Chitkara et al., Biodegradable Injectable In Situ Depot-Forming Drug Delivery Systems, *Macromol. Biosci.*, 6 (2006) 977-990.
- [179] C.B. Packhaeuser et al., In situ forming parenteral drug delivery systems: an overview, *Eur. J. Pharm. Biopharm.*, 58 (2004) 445-455.
- [180] H. Kranz et al., Myotoxicity studies of injectable biodegradable in-situ forming drug delivery systems, *Int. J. Pharm.*, 212 (2001) 11-18.
- [181] K. Mäder et al., Non-invasive in vivo characterization of release processes in biodegradable polymers by low-frequency electron paramagnetic resonance spectroscopy, *Biomaterials*, 17 (1996) 457-461.
- [182] C.M. Agrawal and K.A. Athanasiou, Technique to control pH in vicinity of biodegrading PLA-PGA implants, *J. Biomed. Mater. Res.*, 38 (1997) 105-114.
- [183] A. Brunner et al., pH and Osmotic Pressure Inside Biodegradable Microspheres During Erosion, *Pharm. Res.*, 16 (1999) 847-853.
- [184] Q. Ye et al., DepoFoam™ technology: a vehicle for controlled delivery of protein and peptide drugs, *J. Controlled Release*, 64 (2000) 155-166.
- [185] M.S. Angst and D.R. Drover, Pharmacology of Drugs Formulated with DepoFoam™, *Clin. Pharmacokinet.*, 45 (2006) 1153-1176.
- [186] L.R. Asmus et al., Solutions as solutions – Synthesis and use of a liquid polyester excipient to dissolve lipophilic drugs and formulate sustained-release parenterals, *Eur. J. Pharm. Biopharm.*, 79 (2011) 584-591.
- [187] L.R. Asmus et al., Single processing step toward injectable sustained-release formulations of Triptorelin based on a novel degradable semi-solid polymer, *Eur. J. Pharm. Biopharm.*, 81 (2012) 591-599.
- [188] U. Massing et al., Dual asymmetric centrifugation (DAC) – A new technique for liposome preparation, *J. Controlled Release*, 125 (2008) 16-24.
- [189] W. Tian et al., Vesicular phospholipid gel-based depot formulations for pharmaceutical proteins: Development and in vitro evaluation, *J. Controlled Release*, 142 (2010) 319-325.
- [190] A.R. Rajabi-Siahboomi et al., Structure and behaviour in hydrophilic matrix sustained release dosage forms: 2. NMR-imaging studies of dimensional changes in the gel layer and core of HPMC tablets undergoing hydration, *J. Controlled Release*, 31 (1994) 121-128.
- [191] J.C. Richardson et al., Pharmaceutical applications of magnetic resonance imaging (MRI), *Adv. Drug Delivery Rev.*, 57 (2005) 1191-1209.
- [192] B. Madhu et al., Studies of the internal flow process in polymers by ¹H NMR microscopy at 500 MHz, *J. Controlled Release*, 56 (1998) 95-104.
- [193] H. Metz and K. Mäder, Benchtop-NMR and MRI - A new analytical tool in drug delivery research, *Int. J. Pharm.*, 364 (2008) 170-175.

- [194] G.J. Hirasaki et al., NMR properties of petroleum reservoir fluids, *Magn. Reson. Imaging*, 21 (2003) 269-277.
- [195] G.R. Eaton and S.S. Eaton, Introduction to EPR imaging using magnetic-field gradients, *Concepts Magn. Reson.*, 7 (1995) 49-67.
- [196] K. Mäder et al., Non-destructive and localized assessment of acidic microenvironments inside biodegradable polyanhydrides by spectral spatial electron paramagnetic resonance imaging, *Polymer*, 38 (1997) 4785-4794.
- [197] M. Morlock et al., Microencapsulation of rh-erythropoietin, using biodegradable poly(D,L-lactide-co-glycolide): protein stability and the effects of stabilizing excipients, *Eur. J. Pharm. Biopharm.*, 43 (1997) 29-36.
- [198] K. Ulbrich et al., Polymeric drugs based on conjugates of synthetic and natural macromolecules: I. Synthesis and physico-chemical characterisation, *J. Controlled Release*, 64 (2000) 63-79.
- [199] K. Ulbrich et al., Antibody-targeted Polymer–doxorubicin Conjugates with pH-controlled Activation, *J. Drug Targeting*, 12 (2004) 477-489.
- [200] P. Chytil et al., Properties of HPMA copolymer–doxorubicin conjugates with pH-controlled activation: Effect of polymer chain modification, *J. Controlled Release*, 115 (2006) 26-36.
- [201] T. Etrych et al., Synthesis of HPMA Copolymers Containing Doxorubicin Bound via a Hydrazone Linkage. Effect of Spacer on Drug Release and in vitro Cytotoxicity, *Macromol. Biosci.*, 2 (2002) 43-52.
- [202] T. Etrych et al., N-(2-Hydroxypropyl) methacrylamide–based polymer conjugates with pH-controlled activation of doxorubicin. I. New synthesis, physicochemical characterization and preliminary biological evaluation, *J. Appl. Polym. Sci.*, 109 (2008) 3050-3061.
- [203] F. Esmaeili et al., Preparation and antibacterial activity evaluation of rifampicin-loaded poly lactide-co-glycolide nanoparticles, *Nanomedicine (Philadelphia, PA, US)*, 3 (2007) 161-167.
- [204] H.W. Zhang et al., Preparation of poly(lactide-co-glycolide-co-caprolactone) nanoparticles and their degradation behaviour in aqueous solution, *Polym. Degrad. Stab.*, 91 (2006) 1929-1936.
- [205] J. Kuntsche et al., Size Determinations of Colloidal Fat Emulsions: A Comparative Study, *J. Biomed. Nanotechnol.*, 5 (2009) 384-395.
- [206] N. Stribeck and J. Martinez-Vazquez, X-ray scattering of soft matter, Springer, Heidelberg, 2007.
- [207] GE Healthcare. PD-10 Desalting Columns - Instructions. 2012. Little Chalfont, UK.
- [208] G. Fagadar-Cosma et al., Electrochemical and Spectroscopic Studies of 5,10,15,20-Tetrakis(4-hydroxyphenyl)-21H,23H-porphine, *Chem. Bull. 'POLITEHNICA' Univ. (Timisoara)*, 52 (2007) 109-112.
- [209] A. Synak et al., Femtosecond Dynamics of a Porphyrin Derivative Confined by the Human Serum Albumin Protein, *J. Phys. Chem. B*, 114 (2010) 16567-16573.
- [210] M.S. Niepel et al., pH-dependent modulation of fibroblast adhesion on multilayers composed of poly (ethylene imine) and heparin, *Biomaterials*, 30 (2009) 4939-4947.
- [211] D.M. Euhus et al., Tumor measurement in the nude mouse, *J. Surg. Oncol.*, 31 (1986) 229-234.
- [212] M.M. Tomayko and C.P. Reynolds, Determination of subcutaneous tumor size in athymic (nude) mice, *Cancer Chemother. Pharmacol.*, 24 (1989) 148-154.
- [213] I. Özcan et al., Synthesis and characterization of surface-modified PBLG nanoparticles for bone targeting: In vitro and in vivo evaluations, *J. Pharm. Sci.*, 100 (2011) 4877-4887.
- [214] I. Bravo-Osuna et al., In vitro evaluation of calcium binding capacity of chitosan and thiolated chitosan poly(isobutyl cyanoacrylate) core–shell nanoparticles, *Int. J. Pharm.*, 338 (2007) 284-290.
- [215] D. Wang et al., Synthesis and Evaluation of Water-Soluble Polymeric Bone-Targeted Drug Delivery Systems, *Bioconjugate Chem.*, 14 (2003) 853-859.
- [216] H.Y. Carr and E.M. Purcell, Effects of Diffusion on Free Precession in Nuclear Magnetic Resonance Experiments, *Phys. Rev.*, 94 (1954) 630-638.
- [217] A. Keith et al., Spin-labeled Neurospora mitochondria, *Biophys. J.*, 10 (1970) 618.
- [218] A.D. Keith et al., Spin-label studies on the aqueous regions of phospholipid multilayers, *Biochemistry*, 16 (1977) 634-641.
- [219] S. Puri, Novel functionalized polymers for nanoparticle formulations with anti cancer drugs, Thesis, Nottingham, UK, 2007
- [220] S.M. Moghimi et al., Nanomedicine: current status and future prospects, *FASEB J.*, 19 (2005) 311-330.
- [221] R.H. Müller, Zetapotential und Partikelladung in der Laborpraxis - Einführung in die Theorie, praktische Meßdurchführung, Dateninterpretation, Wissenschaftliche Verlagsgesellschaft, Stuttgart, 1996.

- [222] J. Kuntsche et al., Cryogenic transmission electron microscopy (cryo-TEM) for studying the morphology of colloidal drug delivery systems, *Int. J. Pharm.*, 417 (2011) 120-137.
- [223] D.P. Foster et al., Macrophase and Microphase Separation in Random Comb Copolymers, *Macromolecules* (Washington, DC, US), 28 (1995) 3450-3462.
- [224] D. Curco and C. Aleman, Modeling the amorphous phase of comb-like polymers, *J. Polym. Sci. B Polym. Phys.*, 44 (2006) 953-966.
- [225] H. Shi et al., Effect of main-chain rigidity on the phase transitional behavior of comblike polymers, *Macromolecules* (Washington, DC, US), 40 (2007) 3198-3203.
- [226] Y. Zhou et al., Confined crystallization and phase transition in semi-rigid chitosan containing long chain alkyl groups, *CrystEngComm*, 13 (2011) 561-567.
- [227] M. Beiner and H. Huth, Nanophase separation and hindered glass transition in side-chain polymers, *Nat. Mater.*, 2 (2003) 595-599.
- [228] T.P. Lodge et al., Introductory Lecture Strategies for controlling intra- and intermicellar packing in block copolymer solutions: Illustrating the flexibility of the self-assembly toolbox, *Faraday Discuss.*, 128 (2005).
- [229] C. Neto et al., Imaging soft matter with the atomic force microscope: cubosomes and hexosomes, *J. Phys. Chem. B*, 103 (1999) 3896-3899.
- [230] P.J. Wyatt, Submicrometer particle sizing by multiangle light scattering following fractionation, *J. Colloid Interface Sci.*, 197 (1998) 9-20.
- [231] W. Van de Sande and A. Persoons, The size and shape of macromolecular structures: determination of the radius, the length and the persistence length of rod-like micelles of dodecyldimethylammonium chloride and bromide, *J. Phys. Chem.*, 89 (1985) 404-406.
- [232] D. Kunz et al., Dynamic light scattering from spherical particles, *Colloid Polym. Sci.*, 261 (1983) 635-644.
- [233] J. Lohrke et al., Characterization of superparamagnetic iron oxide nanoparticles by asymmetrical flow-field-flow-fractionation, *Nanomedicine (Lond.)*, 3 (2008) 437-452.
- [234] O. Stauch et al., Structure of Artificial Cytoskeleton Containing Liposomes in Aqueous Solution Studied by Static and Dynamic Light Scattering, *Biomacromolecules*, 3 (2002) 565-578.
- [235] H. Bunjes et al., Crystallization tendency and polymorphic transitions in triglyceride nanoparticles, *Int. J. Pharm.*, 129 (1996) 159-173.
- [236] H. Shi et al., Packing mode and conformational transition of alkyl side chains in N-alkylated poly(p-benzamide) comb-like polymer, *Polymer*, 45 (2004) 6299-6307.
- [237] T. Unruh et al., Observation of size-dependent melting in lipid nanoparticles, *J. Phys. Chem. B*, 103 (1999) 10373-10377.
- [238] J.S. Hrkach et al., Nanotechnology for biomaterials engineering: structural characterization of amphiphilic polymeric nanoparticles by ¹H NMR spectroscopy, *Biomaterials*, 18 (1997) 27-30.
- [239] H.E. Gottlieb et al., NMR Chemical Shifts of Common Laboratory Solvents as Trace Impurities, *J. Org. Chem.*, 62 (1997) 7512-7515.
- [240] C.G. Vonk, Synthetic polymers in the solid state, in: O. Glatter and O. Kratky (Eds.), *Small angle X-ray scattering*, Academic Press, London, 1982, 433-466.
- [241] I. Denicolo et al., X-ray study of the rotator phase of paraffins. III. Even-numbered paraffins octadecane, elcosane, docosane, tetracosane, and hexacosane, *J. Chem. Phys.*, 78 (1983) 1465-1469.
- [242] G. Ungar, Structure of rotator phases in n-alkanes, *J. Phys. Chem.*, 87 (1983) 689-695.
- [243] N. Wentzel and S.T. Milner, Crystal and rotator phases of n-alkanes: A molecular dynamics study, *J. Chem. Phys.*, 132 (2010) 1-10.
- [244] N.A. Plate and V.P. Shibaev, Comb-like polymers. Structure and properties, *J. Polym. Sci., Macromol. Rev.*, 8 (1974) 117-253.
- [245] E. Hempel et al., Crystallization of frustrated alkyl groups in polymeric systems containing octadecylmethacrylate, in: G. Reiter and G.R. Strobl (Eds.), *Progress in Understanding of Polymer Crystallization, Lecture Notes in Physics*, Springer GmbH, Berlin, Germany, 2007, 201-228.
- [246] E.B. Sirota et al., Novel phase behavior in normal alkanes, *Phys. Rev. Lett.*, 68 (1992) 492-495.
- [247] A.B. Herhold et al., A vanishing nucleation barrier for the n-alkane rotator-to-crystal transformation, *J. Chem. Phys.*, 116 (2002) 9036.
- [248] G. Ungar and N. Masic, Order in the Rotator Phase of n-Alkanes, *J. Phys. Chem.*, 89 (1985) 1036-1042.
- [249] G. Porod, Die Rontgenkleinwinkelstreuung von dichtgepackten kolloiden Systemen, *Colloid Polym. Sci.*, 124 (1951) 83-114.

- [250] R. Gref et al., 'Stealth' corona-core nanoparticles surface modified by polyethylene glycol (PEG): influences of the corona (PEG chain length and surface density) and of the core composition on phagocytic uptake and plasma protein adsorption, *Colloids Surf. B*, 18 (2000) 301-313.
- [251] D. Kim et al., Interaction of PLGA nanoparticles with human blood constituents, *Colloids Surf. B*, 40 (2005) 83-91.
- [252] M.M. Nociari et al., A novel one-step, highly sensitive fluorometric assay to evaluate cell-mediated cytotoxicity, *J. Immunol. Methods*, 213 (1998) 157-167.
- [253] M. Löbler et al., Sample Geometry Influences the Outcome of in vitro Cytotoxicity Tests, *Adv. Eng. Mater.*, 10 (2008) B72-B76.
- [254] J.A. Ontko, Metabolism of Free Fatty Acids in Isolated Liver Cells, *J. Biol. Chem.*, 247 (1972) 1788-1800.
- [255] K.M. Hawker et al., Interleukin-4 inhibits mitogen-induced proliferation of human airway smooth muscle cells in culture, *Am. J. Physiol. Lung Cell Mol. Physiol.*, 275 (1998) L469-L477.
- [256] D. Leu et al., Distribution and elimination of coated polymethyl [2-¹⁴C]methacrylate nanoparticles after intravenous injection in rats, *J. Pharm. Sci.*, 73 (1984) 1433-1437.
- [257] L.W. Seymour et al., Effect of molecular weight (Mw) of N-(2-hydroxypropyl) methacrylamide copolymers on body distribution and rate of excretion after subcutaneous, intraperitoneal, and intravenous administration to rats, *J. Biomed. Mater. Res.*, 21 (1987) 1341-1358.
- [258] S. Petersen et al., Flow Cytometry as a New Approach To Investigate Drug Transfer between Lipid Particles, *Mol. Pharmaceutics*, 7 (2010) 350-363.
- [259] S. Stolik et al., Measurement of the penetration depths of red and near infrared light in human *ex vivo* tissues, *J. Photochem. Photobiol. B*, 57 (2000) 90-93.
- [260] J. Eichler et al., Measurements on the depth of penetration of light (0.35–1.0 μm) in tissue, *Radiat. Environ. Biophys.*, 14 (1977) 239-242.
- [261] L. Grislain et al., Pharmacokinetics and distribution of a biodegradable drug-carrier, *Int. J. Pharm.*, 15 (1983) 335-345.
- [262] A. Schädlich et al., Accumulation of nanocarriers in the ovary: A neglected toxicity risk?, *J. Controlled Release*, 160 (2012) 105-112.
- [263] G. Thurston et al., Cationic liposomes target angiogenic endothelial cells in tumors and chronic inflammation in mice, *J. Clin. Invest.*, 101 (1998) 1401.
- [264] A.C. Faure et al., Control of the in vivo Biodistribution of Hybrid Nanoparticles with Different Poly(ethylene glycol) Coatings, *Small*, 5 (2009) 2565-2575.
- [265] M. Goutayer et al., Tumor targeting of functionalized lipid nanoparticles: Assessment by in vivo fluorescence imaging, *Eur. J. Pharm. Biopharm.*, 75 (2010) 137-147.
- [266] V. Simon et al., Pp IX silica nanoparticles demonstrate differential interactions with in vitro tumor cell lines and in vivo mouse models of human cancers, *Photochem. Photobiol.*, 86 (2009) 213-222.
- [267] L.P. Reynolds et al., Angiogenesis in the corpus luteum, *Endocrine*, 12 (2000) 1-9.
- [268] M. Goutayer et al., Tumor targeting of functionalized lipid nanoparticles: Assessment by in vivo fluorescence imaging, *Eur. J. Pharm. Biopharm.*, 75 (2010) 137-147.
- [269] R. Weissleder et al., Polymeric contrast agents for MR imaging of adrenal glands, *J. Magn. Reson. Imaging*, 3 (1993) 93-97.
- [270] W.Y. Kim et al., Histological study of gender differences in accumulation of silver nanoparticles in kidneys of Fischer 344 rats, *J. Toxicol. Environ. Health, Part A*, 72 (2009) 1279-1284.
- [271] S.K. Balasubramanian et al., Biodistribution of gold nanoparticles and gene expression changes in the liver and spleen after intravenous administration in rats, *Biomaterials*, 31 (2010) 2034-2042.
- [272] T. Lammers et al., Effect of physicochemical modification on the biodistribution and tumor accumulation of HPMA copolymers, *J. Controlled Release*, 110 (2005) 103-118.
- [273] T. Lammers et al., Simultaneous delivery of doxorubicin and gemcitabine to tumors in vivo using prototypic polymeric drug carriers, *Biomaterials*, 30 (2009) 3466-3475.
- [274] M.P. Borgman et al., Tumor-targeted HPMA copolymer-(RGDFK)-(CHX-A"-DTPA) conjugates show increased kidney accumulation, *J. Controlled Release*, 132 (2008) 193-199.
- [275] A. Mitra et al., Technetium-99m-labeled N-(2-hydroxypropyl) methacrylamide copolymers: synthesis, characterization, and in vivo biodistribution, *Pharm. Res.*, 21 (2004) 1153-1159.
- [276] T. Lammers et al., Polymeric nanomedicines for image-guided drug delivery and tumor-targeted combination therapy, *Nano Today*, 5 (2010) 197-212.
- [277] J. Engel et al., Calcium binding domains and calcium-induced conformational transition of SPARC/BM-40/osteonectin, an extracellular glycoprotein expressed in mineralized and nonmineralized tissues, *Biochemistry*, 26 (1987) 6958-6965.

- [278] M.E. Bolander et al., Osteonectin cDNA sequence reveals potential binding regions for calcium and hydroxyapatite and shows homologies with both a basement membrane protein (SPARC) and a serine proteinase inhibitor (ovomuroid), *Proc. Natl. Acad. Sci. U. S. A.*, 85 (1988) 2919-2923.
- [279] R. Fujisawa et al., Acidic amino acid-rich sequences as binding sites of osteonectin to hydroxyapatite crystals, *Biochim. Biophys. Acta, Protein Struct. Mol. Enzymol.*, 1292 (1996) 53-60.
- [280] F. Ryuichi and K. Yoshinori, Preferential adsorption of dentin and bone acidic proteins on the (100) face of hydroxyapatite crystals, *Biochim. Biophys. Acta, Gen. Subj.*, 1075 (1991) 56-60.
- [281] T.C. Lee et al., Sequential labelling of microdamage in bone using chelating agents, *J. Orthop. Res.*, 18 (2000) 322-325.
- [282] K. Yokogawa et al., Selective Delivery of Estradiol to Bone by Aspartic Acid Oligopeptide and Its Effects on Ovariectomized Mice, *Endocrinology*, 142 (2001) 1228-1233.
- [283] Z. Zhang et al., Preparation of functionalized gold nanoparticles as a targeted X-ray contrast agent for damaged bone tissue, *Nanoscale*, 2 (2010).
- [284] R.D. Ross and R.K. Roeder, Binding affinity of surface functionalized gold nanoparticles to hydroxyapatite, *J. Biomed. Mater. Res. Part A*, 99A (2011) 58-66.
- [285] N. Bloembergen et al., Relaxation effects in nuclear magnetic resonance absorption, *Phys. Rev.*, 73 (1948) 679-712.
- [286] Brookfield Engineering Laboratories. Brookfield CT3 Texture Analyzer - Operating Instructions. 2012. Middleboro, USA.
- [287] A.S. Szczesniak, Classification of Textural Characteristics, *J. Food Sci.*, 28 (1963) 385-389.
- [288] H.H. Friedman et al., The Texturometer – A New Instrument for Objective Texture Measurement, *J. Food Sci.*, 28 (1963) 390-396.
- [289] H. Herich, Untersuchung der Reorientierungsdynamik von Nitroxid-Spinlabeln in Proteinen und Modellsystemen, GRIN Verlag, München, 2007.
- [290] A.D. Keith et al., Factors restricting diffusion of water-soluble spin labels, *Biophys. J.*, 19 (1977) 205-218.
- [291] M.F. Ottaviani et al., Nitrogen hyperfine splitting of nitroxide solutions: Differently structured and charged nitroxides as probes of environmental properties, *Magn. Reson. Chem.*, 25 (1987) 897-904.
- [292] H. Metz. Personal Communication. 2013.
- [293] S. Kempe et al., Characterization of thermosensitive chitosan-based hydrogels by rheology and electron paramagnetic resonance spectroscopy, *Eur. J. Pharm. Biopharm.*, 68 (2008) 26-33.
- [294] J.V. Frangioni, In vivo near-infrared fluorescence imaging, *Curr. Opin. Chem. Biol.*, 7 (2003) 626-634.
- [295] S. Kempe et al., Non-invasive in vivo evaluation of in situ forming PLGA implants by benchtop magnetic resonance imaging (BT-MRI) and EPR spectroscopy, *Eur. J. Pharm. Biopharm.*, 74 (2010) 102-108.
- [296] W.H. De Jong et al., Tissue response to partially in vitro predegraded poly-L-lactide implants, *Biomaterials*, 26 (2005) 1781-1791.
- [297] L. Requena et al., Adverse reactions to injectable soft tissue fillers, *J. Am. Acad. Dermatol.*, 64 (2011) 1-34.
- [298] J. Sun et al., Injectable chitosan-based hydrogel for implantable drug delivery: Body response and induced variations of structure and composition, *J. Biomed. Mater. Res. Part A*, 95 (2010) 1019-1027.
- [299] J.M. Anderson, Biological responses to materials, *Annu. Rev. Mater. Res.*, 31 (2001) 81-110.
- [300] T.G. Park, Degradation of poly(lactic-co-glycolic acid) microspheres: effect of copolymer composition, *Biomaterials*, 16 (1995) 1123-1130.
- [301] A. Göpferich, Mechanisms of polymer degradation and erosion, *Biomaterials*, 17 (1996) 103-114.
- [302] A.M. Reed and D.K. Gilding, Biodegradable polymers for use in surgery – poly (glycolic)/poly (lactic acid) homo and copolymers: 2. *In vitro* degradation, *Polymer*, 22 (1981) 494-498.
- [303] L.R. Asmus et al., In vivo biocompatibility, sustained-release and stability of triptorelin formulations based on a liquid, degradable polymer, *J. Controlled Release*, 165 (2013) 199-206.
- [304] E. Ron et al., Controlled release of polypeptides from polyanhydrides, *Proc. Natl. Acad. Sci. U. S. A.*, 90 (1993) 4176-4180.
- [305] E. Boelsma et al., Assessment of the potential irritancy of oleic acid on human skin: Evaluation in vitro and in vivo, *Toxicol. in Vitro*, 10 (1996) 729-742.
- [306] H. Tanojo et al., In vivo human skin permeability enhancement by oleic acid: a laser Doppler velocimetry study, *J. Controlled Release*, 58 (1999) 97-104.

7 Appendix

7.1 Supplementary material

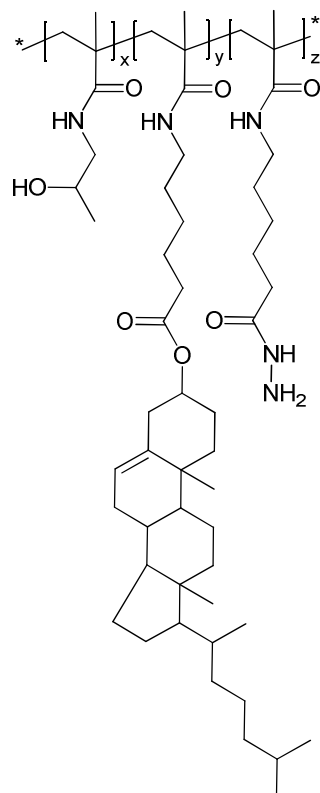


Figure 7-1. Chemical structure of UH18 and UH19.

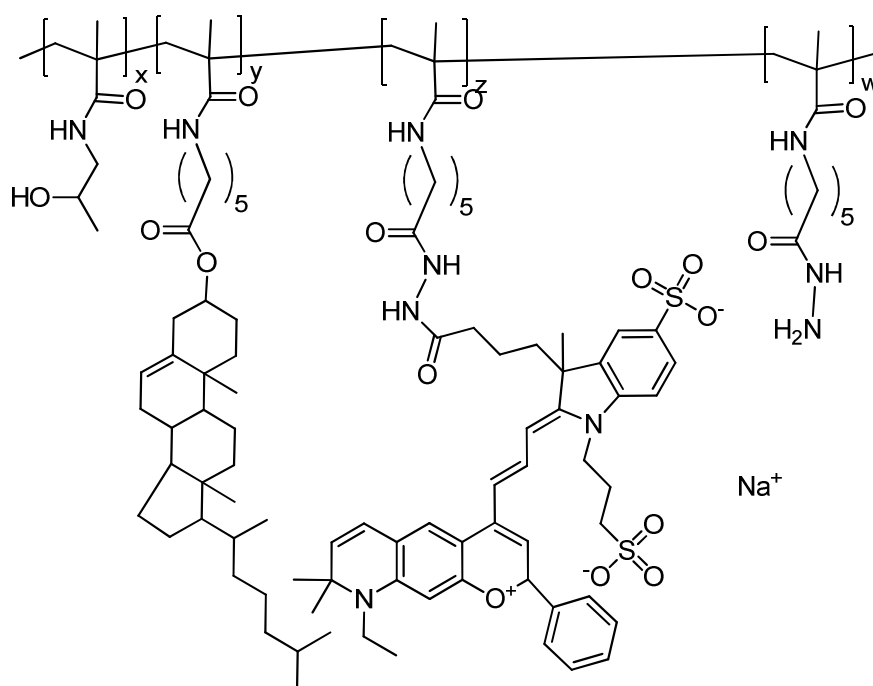


Figure 7-2. Chemical structure of UH23.

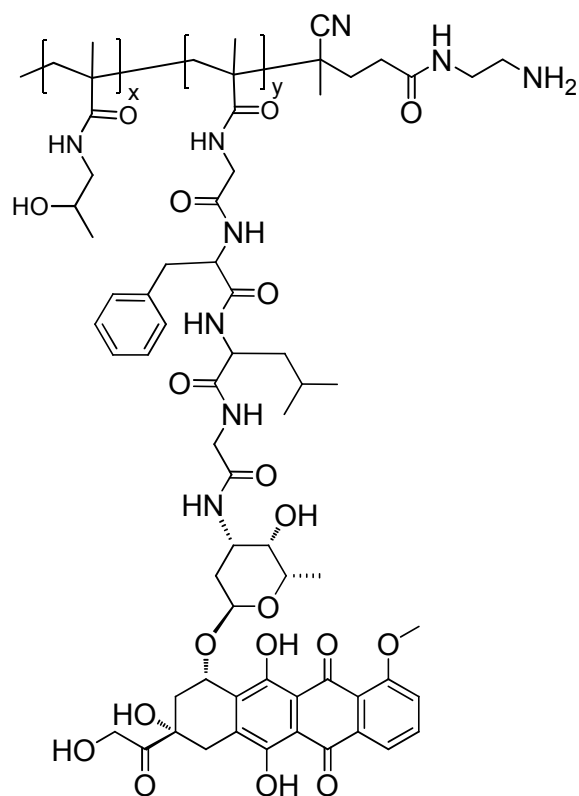


Figure 7-3. Chemical structure of UH26.

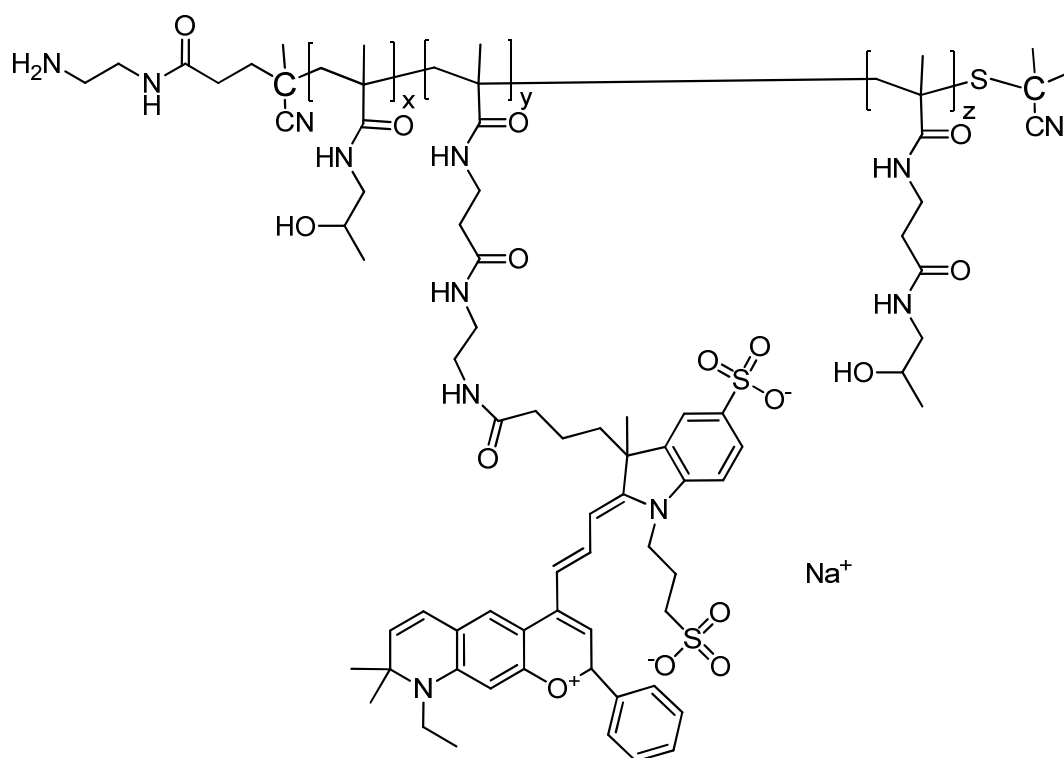


Figure 7-4. Chemical structure of UH27.

7.2 Inhaltsangabe in deutscher Sprache

Poly(glyceroladipat) (PGA) ist ein interessantes bioabbaubares Polymer mit großem Potenzial für die Verwendung in verschiedenen Drug Delivery Systemen. Die freie Hydroxylgruppe der PGA Hauptkette ermöglicht vielfältige Modifizierung und damit eine flexible Anpassung der Eigenschaften. Durch die Veresterung der Hydroxylgruppen mit verschiedenen Fettsäuren wurden vielversprechende amphiphile Polymere mit einer großen Bandbreite an Eigenschaften erhalten.

Der Hauptteil dieser Arbeit beschäftigt sich mit der Herstellung und der umfassenden Charakterisierung von nanopartikulären Wirkstoffträgern aus fettsäuremodifiziertem PGA. Durch die Optimierung der Nanopräzipitationsmethode konnten selbst stabilisierte Lauryl-, Stearyl-, Oleyl- und Behenyl-PGA Nanopartikel definierter Größe und enger Partikelgrößenverteilung hergestellt werden. Ihre Eigenschaften wurden eingehend untersucht und es wurde gezeigt, dass die Kettenlänge der angehängten Fettsäure sowie der Grad der Veresterung die physikochemischen Eigenschaften der Polymere und Nanopartikel erheblich beeinflussen.

Photonenkorrelationsspektroskopie (PCS), asymmetrische Fluss Feld-Fluss Fraktionierung (AF4) und verschiedene Techniken der Transmissionselektronenmikroskopie (TEM) lieferten fundierte Ergebnisse zu Partikelgröße sowie Partikelform und -struktur. Die innere Struktur der Partikel wurde zudem detailliert durch Röntgenklein- und -weitwinkelstreuung (SAXS, WAXS) untersucht. Auf Grundlage dieser Ergebnisse wurden zwei Strukturmodelle entworfen, die die unterschiedliche Architektur der Nanopartikel darstellen. Darüber hinaus wurde das thermische Verhalten von Polymeren und deren Partikel mit Differenzialkalorimetrie (DSC), SAXS, WAXS und Kernspinresonanzspektroskopie ($^1\text{H-NMR}$) untersucht. Die Inkorporation des solvatochromen Fluoreszenzfarbstoffes Nilrot lieferte Informationen zur Polarität verschiedener PGA Nanopartikel. Zur Bestimmung der Beladungskapazität der Nanopartikel wurde eine eigene Methode entwickelt und eine exemplarische Studie durchgeführt.

Als nächster Schritt hin zu *in vivo* Experimenten wurden Zelltoxizitätsstudien mit verschiedenen PGA basierten Nanopartikeln durchgeführt. Dabei wurde die Verträglichkeit gegenüber Erythrozyten und HepG2 Zellen (humane Hepatoblastomazellen) getestet, die sich fast ausschließlich als sehr gut erwies.

Auf Grundlage der vielversprechenden Ergebnisse der *in vitro* Charakterisierung wurden erste *in vivo* Studien an gesunden sowie tumortragenden Labormäusen durchgeführt. Um die Verweildauer der Nanopartikel im Blutkreislauf zu erhöhen wurden diese mit einem hydrophilen Hydroxypropylmethacrylamid (HPMA) basierten Polymer beschichtet. Diese Polymere wurden einerseits kovalent gebunden und andererseits physikalisch angelagert und die Unterschiede *in vivo* untersucht. Die beschichteten Partikel zeigten eine erhöhte Verweildauer im Körper sowie eine verstärkte Anreicherung im subkutanen Tumorgewebe gegenüber den unbeschichteten.

Im zweiten Teil dieser Arbeit wird die erstmalige Verwendung von Lauryl-PGAs in Depotimplantaten zur kontrollierten Wirkstofffreisetzung behandelt. Diese Polymere bieten den Vorteil, dass sie bioabbaubar sind, durch Standardkanülen injiziert werden können und dies ohne den Zusatz eines organischen Lösungsmittels (oder mit max. 5 % N-Methyl-2-pyrrolidon). Darüber hinaus findet innerhalb der Implantate kein Abfall des pH-Wertes in den stark sauren Bereich statt, wie dies bei der Degradation der verbreitet eingesetzten Polymere PLA oder PLGA auftritt.

Die Methoden der ^1H -NMR Relaxometrie und der Texturanalyse lieferten Informationen über Viskosität und andere mechanische Eigenschaften der Polymere und zeigten auf, wie diese durch den Veresterungsgrad beeinflusst werden.

In einer *in vitro* Fluoreszenzstudie wurde die Freisetzung eines hydrophilen und eines lipophilen Farbstoffes aus vier Lauryl-PGAs nichtinvasiv untersucht. Elektronenspinresonanzbildgebung (ESRI) lieferte zusätzlich Einblicke in das Innere der Implantate. So konnte das Eindringen des Puffers, die Beweglichkeit der Spinsonde, die Mikropolarität und der pH-Wert in verschiedenen Schichten des Implantates beobachtet werden.

Darüber hinaus wurde die *in vivo* Freisetzung eines lipophilen Stoffes aus Lauroyl-PGA Implantaten in einer 6-monatigen Pilotstudie untersucht. Diese lieferte auch erste Hinweise zur Verträglichkeit der eingesetzten Polymere.

Insgesamt konnte gezeigt werden, dass Poly(glyceroladipat) durch die vielfältigen Variationsmöglichkeiten eine interessante Plattform für die Herstellung unterschiedlichster bioabbaubarer Materialien bietet. Die große Bandbreite der Einsatzmöglichkeiten – von Nanopartikeln bis hin zu Implantaten – ist sehr vielversprechend, genauso wie viele Ergebnisse der *in vitro* und *in vivo* Untersuchungen dieser Systeme. Dennoch bleiben noch einige Fragen offen, die in der vorliegenden Arbeit aufgeworfen und diskutiert werden. Die vorgeschlagenen Lösungsansätze geben Anstoß für die weitere Fortentwicklung der Materialien und Systeme, was im Hinblick auf die bisherigen Ergebnisse sicherlich lohnenswert ist.

7.3 Acknowledgment

Firstly, I want to express my special thanks and appreciation to my supervisor Prof. Dr. Karsten Mäder for the opportunity to join his group and to work on this interesting, interdisciplinary topic. I highly appreciated his support, his advice and the possibility to get to know so many analytical methods during the process of this work.

I would also like to thank Prof. Dr. Jörg Kressler, Dr. Karsten Busse, Toufik Naolou, Dr. Elkin Amado, Dr. Günther Förster and Delf Conrad of the Physical Chemistry department for the fruitful cooperation, the synthesis of the PGA polyesters and the introduction into the exciting field of X-ray diffraction. Many thanks go to Dr. Judith Kuntsche who provided the opportunity to perform synchrotron X-ray measurements at DESY in Hamburg.

Also to my cooperation partners at the IMC in Prague, Prof. Karel Ulbrich, Thomáš Etrych, PhD, and particularly Petr Chytil, PhD, I express my gratitude for their interest in my work, the synthesis of HPMA copolymers and the helpful discussions and inspirations.

I also thank Prof. Dr. Thomas Groth for providing the opportunity to work in his laboratory for cell experiments. In this context, I want to thank Marcus Niepel and Marlis Porobin for their instructions.

To Dr. Henrike Caysa, Dr. Thomas Müller, Johannes Kutza, Stefan Hoffmann and Andreas Schädlich, I owe gratitude for their support in the field of *in vivo* experiments as well as Martina Henicke and Cornelia Gottschalk for animal care.

Furthermore, many thanks go to Dr. Hendrik Metz for his instructions and support with ESR and NMR measurements and the valuable discussions and suggestions.

I also want to express my gratitude to Dr. Gerd Hause and Dr. Annette Meister for TEM and cryo-TEM images, Dr. Regina Schöps, Dr. Jürgen Vogel and Danny Misiak for their assistance with confocal laser scanning microscopy, Dr. Judith Kuntsche for the introduction into AF4 measurements, Dieter Reese for the manufacture of the ESR sample holders as well as Ute Mentzel, Kerstin Schwarz, Bettina Fölting and my student Priscilla F. Maeda for their active support with different measurements.

Special thanks go to all colleagues of the Pharmaceutical Technology group, particularly those who welcomed me so friendly and made it easy for me to get settled in Halle: Friederike Eisenächer, Claudia Kutza, Dr. Andreas Noack, Dr. Alexander Lochmann and Johannes Kutza – I enjoyed the time we had together and with the whole group.

Last but not least, I deeply thank my husband Andreas and my mother Margarete for their love, their continuous support and encouragement and their appreciation for my work. No words can express my gratitude.

7.4 Publications

7.4.1 Research Papers

V. M. Weiss, T. Naolou, G. Hause, J. Kuntsche, J. Kressler, K. Mäder, Poly(glycerol adipate)-fatty acid esters as versatile nanocarriers: From nanocubes over ellipsoids to nanospheres, *Journal of Controlled Release* 158 (2012) 156-164.

V. M. Weiss, T. Naolou, E. Amado, K. Busse, K. Mäder, J. Kressler, Formation of Structured Polygonal Nanoparticles by Phase-separated Comb-like Polymers, *Macromolecular Rapid Communications* 33 (2012) 35-40.

V. M. Weiss, T. Naolou, T. Groth, J. Kressler, K. Mäder, *In vitro* Toxicity of Stearoyl-Poly(glycerol adipate) Nanoparticles, *Journal of Applied Biomaterials & Functional Materials* 10 (3) (2012) 163-169.

K. Busse, V. M. Weiss, T. Naolou, D. Conrad, K. Mäder, J. Kressler, Microphase separation of poly(glycerol adipate)-*graft*-oleoyl ester, 2013, in preparation.

7.4.2 Book chapters

T. Naolou, V. M. Weiss, D. Conrad, K. Busse, K. Maeder, J. Kressler, Fatty Acid Modified Poly(glycerol adipate) - Polymeric Analogues of Glycerides, in: *Tailored Polymer Architectures for Pharmaceutical and Biomedical Applications*, C. Scholz et al., ACS Symposium Series, American Chemical Society, Washington, DC, 2013.

7.4.3 Abstracts and posters

V. M. Weiss, T. Naolou, G. Hause, J. Kressler, K. Mäder, Poly(glycerol adipate)-stearic acid esters – biodegradable polymers for versatile nanocarriers with defined shapes and structures, 8th World Meeting on Pharmaceutics, Biopharmaceutics and Pharmaceutical Technology 2012, Istanbul, Turkey (abstract & poster).

V. M. Weiss, G. Hause, E. Amado, K. Mäder, Versatile nanocarriers from Poly(glycerol adipate)-stearic acid esters – insight into geometry and internal structure, Controlled Release Society Germany Local Chapter Meeting 2012, Würzburg, Germany (abstract & poster).

V. M. Weiss, J. Kressler, T. Groth, K. Mäder, *In vitro* Toxicity of Stearoyl-Poly(glycerol adipate) Nanoparticles, *Advanced Functional Polymers for Medicine 2012*, Vico Equense, Italy (abstract & poster).

J. Kressler, T. Naolou, D. Conrad, K. Busse, E. Amado, V. Weiss, K. Maeder, Fatty acid modified poly(glycerol adipate) - polymeric analogues of glycerides, *Polymer Preprints* (American Chemical Society, Division of Polymer Chemistry) 53(1) (2012) 567-568.

7.5 Curriculum vitae

Verena Maria Weiss geb. Gläßer

born: 27.05.1983 in Herrenberg, Germany

nationality: German

marital status: married

Education

08/2009 – 04/2013	Ph.D. student in the group of Prof. Dr. Karsten Mäder, Institute of Pharmacy (Pharmaceutical Technology), Martin-Luther University Halle-Wittenberg
06/2009	Approbation as a pharmacist, Eberhard Karls University Tübingen
12/2008	Diploma degree in pharmacy (Pharmaceutical Technology), Eberhard Karls University Tübingen
05/2008 – 10/2008	Diploma thesis in pharmaceutical technology at Boehringer Ingelheim Pharma GmbH & Co. KG, Biberach/Riß: “Die Kompressionsanalyse im Vergleich zwischen hydraulischer und Rundlauftablettenpresse“
04/2004 – 04/2008	Pharmacy studies at Eberhard Karls University Tübingen
06/2003	Abitur at Andreae Gymnasium Herrenberg

Work experience

since 06/2013	Trainee Quality Assurance at Takeda GmbH, Oranienburg
08/2009 – 04/2013	Research and teaching assistant at the Institute of Pharmacy, Martin-Luther University Halle-Wittenberg
11/2008 – 04/2009	Practical training at Marktapotheke Ludwigsburg
05/2008 – 10/2008	Practical training at Boehringer Ingelheim Pharma GmbH & Co. KG, Biberach/Riß, Research & Development
08/2006 – 09/2006	Practical training at GlaxoSmithKline GmbH & Co. KG, Herrenberg, Research & Development
02/2005 – 03/2005	Practical training (Famulatur) at Universitätsklinikums-apotheke Tübingen
08/2004 – 09/2004	Practical training (Famulatur) at Apotheke Haug, Herrenberg

7.6 Selbstständigkeitserklärung

Hiermit erkläre ich an Eides statt, dass ich die Ergebnisse der vorliegenden
Dissertationsarbeit

Parenteral drug delivery systems
based on fatty acid modified poly(glycerol adipate)

am Institut für Pharmazie der Martin-Luther Universität Halle-Wittenberg unter
Anleitung von Herrn Prof. Dr. Karsten Mäder selbstständig erarbeitet bzw. im Rahmen
der angegebenen Kooperationen erhalten habe. Die Dissertation habe ich ohne fremde
Hilfe angefertigt und dazu keine anderen als die von mir angegebenen Quellen und
Hilfsmittel benutzt. Die den verwendeten Werken wörtlich oder inhaltlich
entnommenen Stellen sind als solche kenntlich gemacht.

Ferner erkläre ich, dass ich mich erstmals um die Erlangung eines Doktorgrades
bewerbe und die vorliegende Dissertationsschrift keiner anderen in- oder ausländischen
Fakultät vorgelegt habe.